Design and Test of a 94 GHz Overmoded Traveling Wave Tube Amplifier

by

Elizabeth J. Kowalski

B.S. Electrical Engineering, the Pennsylvania State University (2008)
S.M. Electrical Engineering and Computer Science, Massachusetts Institute of Technology (2010)

Submitted to the
Department of Electrical Engineering and Computer Science
in partial fulfillment of the requirements for the degree of

Doctor of Philosophy

at the

MASSACHUSETTS INSTITUTE OF TECHNOLOGY

February 2015

Author .....
Department of Electrical Engineering and Computer Science
December 31, 2014

Certified by .....
Richard J. Temkin
Senior Research Scientist, Department of Physics
Thesis Supervisor

Accepted by .....
Professor Leslie A. Kolodziejski
Chairman, Committee on Graduate Students
Department of Electrical Engineering and Computer Science

Design and Test of a 94 GHz Overmoded Traveling Wave Tube Amplifier

by

Elizabeth J. Kowalski

Submitted to the Department of Electrical Engineering and Computer Science
on December 31, 2014, in partial fulfillment of the
requirements for the degree of
Doctor of Philosophy

Abstract

This thesis discusses the design and test of an overmoded W-band Traveling Wave Tube (TWT). The TWT was designed to operate in the rectangular TM_{31} cavity mode at 94 GHz. The unwanted lower order, TM_{11} and TM_{21}, modes were suppressed using selectively placed aluminum nitride dielectric loading. Simulations in 3-D CST Particle Studio confirmed suppression of unwanted modes due to dielectric loading and operation in the TM_{31} mode. The TWT was designed to operate at 31 kV with 310 mA and a 2.5 kG solenoid magnet. Simulations in both 1-D Latte and 3-D CST predicted 32 dB of gain, 200 MHz bandwidth, and 300 W peak output power for the TWT at 94 GHz. Test structures of 9- and 19- cavities were made via CNC direct machining. Cold test measurements showed suppression of the unwanted modes and transmission of the TM_{31} mode, which correlated well with HFSS simulations. Two final 87-cavity structures were built and cold tested.

The experiment was designed and built in-house at MIT (with exception of the electron gun cathode, manufactured by industry). It was operated with a 3 microsecond pulsed power supply. A beam test was implemented which confirmed operation of the TWT set up and electron gun. The electron gun operated at 31 kV with 306±6 mA of current detected at the collector and 88 % transmission of current. Initial operation of the TWT showed zero-drive stable operation and demonstrated 8 dB of device gain and 10 W peak output power at 95.5 GHz. Following these first tests, the magnetic field alignment was improved and the second structure, which showed better circuit transmission in cold test, was installed. The overmoded TWT produced 21±2 dB device gain (defined as P_{out}/P_{in}) at 94.3 GHz and 27 W of saturated output power in zero-drive stable operation. The TWT was estimated to have about 6 dB of additional loss due to coupling into and out of the circuit. Taking that loss into account, the gain on the TWT circuit itself was estimated to be 27±2 dB circuit gain. CST simulations for the experimental current and voltage predict 28 dB circuit gain, in good agreement with measurements.

This experiment demonstrated the first successful operation of an overmoded TWT. The overmoded TWT is a promising approach to high power TWT opera-

tion at W-Band and to the extension of the TWT to terahertz frequencies.

Thesis Supervisor: Richard J. Temkin
Title: Senior Research Scientist, Department of Physics

Acknowledgments

This thesis would not have been possible without my advisor, Dr. Richard J. Temkin. Always willing to help, offer advice, and teach the finer points of vacuum electronics, he guided me through this project and helped to make my PhD successful. Every member of the Waves and Beams Group in the PSFC also helped me in my research. Particularly, my officemates Dr. Emilio Nanni and XueYing Lu dealt with my distracting conversation, pungent teas, and research woes. Ivan Mastovsky's expertise helped my experiment to be operational, while Dr. Michael Shapiro ensured that my theory and simulations were correct. In addition, Dr. Sudheer Jawla, Dr. David Tax, Dr. Brian Munroe, Jason Hummelt, JeiXi Zhang, Sam Schuab, Alexander Soane, and Haoron Xu all offered their advice and help, from Friday evening brainstorming to unexpected company in the lab on Saturday.

Graduate Women at MIT, GWAMIT, helped me to realize I was not alone in my endeavors and introduced me to some amazing women at MIT who encouraged me and became great friends. It was amazing to be a part of shaping GWAMIT, and I hope that the organization continues to grow in the future.

Of course, my family and friends helped me through the long nights, weeks, months, and years of research. My parents taught me how to learn, and my sisters taught me how to have a life. My husband, Edward Loveall, provided endless support. He listened to me practice countless presentations, so he may even understand 31 % of this thesis.

Elizabeth Kowalski

Cambridge, MA

December 22, 2014

to Edward

onion (ˈənyən) *noun.* An edible bulb with a pungent taste and smell, composed of several concentric layers, used in cooking.

— Oxford English Dictionary

Contents

1 Introduction **21**

1.1 Motivation 21

1.2 A Brief History of TWTs 29

1.2.1 Vacuum Tubes and Radar 29

1.2.2 Invention of the TWT 32

1.2.3 More Vacuum Devices 35

1.3 Modern Day W-Band Vacuum Tubes 36

1.3.1 W-Band TWTs 36

1.3.2 Other W-Band Devices 38

1.3.3 Overmoded TWTs 39

1.4 Overview of Thesis 40

2 Theory of Traveling Wave Tubes **41**

2.1 TWT Overview 41

2.2 Electron Beams in Vacuum Tubes 44

2.2.1 Pierce Electron Gun 44

2.2.2 Magnetic Field Confinement 51

2.2.3 Collector 53

2.3 Analytical Theory for Slow-Wave Structures 53

2.3.1 Gain in the Circuit 59

2.4 Types of Slow-Wave Structures 62

2.4.1 Helical TWTs 63
2.4.2 Coupled-Cavity TWTs 65

3 Design of a 94 GHz Overmoded Coupled-Cavity TWT 69
3.1 Problem Statement 69
3.2 Electromagnetic Cavity Design 70
3.2.1 Cavity Fields 71
3.2.2 The TM_{31} Mode 73
3.2.3 Other Modes and Dielectric Loading 76
3.2.4 Final Design Parameters 81
3.2.5 Other Design Considerations 89
3.3 Analytical Calculations and Simulations 91
3.3.1 Pierce TWT Analytical Theory 91
3.3.2 3-D CST Simulations 94

4 Cold Tests of the Overmoded TWT Circuit 99
4.1 Machining Techniques and Tolerances 99
4.2 Low Power Cold Test Measurements 103
4.2.1 Materials 103
4.2.2 Dielectric Loading 110
4.3 87-Cavity Design Cold Test Results 112

5 Experiment Design and Set-up 119
5.1 Experiment Overview 119
5.2 Solenoid Magnet 122
5.3 Electron Gun 125
5.3.1 Design 126
5.3.2 Manufacturing 130
5.4 Driving Sources 133
5.4.1 94 GHz EIO 133
5.4.2 W-band Solid-State AMC 135

5.5 RF Vacuum Windows 136
5.6 High Power Pulse Modulator 138
5.7 Safety Interlock System and Controls 141
5.8 Installation 143

6 Experiment Results **147**
6.1 Electron Gun Beam Test 147
6.2 94 GHz TWT - Structure A 151
6.2.1 Full Dielectric 151
6.2.2 Half Dielectric 156
6.3 94 GHz TWT - Structure B 157
6.3.1 Results 157
6.3.2 Analysis 162

7 Conclusions **171**
7.1 Summary of Results 171
7.2 Discussion of Relevance 173
7.3 Future Work 174

List of Figures

1-1 The Haystack Observatory 94 GHz antenna. 22

1-2 Average output power vs. frequency for vacuum and solid state devices. 23

1-3 Transmission (%/km) vs. frequency for sea-level conditions. 25

1-4 Examples of electronic warfare usages [1]. 26

1-5 The U. S. Military Active Denial System. 27

1-6 Early vacuum tubes diagrams. 30

1-7 Drawings of the first TWT design. 32

1-8 A diagram of the first TWT experiment and John Pierce. 33

2-1 A block diagram overview of a TWT amplifier circuit. 42

2-2 The $\hat{z}$-directed electric field in the TWT. 43

2-3 Diagrams with different anode-cathode configurations. 47

2-4 A diagram showing the ideal design of a Pierce electron gun. 49

2-5 The electron beam compression and magnetic field confinement. . . . 49

2-6 The space charge reduction factor, R vs. $\beta_e b$. 57

2-7 B vs. non-synchronous parameter, b, for various conditions. 62

2-8 The helical TWT slow-wave structure. 63

2-9 A folded waveguide coupled-cavity design. (Picture from [37].) 65

2-10 A rectangular folded-waveguide coupled-cavity TWT. 65

2-11 The dispersion relation and period length for a coupled-cavity TWT. 66

3-1 An illustration of the electric and magnetic fields in the TM_{110} cavity mode. (Figure modified from [12].) 72
3-2 Contour plots of the electric field, E_z, for the lowest order cavity modes. 74
3-3 Two cavities of the TWT structure linked via staggered coupling slots, as seen with an isometric view and from the top of the structure. . . 75
3-4 The electric field patterns of the three lowest order TM modes in a rectangular cavity tuned to 94 GHz for the TM_{31} mode. 77
3-5 The dispersion relation for the lowest order TM modes of the cavity. . 78
3-6 Placement of dielectric on the top and bottom of the cavity. 79
3-7 The electric field patterns of the three lowest order TM modes in a rectangular cavity. 80
3-8 The transmission through a single cavity with and without dielectric loading for the lowest four TM modes. 81
3-9 Simulation results showing the variation of current, K, and C as dependent on cavity parameters. 82
3-10 The effect of beam tunnel size on calculated coupling impedance through the middle of the circuit. 83
3-11 I_0/V_0 ratio vs. operation voltage, V_0, for different electron beam radii. 85
3-12 The final cavity design showing the dielectric loading and manufacturing fillets. 86
3-13 The dispersion relation for the first three cavity modes of Design A, as calculated by HFSS. 87
3-14 The coupling impedance and dispersion relation for the TM_{31} mode of Designs A and B. 88
3-15 The input coupler from standard waveguide into the first cavity of the TWT. 90
3-16 Linear gain vs. operation voltage for 94 GHz operation and design parameters discussed in Table 3.2. 93
3-17 Linear gain vs. frequency for LATTE simulations. 93
3-18 The full 87 cavity structure with dielectric loading as simulated in CST. 95

3-19 Power out vs. time for a 90 mW input signal along with an FFT of the output signal. 95
3-20 The energy of the particles in the beam tunnel at the end of the circuit, and the particle density along the length of the cavity. 96
3-21 Output power vs. input power for the simulated TM_{31} coupled-cavity TWT. 97

4-1 The assembly of 4-plate and 2-plate 9-cavity cold test structures. . . . 101
4-2 HFSS simulations showing a WR-08 waveguide with gaps at the top, mid-plane, and bottom of the waveguide. 102
4-3 CAD drawings and machined 9- and 19-cavity cold test structures. . . 104
4-4 The measured transmission through (a) 9- and (b) 19-cavity OFHC copper structures compared to HFSS simulations. 105
4-5 The measured transmission through (a) 9- and (b) 19-cavity glidcop structures compared to HFSS simulations. 106
4-6 The measured transmission for copper cold test structures. 108
4-7 The measured transmission for glidcop cold test structures. 109
4-8 Detailed pictures of the final 87-cavity structure. 113
4-9 Transmission measurements for the first 87-cavity structure (A). . . . 114
4-10 Transmission measurements for the first 87-cavity structure (A) with dielectric loading 115
4-11 Transmission measurements for Structures A and B with no dielectric loading. 116
4-12 Transmission measurements for the assembled structures that underwent hot test. 116

5-1 The full experimental set up. 120
5-2 A rendering of the TWT tube assembly inside of the solenoid magnet. 121
5-3 The 2.5 kG solenoid magnet installed for testing. 122
5-4 Poisson calculation of the solenoid electromagnet. 124
5-5 Measurement of the on-axis $\hat{z}$-directed solenoid magnetic field. 125

5-6 The 2-D cylindrical electron gun geometry. 126
5-7 The beam envelope calculated via Michelle. 127
5-8 The equipotential lines and particle trajectories as calculated by Michelle. 128
5-9 The electric field in the electron gun for operation at 31 kV. 129
5-10 A cross-sectional view of the electron gun modeled in Autodesk Inventor with cold dimensions. 131
5-11 Pictures of the electron gun and beam test assembly. 132
5-12 A picture of the 94 GHz EIO. 134
5-13 Frequency vs. power for the Millitech AMC. 135
5-14 Measured and calculated transmission through the RF windows. . . . 137
5-15 One of the fused silica RF windows in a 2-3/4 con flat flange, installed on the TWT. The input WR-28 waveguide can be seen 138
5-16 A block-diagram of the PFN and high voltage pulse transformer set-up with dual-experiment access. 139
5-17 The modulator set-up of the TWT experiment. 140
5-18 An electronic schematic of the high voltage pulse transformer and TWT experiment. 141
5-19 The control system for the experiment and safety interlock system. . 142
5-20 Installation of the TWT structure onto the anode. 143
5-21 Installation of the WR-10 90 degree waveguide bends and support structures into the tube. 144
5-22 Completion of installation for the TWT experiment. 145
5-23 The fully assembled TWT experiment. 146

6-1 A cross-sectional rendering of the beam test experiment. 148
6-2 Sample voltage and collector current measurements from the beam test. 149
6-3 The Child-Langmuir curve for the electron gun. 150
6-4 Device gain (and output power) vs. input power observed at 95.5 GHz with V_0 =27 kV. 152

6-5 Sample traces of the collector current and output power measurements for Structure A. 154
6-6 Device gain vs. bandwidth for operation at V_0=27 kV. 155
6-7 Device gain and output power vs. input power, showing 20.9 dB linear gain. 158
6-8 Circuit gain in the TWT as compared to simulated gain. 160
6-9 Device gain vs. frequency in the TWT for two different operation points. 161
6-10 The diagnostic measurements for high-gain operation at 94.27 GHz. . 163
6-11 The diagnostic measurements for saturated power operation at 94.26 GHz. 165
6-12 The diagnostic measurements for an oscillation observed during the start of operation. 167

List of Tables

3.1 Dimensions of Final Structure 87
3.2 TWT Operation Parameters 92

4.1 Coupled-Cavity Loss with Dielectric Loading (dB/cm) 111

Chapter 1

Introduction

1.1 Motivation

In this technology-dependent world, electromagnetic applications are present in our everyday lives. Household microwave ovens, commercial cell phone communications, radar, satellites, and advanced military capabilities are just a few of the varied ways that electromagnetic waves are used. For the most part, these applications exist at low frequencies and low powers where solid state transistors and other devices are able to satisfy the needs of the applications. Advances to higher frequency bands require the development of new devices at those frequencies. Currently, there are few devices which are capable of operating in the regime of high-frequency and high-power. Vacuum electronics are extremely useful for high power applications, but extending these devices to high frequencies is difficult for reasons that will be explored. As we expand our scientific knowledge, applications are available at high frequencies and for higher powers, but they require devices for practical implementation which don't yet exist.

The need for both higher power and higher frequency devices for millimeter wave, microwaves, and terahertz waves is easily understood by looking at radar and communications systems. Simply put, operating with higher powers means that we can communicate over longer distances. In addition to power, we must consider the bandwidth of communication, i.e. the range of frequencies over which a transmission can

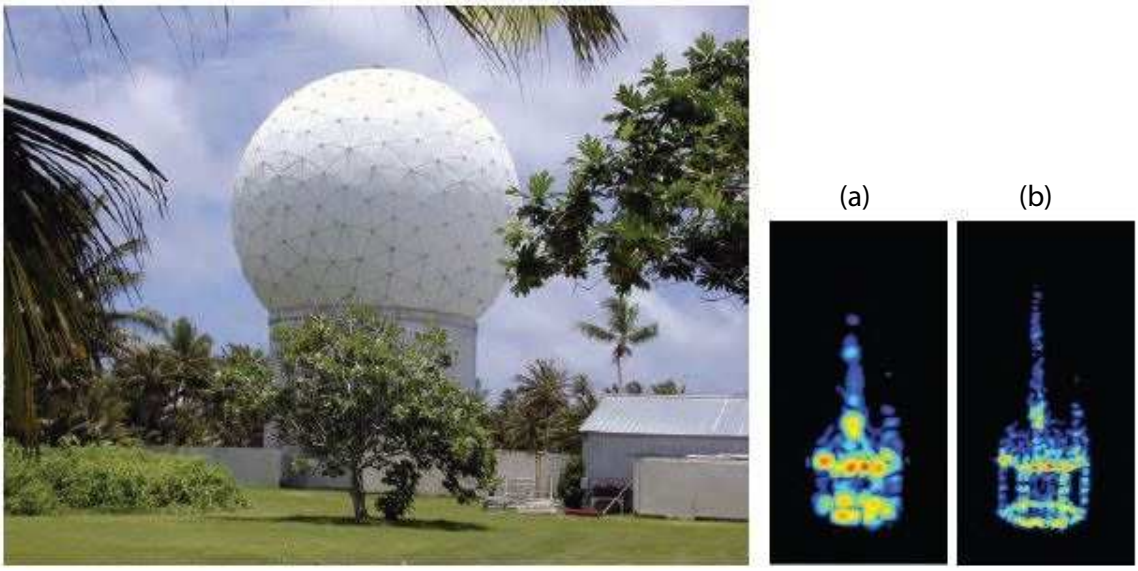

Figure 1-1: The Haystack Observatory 94 GHz antenna. Two sets of simulated data show a satellite that has been imaged with (a) 2 GHz or (b) 4 GHz bandwidth [11].

occur. Operation at higher frequencies means that larger bandwidths are available to transmit data, leading to higher resolution imaging. For example, Haystack Radar, shown in Figure 1-1 is a radar system located in Westford, MA that is used for space tracking, communications, and astronomy. The system originally operated at 10 GHz, and was recently upgraded to have a second operation point at 94 GHz. The bandwidth available at 94 GHz can be as large as 4 GHz. The figure shows the simulated detection of a satellite by the Haystack radar via two different operation bandwidths for comparison [11]. It's easily observed that more details can be seen with a larger bandwidth. Operation at 94 GHz allows for this large bandwidth to be achieved and for details to be resolved which would not otherwise be detected.

Space communications also benefit from large bandwidths due to large distances requiring long transmission times. NASA has built most of their communications systems around 10 GHz, like those on board the Mars Curiosity Mission, because it has a relatively high bandwidth for communication and reliable, high power devices are available to operate at that frequency. Some NASA missions, like the Mars Reconnaissance Orbiter, operate at higher frequencies, about 32 GHz, in order to support higher bandwidths and higher data rates [47]. It is likely that future NASA

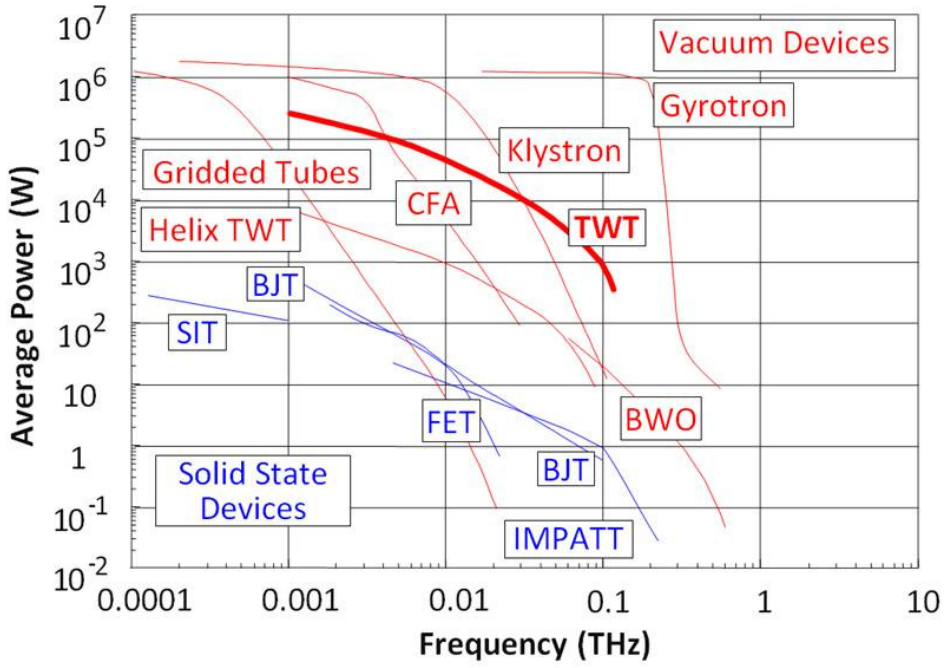

Figure 1-2: Average output power vs. frequency for vacuum and solid state devices. This graph demonstrates the THz gap, from 0.3–10 THz, a frequency range for which no or limited devices exist. Figure adapted from [23].

missions will be at even higher frequencies for better communications; but reliable, high power, devices must exist at those frequencies first.

Many more applications for high power, high frequency devices exist, but all electromagnetic applications are limited by our abilities to produce and amplify electromagnetic signals at the frequency of operation. At low frequencies, high power sources and amplifiers are readily available. However, at higher frequencies there is an undeniable need for reliable, high-power, and cost-effective power sources and amplifiers.

Unfortunately, there is a range of frequencies with radar and communications applications for which there are no viable devices which offer high output powers. Figure 1-2 displays the power limits of electronic devices as they depend on frequency. Solid state and vacuum electronic devices provide a wide range of available power for diverse applications below 1 GHz. Vacuum electronics are robust and able to provide higher power at frequencies up to 100 GHz (and even higher). In general, vacuum

devices are less desirable because they can be large, complex systems. However, their ability to provide high power makes them viable options for certain applications. For all electronic devices, the relative size of interaction circuits inversely scales with frequency. At high frequencies, above 300 GHz, the small wavelengths of operation severely limit the types of devices that can perform at high powers. At even higher frequencies, above 10 THz, laser photonic devices are able to provide high power for applications in the visible light spectrum, x-rays, and gamma-rays. These devices have wavelengths less than 30 micrometers. The output power for devices such as quantum-cascade lasers drops off rapidly at frequencies lower than 100 THz due to physical limitations at relatively large wavelengths of operation [63]. In addition to vacuum devices, quantum-cascade lasers in the THz range of frequencies are a large area of interest.

At present, the two opposing frequency limits between electronic and photonic devices leads to the range of frequencies for which there are no high power devices. The range is between 300 GHz and 10 THz and is referred to as the terahertz gap. In this gap there is very limited power output from all types of devices. Though, many vacuum electron devices have recently been able to output relatively high power in this frequency range. Recent experimental achievements with gyrotrons, klystrons, and Traveling Wave Tubes (TWTs) have demonstrated that vacuum electronics are able to perform well in the Terahertz Gap, though limitations in power output still exist in all types of devices [5]. The characteristics and benefits of these devices will be described in the next section.

For practical applications, several frequency ranges, referred to as "windows" or "bands," are commonly used in communications and are the subject of research developments. These bands take advantage of the earth's atmospheric conditions, as shown in Figure 1-3, which shows the transmission associated with an electromagnetic wave traveling through the earth's atmosphere. They are called "windows" since they refer to a range of frequencies that can be "seen", or transmitted, through the atmosphere. The ability of a certain frequency to transmit changes due to several atmospheric factors, but, for simplicity, sea level conditions with moderate humidity

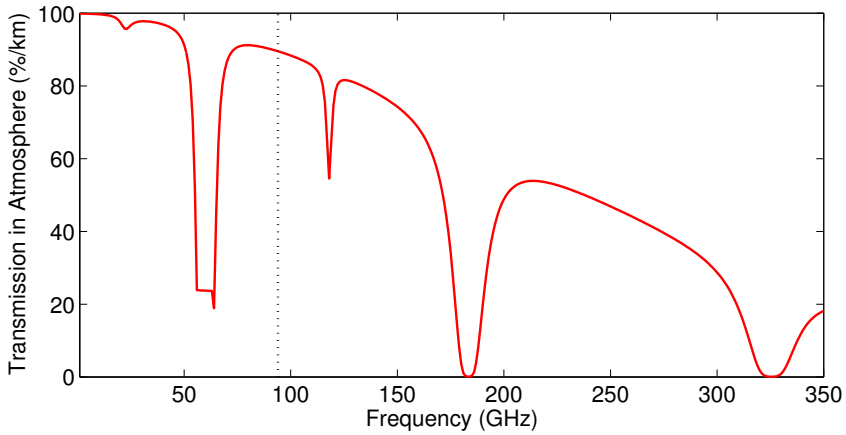

Figure 1-3: Transmission (%/km) vs. frequency for sea-level conditions. The black dotted line indicates the atmospheric window at 94 GHz.

were assumed in calculation. Several frequency windows can be seen in Figure 1-3 where there are transmission peaks in the atmosphere. Resonances in the atmosphere, which absorb large quantities of electromagnetic waves leading to transmission dips at certain frequencies, are due to molecules in the air. In the frequency range shown in the figure (0–350 GHz), oxygen and water particles dominate the loss effects. Atmospheric losses are dependent on a wide variety of conditions that affect the molecules in the air, most importantly weather conditions and altitude, but the windows of low losses shown in the figure are still the best transmission frequencies to use in communication applications [59]. The low loss windows can also be referred to as high transmission bands, i.e. it takes less power to transmit electromagnetic waves at those frequencies for longer distances than at the resonance frequencies. In addition, higher frequencies have larger windows, allowing for larger operation bandwidths at those frequencies.

Several systems and agencies have built communications infrastructure in the frequency bands that have low losses in atmosphere. At 94 GHz there is a large window of communications that is often associated with air force communications and many developments in vacuum devices have been aimed at developing high power tubes for use in that frequency range. In addition, there is a window at 220 GHz which is also an area of large development for communications due to the large bandwidth

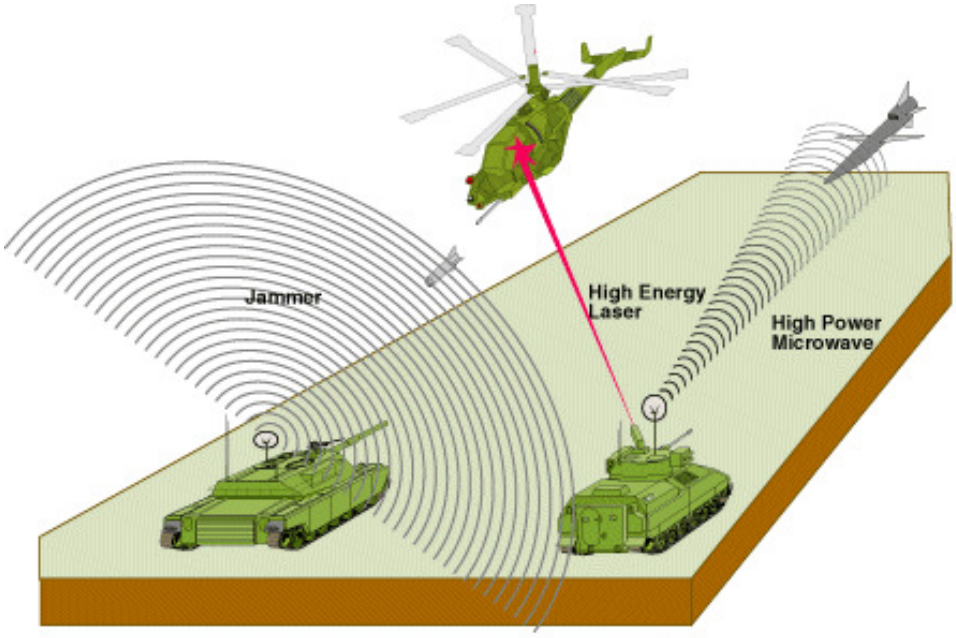

Figure 1-4: Examples of electronic warfare usages [1].

that is possible. These high frequency windows are also in use for weather research due to atmospheric transmission characteristics, the small wavelength of operation, and the large bandwidth available. These two bands at 94 and 220 GHz are below the defined Terahertz Gap in frequencies, and vacuum tubes exist which provide useful output powers. However, high power devices are still in development at these frequencies due to a need for more power than is currently accessible and a desire for cheaper alternatives. It is also relevant that development of devices at these frequencies will lead to more robust devices that can be modified for use at even higher frequencies in the following years.

Just below the Terahertz Gap is a band of frequencies known as the W-band, between 75–110 GHz, for which there are many applications. This range includes the 94 GHz transmission window in atmosphere. The possibility of high data rates and the crowding of communications at lower frequencies make the W-band a good communications channel. Though no commercial systems exist in the W-band yet, many research and military applications are already implemented. The Haystack Radar, shown in Figure 1-1 takes advantage of the transmission window in order to image objects in space. Gyrotron devices are used to power the system since they

Figure 1-5: The U. S. Military Active Denial System, which operates at 95 GHz. A humvee is necessary to move the equipment.

can provide the necessary high powers and bandwidths that are needed for operation. Figure 1-4 shows electronic warfare applications, such as a frequency jammer, which involves disrupting electronic systems with high power microwave and millimeter wave signals. These applications require very high power devices to disrupt appropriately and from a safe distance. There are many other communications capabilities that exist at 94 GHz, many involve devices installed on satellites and airplanes. As such, it is often necessary that the devices are robust, reliable, light weight, and have long operation life-times. Traveling Wave Tubes (TWTs), which will be discussed in the next section, satisfy these requirements.

Besides communications there are, of course, several other applications in the W-band of frequencies. Passive imaging systems to detect concealed weapons typically operate around 94 GHz. Intelligent cruise control in cars uses frequencies around 77 GHz to detect surrounding traffic. The Active Denial System (ADS) is a military application which uses a high-power beam at 95 GHz for non-lethal crowd control and

perimeter security; it is depicted in Figure 1-5. If the ADS is pointed at a human, the directed energy at about 95 GHz heats up water molecules that are present in skin and creates a near-instantaneous sensation of burning without causing any physical harm or injury to the subject. The subject will retreat from the area of directed energy, relieving oneself of the burning sensation. This is effective in creating an area of *denied access*, where people are unable to enter. It may also be used in riot control to disperse a crowd without causing physical harm. Unlike the rubber bullets or pepper spray that are used in these situations today, the ADS causes no physical harm to the subject. In its current iteration, the ADS system is large and cumbersome, requiring gyrotrons to power the high-energy beam and a large transport vehicle. In addition to being difficult to transport, it is currently incapable of covering a significant area due to power restraints of the gyrotron and the need for extremely directed energy.

This thesis focuses on the W-band, but there are a wide array of applications for higher frequencies. Communications channels, radar, and imaging at higher frequencies have increasing benefits in bandwidths, data rates, and resolutions. For example, there is another peak in the transmission through atmosphere at 220 GHz, which could have even larger bandwidths and data rates for communications. By focusing this thesis on the W-band, we are creating an increase in our capabilities to produce high power at high frequencies which can easily be converted to even higher frequencies in a future experiment. In this regard, the ability to scale the experiment to higher frequencies was kept under consideration. It is not enough to just design in the W-band, one must also think toward the future of our applications and the need for power within the Terahertz gap.

The development of Traveling Wave Tubes (TWTs) at high frequencies is significant because of their uses in wireless communications, satellite transponders, and electronic warfare applications. They are small, reliable, and efficient devices that provide high power for relatively high frequencies. The history of the device will be explored in the next section. Among the available vacuum electronic devices for the terahertz frequency range, TWTs are shown to be one of the most promising based off of previous experimental results and current TWT applications. Currently, TWTs

are one of the best amplifiers available in the W-band. Experimentally, they have reached average powers up to 100 W at 94 GHz. The only other amplifiers which outperform TWTs in the W-band frequency range are gyrotron devices, but they require superconducting magnets to operate. These devices are generally large and cumbersome making them impractical for many applications. TWTs offer a cheaper and more portable alternative.

Therefore, the development of a high power TWT at 94 GHz is of immediate practical use. In addition, there is a motivation to develop a new design for TWTs which has a size that is not as limited by the wavelength of operation as the traditional TWT design. A TWT of such a design would be able to easily be scaled to higher frequencies and bridge the Terahertz gap. An experimental TWT at 94 GHz with a novel cavity design is a profound scientific advancement.

1.2 A Brief History of TWTs

In the modern day, vacuum tubes are seen as a specialty field in electrical engineering. However, in the early twentieth century, even well into the 1970s, vacuum tubes were the core of electrical engineering studies. The various types of vacuum tubes were the dominant form of creating electronic systems up until the invention of the transistor in 1947. As the transistor and solid-state electronics emerged as the power-house for everyday, low power electronic devices, vacuum tubes still remained as the dominant driver in high power microwave systems. To this day, vacuum tubes are still the driving force of high power systems, and cannot be matched in performance by solid-state devices.

1.2.1 Vacuum Tubes and Radar

The first and most generic vacuum tube, the thermionic tube, was invented in 1907. These devices were the simplest form of an electronic switch and were the drive behind the first commercial electronic devices. In its most generic form, a vacuum tube consists of a cathode and anode which emit and accelerate electrons, respectively.

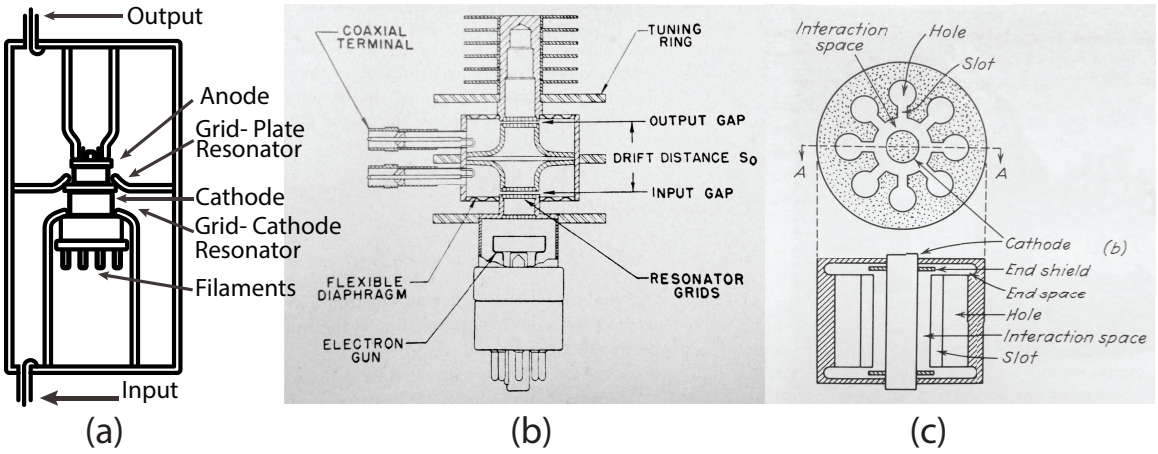

Figure 1-6: Early vacuum tubes diagrams of (a) a tetrode tube with resonators, (b) a klystron, and (c) a cavity magnetron [57], [25].

When a voltage is applied, the cathode emits and turns "on" the vacuum tube. Vacuum tubes are easily used to oscillate at certain frequencies, act as relays, or amplify signals due to a complex interaction between the electron beam in the system and an electromagnetic wave. An early tetrode tube is shown in Figure 1-6(a), which is designed to amplify a certain frequency.

As World War II approached, Britain began development of the first radar system in 1935. The first military demonstration used a BBC (British Broadcasting Corporation) transmitter in order to "see" airplanes passing near. The reflected radio signal from the planes was easily detected. The first radar system used triode thermionic tubes with large antenna towers. It operated at 11 MHz (but the frequency was quickly increased to 30 MHz) and able to detect airplanes up to 100 miles away despite weather conditions for low visibility [55]. These systems were installed along the coast of the UK to detect incoming airplanes, but it was quickly apparent that range and accuracy for detection would be a key component in developing a better radar system. It was also apparent that the installation of such a system on an airplane would lead to superior air defenses. These requirements led to a search for higher frequency components with high power signals.

The klystron was developed shortly after in 1937, by Russel and Sigurd Varian at Stanford. They were developing a small tube for radar which had enough power

to detect oncoming airplanes. The klystron, a powerful tube in its own right, is also important because it directed the military radar research that was being developed prior to World War II and led to the development of countless other vacuum devices. In a klystron, the electron beam travels from the cathode through a series of cavities which oscillate at specific frequencies when the beam passes through, as shown in Figure 1-6(b). The electron beam transfers energy into the electromagnetic wave in the klystron, creating an oscillation of the cavity frequency. If the klystron is driven by an input signal, it is possible to cause an amplifying device which creates a high power output signal in the electromagnetic wave at the input frequency.

During World War II, Germany developed radar systems with klystrons, but the U.K. developed radar systems which used a different device, the magnetron, that was able to provide higher power outputs. The magnetron was developed in 1939 by John Randall and Harry Boot in the UK based on previous similar devices; it is shown in Figure 1-6(c). This is the same device which, years later, would go on to power microwave ovens. (You probably have one in your kitchen.) Electrons from the center cathode are directed circularly with a magnetic field around the cavities and to the anode. The circular motion creates bunching and resonances that develop within the cavities of the magnetron. These resonances are able to be combined, leading to a high-power device. While klystrons were able to give decent power (about 500 W) at 500 MHz, the cavity magnetron provided about 50 kW at nearly 2-5 GHz, providing a phenomenal improvement in both power and frequency.

In a key collaboration between the U.S. and U.K. in 1940, the Tizard Mission sent one of the first magnetrons to the United States. The mission led to a key international exchange of radar technology. Once in the U.S., the MIT Radiation Laboratory and Bell Laboratories quickly optimized the magnetron output and put it into mass production as part of the war effort. The magnetron was a large component of the superior British air force in World War II, and was a large driving factor in winning the war. The success of tubes in radar systems led to the development of many known types of vacuum tubes and providing the scientific knowledge to pursue new tube designs after the war.

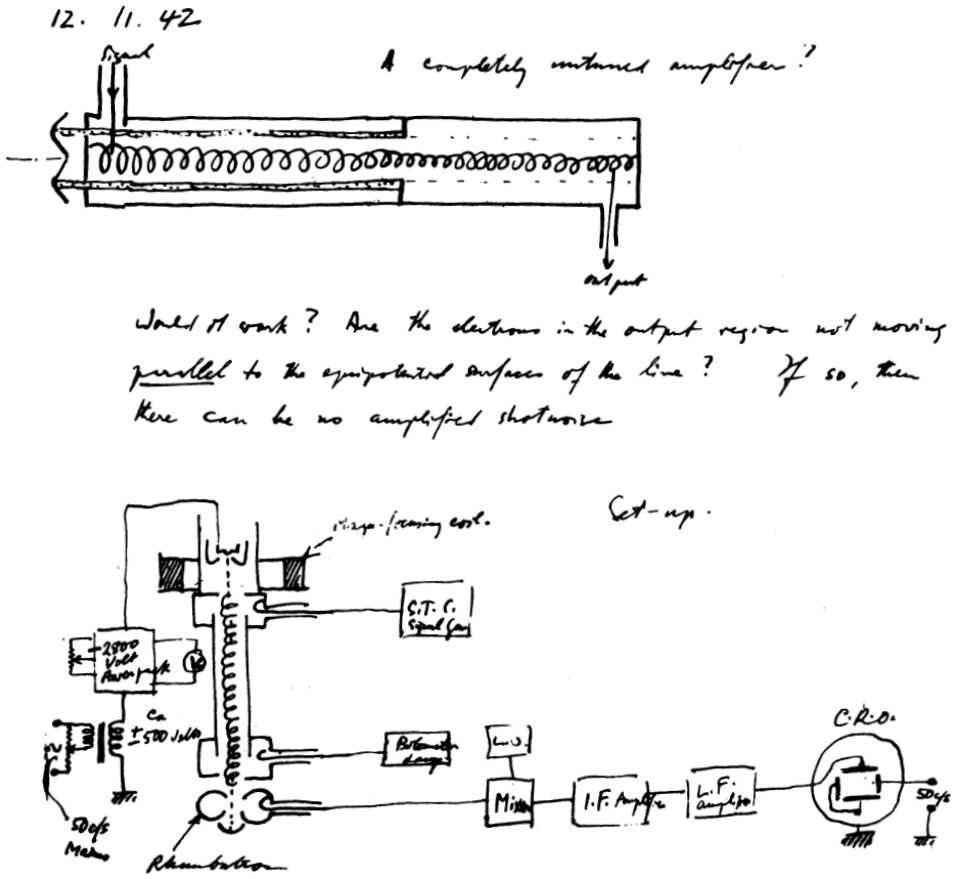

Figure 1-7: Drawings from Kompfner's notebook in 1942, when he first began work on the helical TWT. First, the TWT concept is shown with a hollow electron beam, traveling outside of the helix. Kompfner supposed it would be a "completely untuned amplifier" and questioned, "Would it work?" Second, a diagram of the first TWT experiment is depicted, which has a solid pencil beam traveling through the center of the helix [39].

1.2.2 Invention of the TWT

While working on the magnetron and related radar technology in the U.K., Rudolf Kompfner developed the initial idea for the Traveling Wave Tube Amplifier (Abbreviated TWAT or TWTA in some publications, but more commonly simply called a TWT). Figure 1-7 shows drawings from his 1942 notebook. The design involves sending an electron beam through a slow-wave circuit; in this case, the circuit is a helical wire which acts as the center of a coaxial input line. The helical wire slows down the phase and group velocity of the electromagnetic wave traveling through the device, such that the phase velocity of the wave matches the velocity of the beam.

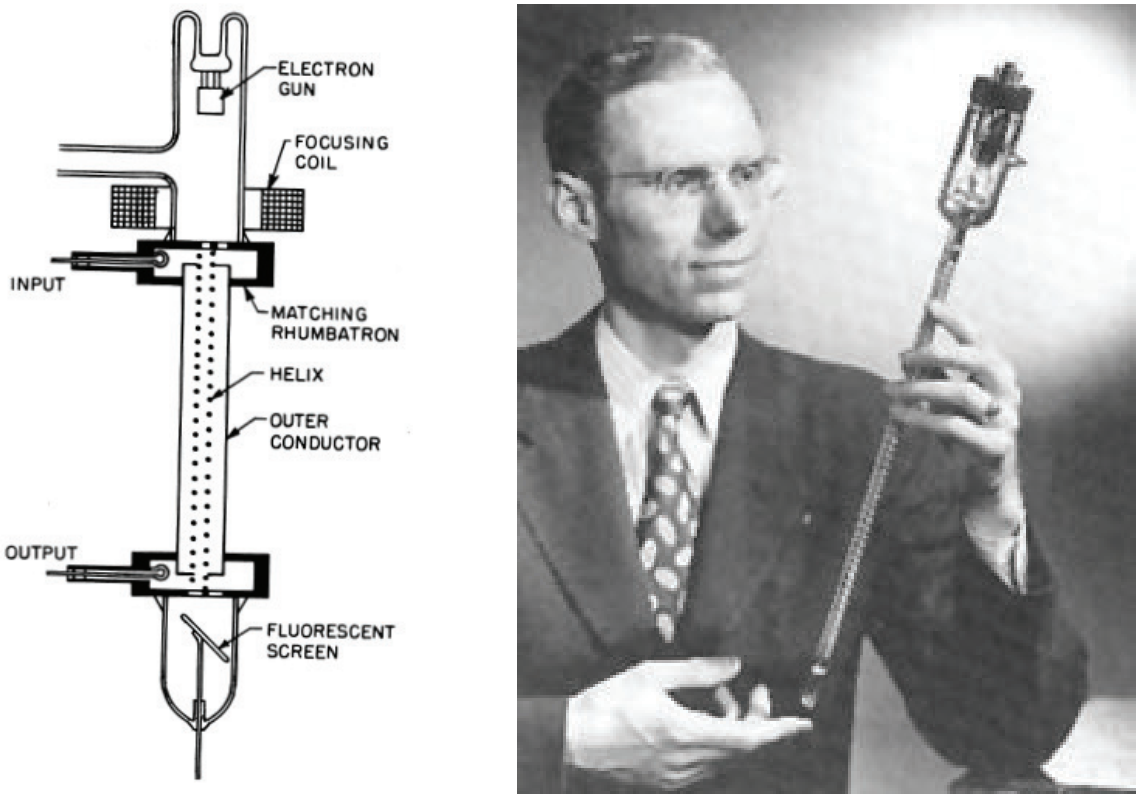

Figure 1-8: A diagram of the first TWT experiment from Kompfner's laboratory and a picture of John R. Pierce holding one of the first successful TWTs [39] [55].

Energy can transfer from the beam into the wave and amplification can occur. This device was proposed as an untuned amplifier, meaning that the device would have a significant bandwidth in comparison to its klystron and magnetron counterparts. A detailed drawing of the TWT is shown in Figure 1-8. A focusing magnetic coil along with other magnets (not shown) direct the electron beam through the device, while a matching input and output circuit couple to the electromagnetic wave that is amplified. A detailed theory of the TWT will be provided in Chapter 2.

Near the end of World War II, Kompfner and John Pierce worked together on developing the theory and optimizing the output power and bandwidths of a working TWT experiment. The goal was to develop a low-noise device that could be used in radar and communications applications. John Pierce is shown in Figure 1-8 holding one of the first successful TWTs. The helical TWT was shown to be a highly efficient and high bandwidth device with low noise, up to 80 % efficiency, and the capability

for an octave of bandwidth (50%) [55]. Though Kompfner invented the TWT, Pierce is credited with developing the theory which ultimately led to a successful device.

The development of other types of TWTs followed. Though the helical TWT is a high bandwidth device, it has low output powers and gain characteristics. For radar transmitting, high power and gain is often necessary. In the basic theory of a TWT, a slow-wave device must be used; this device can be anything which causes the electromagnetic wave to travel at a slow velocity (less than the speed of light) such that it can be phase-matched with the electromagnetic wave. In each device, the theory remains the same, and the phase velocity of the wave can be calculated via electromagnetic field theory. Different types of TWTs led to different ranges and design trade-offs for bandwidth, gain, and power.

Using concepts from accelerator physics, high power TWTs were developed. The folded waveguide TWT is a design which uses a meandering (or serpentine) waveguide structure and a beam tunnel that cuts through the waveguide. The wave is slowed down relative to the electron beam by traveling a longer distance through a rectangular waveguide structure that folds repeatedly across the beam tunnel axis. When the beam passes through the meandering structure, it interacts with the wave. A cooling system on the folded-waveguide TWT allows for it to be more powerful than the helical TWT, while maintaining a relatively high bandwidth. Similarly, in a coupled-cavity TWT, the electromagnetic wave couples through subsequent cavities along the electron beam line, in much the same way as the folded-waveguide structure. The coupling from one cavity to the next slows down the phase velocity of the wave to match the electron beam. The coupled cavities allow for a high power device due to the strong resonances that occur in the circuit. However, the cavities are frequency specific, and the highest achievable powers are only obtained by limiting the bandwidth capabilities of the circuit. The coupled-cavity TWT will be discussed further in Chapter 2. The varied array of possibilities with TWTs mean that a device can easily have an optimized, gain, power, and bandwidth which best suits the needs of the application at hand.

1.2.3 More Vacuum Devices

The development of the klystron, led to an array of vacuum devices that all used very similar concepts of phase-matching between the electromagnetic wave and the electron beam. These devices can be split into slow-wave devices (like magnetrons and TWTs), where the phase velocity of the wave is less than the speed of light such that the velocity matching occurs, or fast-wave devices (gyrotrons), where the phase velocity of the electromagnetic waves travel faster than the speed of light and RF interaction occurs via the angular velocity of the electron beam. It is also worth mentioning backward-wave oscillators, which are slow-wave devices that use resonances within a circuit similar to a TWT structure. The resonances cause oscillations (instead of amplifications) with a negative group velocity wave in the structure. This leads to a high power output device with a tuned frequency.

When it comes to high power in millimeter waves, no other device can match the achievements of the gyrotron. Gyrotrons are fast-wave devices which can operate as either oscillator or amplifier circuits. In gyrotrons, an annular (or hollow) electron beam is bunched azimuthally with the electric field. Gyrotron oscillators are capable of achieving extremely high output powers (more than megawatts of power) at the highest frequencies of any vacuum device, up to 100 GHz and above. Gyrotron amplifiers are capable of producing high gain at those frequencies, as well. Gyrotrons at even higher frequencies exist, and many designs are being pursued to bring gyrotron devices into the Terahertz gap. In practical applications however, gyrotrons are often seen as cumbersome; they often require high magnetic fields (10 T) which must be achieved with a superconducting magnet and are not robust to alignment issues within the magnetic field, making them hard to transport and maintain. Though gyrotrons have many applications, gyrotron devices placed in airplanes or satellites are not a practical implementation.

1.3 Modern Day W-Band Vacuum Tubes

Many advancements in vacuum tubes have occurred since the development of the device in the 1940s and 1950s. With the advent of highly accurate computer-driven simulations and optimized designs, many devices which could not be completely derived and understood with direct theoretical calculations can be explored without much experimental cost. In addition, machining techniques have improved, making practical implementation in the W-band easier to achieve. As such, tubes at high-frequencies have been rapidly developed in recent years.

After extensive development in the 1960s, helical TWTs have been demonstrated to provide about 1 kW of power at 10 GHz. Helical TWTs also have large bandwidths, providing up to two octaves of bandwidth at lower frequencies [21]. Folded waveguide and coupled cavity TWTs operating in the fundamental mode were developed shortly after and shown to provide approximately 100 kW of power with 10 % bandwidth up to 10 GHz in frequency [20], [37]. Scaling to higher frequencies is difficult due to small wavelengths and proportionally small structures that are difficult to manufacture.

1.3.1 W-Band TWTs

In the W-band, vacuum tube designs must deal with smaller wavelengths than the original TWT designs. (Wavelengths in this frequency range are from 4 mm to 2.7 mm.) Small operation wavelengths lead to mechanical difficulties in experimental implementation. At 94 GHz, the wavelength of about 3.2 mm means that components that interact with this wavelength will be much smaller in size. When dealing with a TWT, this scaling also means that the electron beam must be subsequently smaller in size and will be traveling through a small beam tunnel, too. Beam compression is incredibly difficult at small sizes, and leads to extremely large magnetic fields necessary for TWT operation. (The concept of Brillouin flow will be discussed in Chapter 2.) Due to these limitations, development of high power TWTs in the W-band is not straightforward.

One of the most successful W-band TWTs was a cylindrical coupled-cavity ladder

circuit known as the Bill James Tube developed in 1986 at Varian. With a 20 GHz bandwidth, it achieved up to 100 W continuous (CW) power and 1 kW peak output pulsed power [34], [33]. In the 25 years since, W-band TWTs have only achieved 50-100 W average power with less than 5 GHz bandwidth.

Commercially, W-band Coupled-Cavity TWTs are available with limited output power today. Off the shelf, a W-band TWT with 50 W output power from 93 to 95 GHz can be purchased from Communications & Power Industries (CPI), a company that specializes in vacuum tube manufacturing. With a limited bandwidth, a TWT with 3 kW peak power with pulsed operation can be purchased from CPI. Wide bandwidth, helix TWTs are not commercially available in the W-band. At that frequency the necessary helix size is simply too small for operation since manufacturing the small helix is difficult and transmitting a significant electron beam through the helix requires a large magnetic field (10 T or higher is not achievable without a superconducting magnet).

Higher power TWTs are in development at industry locations as well as research labs. Research at L-3 Communications has shown the capabilities to produce a coupled-cavity TWT with 4 GHz of bandwidth and 75 W average output power for pulsed operation (150 W peak power) at 94 GHz [43]. Most notably, a complex integral-pole-piece-ferruleless-coupled-cavity folded-waveguide circuit was capable of 100 W average power, 30 dB of gain, and 1 % bandwidth [68]. The high average power of the device was obtained through sacrificing bandwidth in the circuit, making a strongly resonant coupled-cavity device. Recent research at the Naval Research Lab has used a 3-stage folded-waveguide TWT circuit with a 3-beam electron gun, though results are forthcoming [51].

In addition, theoretical analysis of many types of structures for W-band TWTs shows the limits of fundamental structures and diverse range of ideas to circumvent those limits. These investigated structures include a micro-fabricated helical structure with two electron beamlets [41], a suspended ladder structure [42], a wood-pile electromagnetic-bandgap waveguide [16], groove-loaded folded waveguide [27], or selectively metalized micro-fabricated folded waveguide [62]. A cylindrical dielectric

omniguide photonic band gap TWT was in development with a 10 % bandwidth expected [64], but achieved limited success. None of these designs have been successfully implemented in experiment and all would require small electron beam radii with large currents and significantly larger magnetic fields than lower frequency TWTs in order to achieve high gain conditions.

Success has come using UV-LIGA fabrication techniques. A 50 W, 220 GHz folded waveguide TWT was successfully built at the Naval Research Lab [36]. The small device, with a beam tunnel of about 100 microns, uses a patented UV-LIGA method which is susceptible to small manufacturing and alignment errors. With the development of a manufacturing process for small components, devices at high frequencies will see larger possible gains in the coming years. However, the sizes of the components at these frequencies puts a very strict limit on the peak output power that can be safely handled by the devices.

Development in TWTs has also focused on complex electron beam formation. Sheet beams, which are elliptical, as opposed to circular, solid electron beams have been successfully used in experiments [53] [18]. In addition, multiple-beam TWTs have up to 8 circular beams in a single device [52]. These devices are successful, but they often require extremely precise magnetic fields and complex beam focusing mechanisms.

1.3.2 Other W-Band Devices

Gyrotron oscillators are capable of producing extremely high output powers in the W-band. Fueled by ITER, 1-2 MW gyrotron tubes are in development at 170 GHz. W-band devices are also achievable with over 1 MW of output power. These designs often have interactions in over-sized cavities and operate in an extremely high-order mode in order to maximize interaction with an azimuthal beam [30], [38], [46], [7]. They are phenomenal devices, but require significant magnetic fields and extremely high voltages to operate.

Extended Interaction Klystrons and Oscillators (EIKs and EIOs) in the W-band have produced extremely high power as well. Commercially, an EIO can be purchased

which gives up to 1 kW of power in the W-band. However, the instantaneous bandwidth of operation is limited, at only 250 MHz for high power devices [58]. Larger bandwidths, up to 2 GHz are available for devices with less output power [31].

Solid-state devices are also not to be ignored. With advances, Amplifier Multiplier Chains (AMCs) are capable of producing significant power in the W-band and are extremely efficient. Though expensive, purchasing a solid state device which produces 50 mW of power across 10 GHz in the W-band is reasonable [48]. AMCs have a distinct scale between power and bandwidth. Devices are available with large bandwidth, 20 mW over the entire entire W-band (75-110 GHz), or high power, 3 W over 4 GHz [49] [61]. Though 3 W is hardly considered high power for vacuum devices, it is a great achievement for solid-state amplifiers. AMCs can be cascaded together, but reaching high powers is often prohibitively expensive, especially as the available power in solid-state devices rapidly drops off at higher frequencies.

The TWT has been shown to be a robust and capable device for numerous applications. It is seen as one of the most practical vacuum tubes for modern-day endeavors, capable of producing high power and high frequency. It is also an extremely reliable device, already used for many space applications. Though devices with better output power characteristics exist at 94 GHz, it is the goal of this thesis to develop a TWT for these reasons.

1.3.3 Overmoded TWTs

Overmoded W-band TWTs have been proposed which would allow the possibility of larger beam tunnels and the need for less magnetic field overall [9], [10], [22]. An overmoded design, meaning a design which operates in a cavity mode which is at a higher frequency than the fundamental cavity mode, is oversized for its intended frequency of operation. By operating in a higher order mode, the overmoded design offers the possibility of creating a larger device than the fundamental coupled cavity equivalent at the same frequency. An oversized device offers many benefits that can lead to higher gain and power in the TWT; these benefits will be explored in this thesis.

Sheet beam EIKs are oversized devices that have been shown to be successful at high frequencies and the technology could be applied to TWTs. By nature, these devices are oversized for their intended frequency of operation, though they operate in the fundamental device mode. The elliptical beam structure takes advantage of peaks in the electric fields of the mode in the cavity or folded waveguide [53] [44]. Though moderately successful, strong and precise magnetic fields must be used to successfully implement these devices due to the complex electron beam.

1.4 Overview of Thesis

This thesis will develop and experimentally test a novel 94 GHz overmoded coupled-cavity TWT. Overmoded TWTs were first explored at MIT by [10]. The design presented in this thesis is for a 94 GHz TM_{31} cavity mode with lower order modes suppressed by selective dielectric loading. With the goal of experimental validation, the design considers the practicality, manufacturing, and experimental testing of the overmoded TWT. As the first experimental validation of an overmoded TWT, this experiment will further expand the use of TWTs to higher frequency ranges, impinging on the terahertz gap. The experimental success of an overmoded W-band TWT will offer the possibility of scaling to higher frequencies and expanding to other modes for operation.

In this thesis, Chapter 2 will discuss the theory of TWT design. Chapter 3 will cover the design of an overmoded TWT circuit and Chapter 4 will discuss low power testing of the cavity. Chapter 5 will discuss the experimental implementation of the overmoded TWT, including the electron gun and solenoid magnet design. Chapter 6 will discuss the electron gun beam test and overmoded TWT experiment results. Finally, Chapter 7 will discuss conclusions from the overmoded experiment.

Chapter 2

Theory of Traveling Wave Tubes

The equations that govern Traveling Wave Tube (TWT) amplification and operation are easily described using theory derived from Pierce, and further refined over the decades, to describe different slow-wave structure interactions. This chapter will first consider an overview of the TWT interaction. A discussion on the electron beam compression with the magnetic field considerations will follow. Finally, there will be a detailed analysis of the slow-wave structure and beam-wave interaction theory.

2.1 TWT Overview

First, consider the generic TWT circuit, as shown in Figure 2-1. In this figure, an electron gun produces a beam of a specific quality. The electron beam is solid, typically round, and it is often described as a "pencil beam." It is confined and directed by a magnetic field along the $\hat{z}$-axis of the system and travels through a TWT interaction structure, as described in the next section. An electromagnetic wave is fed into the interaction structure, which interacts with the electron beam and gains energy along the length of the structure before exiting. The structure and beam-wave interaction will be described in Section 2.3 along with interaction equations. After the interaction structure, the beam exits the confining magnetic field, expands, and is deposited on a collector. All of these components are outlined in Figure 2-1 for simplicity. The beam, shown in pink, travels through the slow wave

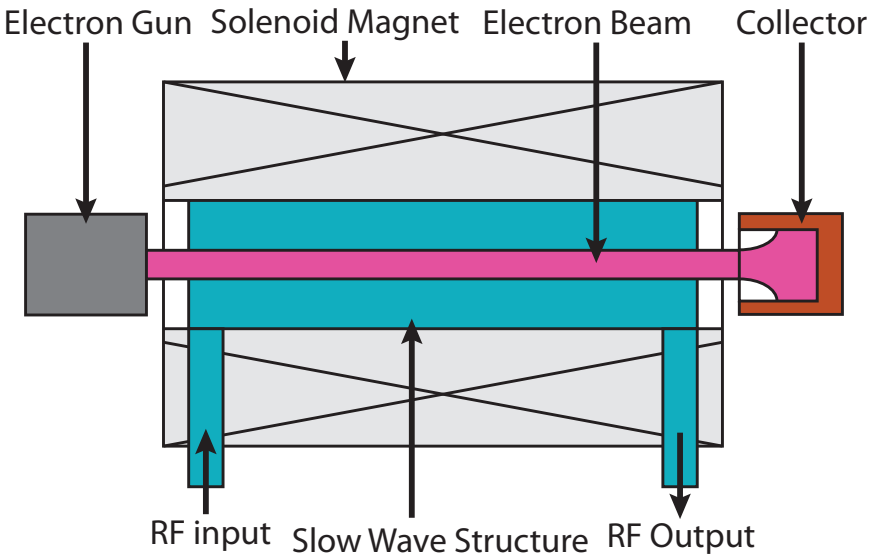

Figure 2-1: A block diagram overview of a TWT amplifier circuit. The electron beam (pink) travels from the electron gun (gray), through the slow wave structure (cyan) which is surrounded by a solenoid magnet, and to the collector (orange).

structure, shown in blue. A solenoid magnet surrounds the structure and confines the beam. The electron beam, magnet, and slow-wave structure are the three main parts of a TWT and will be described in detail in the subsequent sections.

For now, let's simply understand that the electron beam must be formed to a small diameter and confined over a length of space via the magnetic field. The velocity of the electron beam must be in synchronous operation with the electric field in the slow-wave structure. This means that the phase of the electric field must travel at the same velocity as the electron beam. This concept is illustrated in Figure 2-2, which shows a generic plot of the electric field along the longitudinal length, or $\hat{z}$-axis, of the TWT device. Since the electric field and electrons are traveling at the same velocity, some of the electrons will perpetually see a $+\hat{z}$-directed accelerating field and some will see a $-\hat{z}$-directed decelerating field, as shown in the cut-out from the figure. This interaction leads to electron bunches forming along the longitudinal axis of the interaction. After the bunch is formed, the electron beam transfers energy to the electromagnetic wave over a length of space, and the wave sees exponential growth in power. At the end, the field reaches saturation once the electron beam begins to lose energy and de-bunches after falling into the decelerating field of the

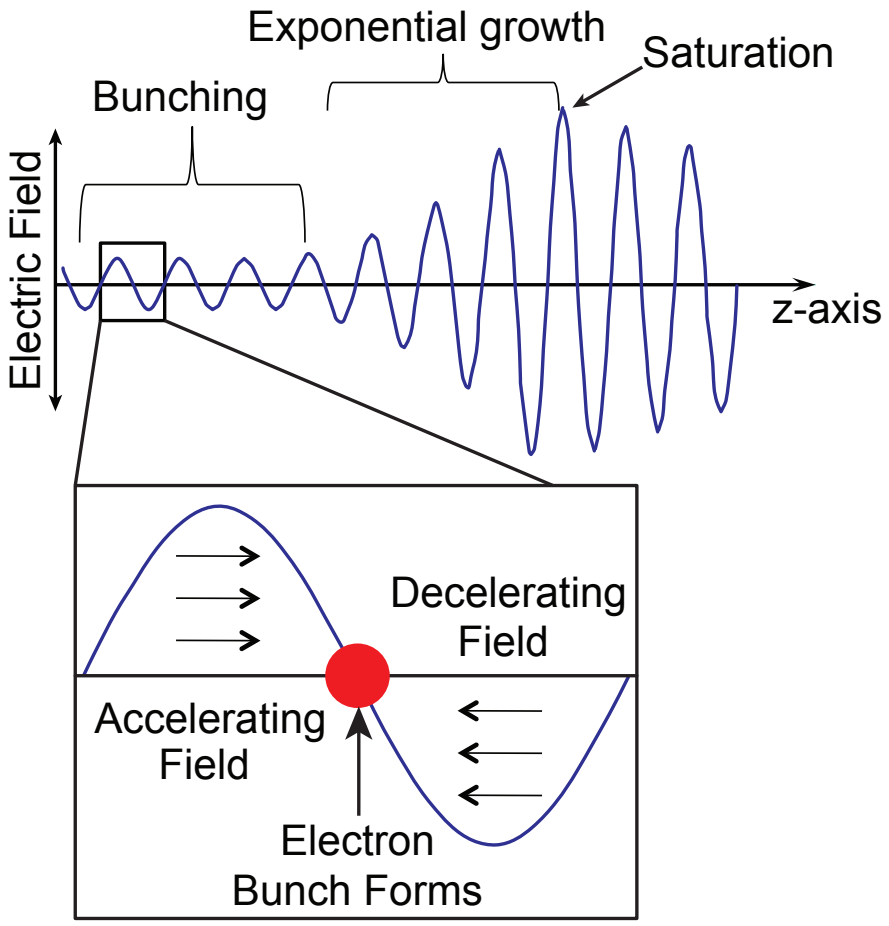

Figure 2-2: A generic graph of the $\hat{z}$-directed electric field in the TWT along the beam tunnel of the TWT. In the bunching region, electrons in positive field are accelerated, and electrons in negative field are decelerated, forming bunches.

RF wave.

The complex equations to describe this interaction will be explained in Section 2.3, but the key take-away is that the beam and wave should travel at the same speed, causing a consistent interaction over the length of the structure, and transferring energy from the electron beam into the electromagnetic wave. This energy transfer causes the amplification of the electromagnetic wave in the circuit. The rest of this chapter will be dedicated to explaining this interaction in detail.

2.2 Electron Beams in Vacuum Tubes

A key component of a TWT is the electron beam that will be used for the interaction. In high frequency tubes, a well-formed electron beam is necessary to travel through the small beam tunnel of the circuit. Though there are several ways to go about making an electron beam, this project utilizes a simple, single-beam Pierce electron gun with a thermionic cathode, which will be described in this section.

2.2.1 Pierce Electron Gun

In its simplest form, an electron gun consists of a cathode and an anode. In general, the cathode has a reservoir of electrons and is biased by a negative voltage relative to the anode, which is grounded. The cathodes considered here are thermionic cathodes, meaning that they are heated to a certain temperature and that a reservoir of electrons, typically tungsten and barium based, is activated. The electrons at the cathode have a low work function due to the barium. Therefore, when a voltage is applied to the cathode, electrons easily emit from the surface. Figure 2-3(a) shows the generic set-up. In this instance, the cathode releases electrons that accelerate over the gap between the anode and cathode, this space is often referred to as the A-K gap. When the electrons reach the anode, their speed, v_e, as determined by conservation of energy is

$$v_e = c\sqrt{1 - 1/\gamma^2} \tag{2.1}$$

and

$$\gamma = 1 + \frac{V_0 \text{ [kV]}}{511 \text{ [kV]}} \tag{2.2}$$

where V_0 is the voltage between the electrodes (in kV), and c is the speed of light.

The current emitted from the cathode has two possible limitations: temperature and space-charge. In general, the larger factor to consider is temperature. A thermionic cathode has a maximum current density that it can emit for a given temperature of operation. This limit ranges between 1 A/cm^2 to 100 A/cm^2 at the surface, depending on the type of cathode, operation temperature, and lifetime considerations

of the device. A longer lifetime circuit, will have a smaller acceptable current density on the cathode. Pierce guns, however, are intended to operate below the temperature limited regime, and in the space-charge limited regime. At this operating condition, the cathode voltage, V_0, limits the current that can be extracted from the cathode due to space-charge forces within the beam. That is, the repulsion of the electrons between themselves is the limiting factor in extracting current from the cathode. The limit can be determined via Poisson's Law.

$$\nabla^2 V_0 = \frac{\rho}{\varepsilon_0} \tag{2.3}$$

The charge density is related to the current density, such that $J_0 = \rho v_e$, with $v_e = \sqrt{2\eta V}$, where η is the charge-to-mass ratio of electrons (note that this is the same as eq. (2.1) if $V_0 \ll 511$ kV). Consider that the electrons are traveling only along the $\hat{z}$-axis, then the equation can be reduced to,

$$\frac{d^2 V_0}{dz^2} = \frac{J_0}{\sqrt{2\eta V}\varepsilon_0} \tag{2.4}$$

This equation can easily be solved for the Child-Langmuir equation, which provides a relationship between current density and voltage in a space-charge limited electron gun, such that [37]

$$J_0 = \frac{4}{9}\varepsilon_0 (2\eta)^{1/2} \frac{V_0^{3/2}}{d^2} = 2.33 \times 10^{-6} \frac{V_0^{3/2}}{d^2} \tag{2.5}$$

For a practical electron gun, the Child-Langmuir relationship can be written in a more generic form for a finite cathode area,

$$I_0 = P V_0^{3/2} \tag{2.6}$$

Where I_0 is the total current in the electron gun, and P is the perveance of the gun, which is defined as

$$P = \frac{4}{9} \frac{A\varepsilon_0}{d^2} (2\eta)^{1/2} = 2.33 \times 10^{-6} \frac{A}{d^2} \tag{2.7}$$

where A is the area of the cathode and d is the distance between the anode and cathode [37]. As such, the perveance (typically with units of micropervs) is a defining factor of the electron gun which describes the current limitations of the gun, and the relationship between current and voltage in the gun.

In essence, current is proportional to $V_0^{3/2}$. At operating voltages, a Pierce electron gun should follow the Child-Langmuir limitation of current density. For higher voltages, the gun will reach a maximum, temperature limited, current output. For a Pierce electron gun, a space-charge limited operation is ideal. This allows for the beam to be self-modified, and leads to a better confined beam within the circuit that can easily be directed with appropriate magnetic fields.

Though simple, modeling the electron gun as two parallel plates, as shown in Figure 2-3(a), has many practical problems. To begin, it requires two infinitely large planes, which cannot be practically realized. The electron beam, also, must have some space in which to interact with the slow-wave structure, requiring some sort of beam tunnel to propagate through the anode. In addition, the set-up offers no compression of the beam. Space-charge limited, thermionic cathodes will only emit small amounts of electrons over their surfaces, typically 10 A/cm^2 is the upper limit of emitted current density for a thermionic cathode with a decent lifetime. However many applications require a large density of electrons that is difficult to achieve with thermionic emission. These two properties lead to a compression of the electron beam between the cathode and anode being necessary. Figure 2-3(b) shows a simple set-up of two spherical electrodes, which would have a larger density of electrons at the anode than at the cathode. In this case, the velocity of the electrons is still defined as in equation (2.1), and the Child-Langmuir limit is still applicable.

An even more practical set-up is shown in Figure 2-3(c), where the spheres have been reduced to smaller surfaces. This allows for a circular spot of electrons to form at the anode. The velocity is the same, but the edges of the beam need to be contained. In general, electrons will travel along lines parallel to the equipotential lines formed by the anode-cathode configuration. In Figure 2-3(a), the equipotential lines are parallel to the anode and cathode, so the flow of electrons is simply straight across the gap.

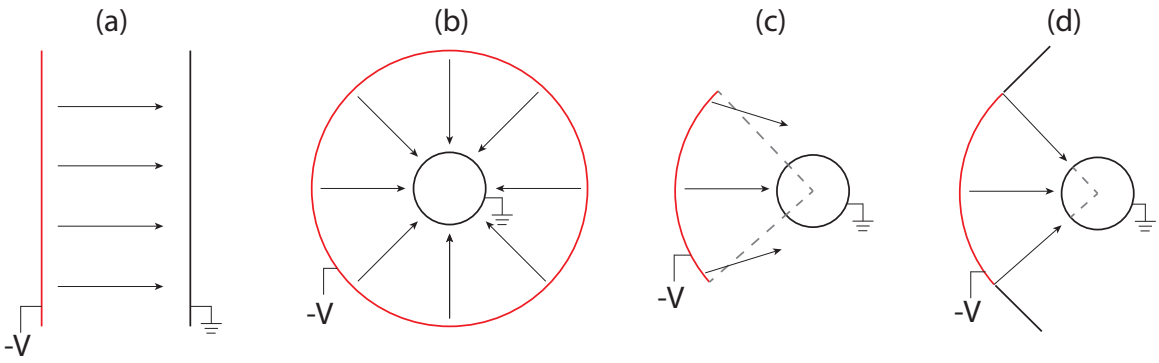

Figure 2-3: Diagrams with different anode-cathode configurations to demonstrate the compression of electrons between the A-K gap.

In Figure 2-3(b), the equipotential line are concentric circles between the anode and cathode, leading to another simple flow of electrons directly between the cathode and anode. However, in Figure 2-3(c), the equipotential lines are more complicated, straitening out and curling around the two electrodes. Due to this configuration, electrons along the edge of the beam will not be confined.

If the outer emitting sphere were simply cut like in Figure 2-3(c), the electrons would repulse each other and not form a coherent beam. Figure 2-3(d) solves this problem. Focusing electrodes are added to the edges of the partial spherical surface of the cathode. These electrodes are at the same voltage as the cathode, but they do not emit electrons; they provide an electric field outside the partial sphere of the cathode to help to focus and maintain the electron beam shape. This addition changes the shape of the equipotential lines, such that the electrons forming at the edge of the cathode see a parallel equipotential, and move perpendicular to the cathode surface. The equipotentials direct the beam to a confined spot at the center of the anode. The angle of the focusing electrodes can be calculated by assuming planar flow of electrons near the edge of the beam. That is, if we zoom into the edge of the cylindrical electron beam, we can assume that the electrons are traveling locally only in the $\hat{z}$-direction. In this case, Poisson's equation leads to boundary conditions at the space along the edge of the beam to produce a straight electron flow [37],

$$\frac{\partial V}{\partial y} = \frac{\partial V}{\partial x} = 0 \tag{2.8}$$

This condition defines linear equipotentials along the beam line between the electrodes. Equation (2.5) can be rewritten, such that

$$V_0 = \left(\frac{J_0}{2.33 \times 10^{-6}}\right)^{2/3} d^{4/3} \tag{2.9}$$

where d is the distance between the anode and cathode. Taking the anode to be at $+V_0$, the cathode to be at ground, and solving for the boundary conditions in polar coordinates, the line at which V=0 is defined as:

$$\cos\frac{4}{3}\theta = 0 \tag{2.10}$$

where θ is the angle between the focus electrode and the edge of the electron beam. This equation defines the line of the focusing electrode, which requires that $\theta = (3/8)\pi$, or $\theta = 67.5°$. In other words, the focusing electrode placed at 67.5° away from the edge of the beam, will cause equipotentials between the cathode and anode that appear as concentric circles for the beam. This means that the electrons will travel along straight lines between the anode and cathode [37].

Figure 2-4 shows the general set-up for the cathode and anode of an electron gun, using the modified spherical geometry. A hole in the anode has been introduced to allow the beam to pass through the anode. After the anode, it will interact with the slow wave structure. At the location of the anode, the electrons will be traveling with velocity, v_e. The compression of the gun is determined by the radii of the two electrodes and the spacing between them. Ideally, the electrode spheres are centered at the same point, such that the A-K gap is equal to $R_c - R_a$, but in practice, these are often offset in order to get a better compression of the beam.

The minimum beam diameter is determined after the cathode-anode interaction and is a product of the space-charge interaction in the beam and the focusing forces of the electron flow. Figure 2-5(a) illustrates the beam compression without an external magnetic field. The edges of a solid electron beam are illustrated, showing that the beam compresses to the minimum diameter, b_{min}. Subsequently, the beam expands

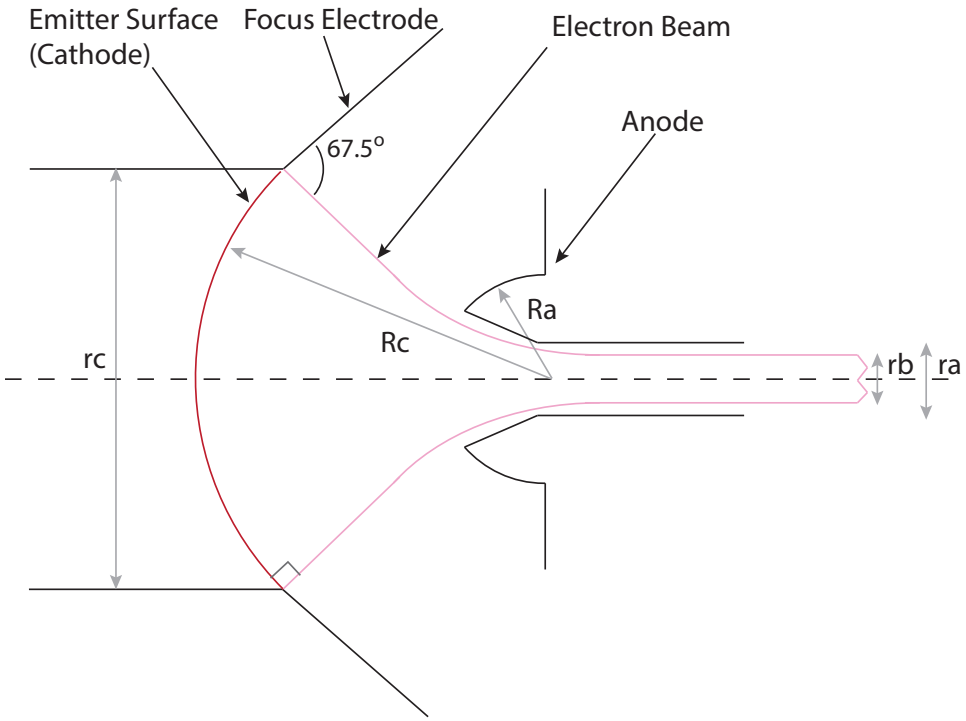

Figure 2-4: A diagram showing the ideal design of a Pierce electron gun, with the emitter surface highlighted in red, and the electron beam shown in pink.

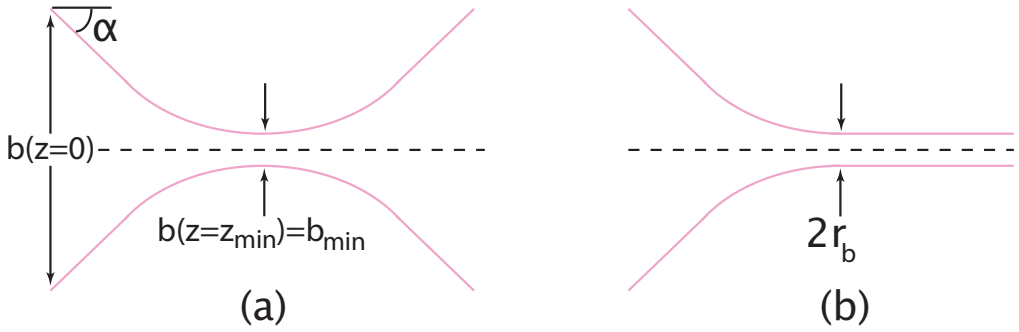

Figure 2-5: (a) The electron beam compression and minimum beam radius. (b) Magnetic field confinement of the beam after the minimum beam radius has been formed.

after the minimum diameter is reached due to repulsion forces. This figure considers no magnetic fields, and the beam is outside of the cathode-anode configuration, meaning that the only forces on the beam are a result of space charge. As such, the universal beam spread equation defines compression and divergence of the beam.

$$\frac{d^2b}{dz^2} - \frac{\eta I_0}{2\pi b \varepsilon_0 v_e^3} = 0 \tag{2.11}$$

where b is the diameter of the electron beam and z is the axial direction of propagation. The equation can be simplified by introducing a constant parameter, D, such that

$$D^2 = \frac{\eta I_0}{2\pi\varepsilon_0 v_e^3} = \frac{1}{\pi\varepsilon_0\sqrt{2\eta}}\frac{I_0}{V_0^{3/2}} = (174\sqrt{P})^2 \tag{2.12}$$

and

$$\frac{d^2b}{dz^2} - \frac{D^2}{2b} = 0 \tag{2.13}$$

By substituting for the parameters in Figure 2-5(a), we can obtain an equation for the beam diameter.

$$B = e^{(dB/dZ)^2 - (dB_0/dZ)^2} \tag{2.14}$$

where $B = b/b_0$, $Z = Dz/b_0$, and $b_0 = b(z = 0)$. At the minimum beam diameter, $dB/dZ = 0$, so the minimum beam diameter, b_{min}, is determined as

$$B_{min} = \frac{b_{min}}{b_0} = e^{-(dB_0/dZ)^2} = e^{-(\tan\alpha/D)^2} \tag{2.15}$$

with D defined above, and the angle α defined in Figure 2-5 [37]. In reality, thermal velocities of the electrons will disperse the beam, and achieving this predicted minimum beam diameter is impossible. However, by changing the shape of the cathode radius and other dimensions of the electron gun, the beam can be shaped to achieve whatever beam diameter is necessary for the application.

Note that beams which are compressing sharply, with a large angle, α, will have a smaller beam diameter than those which are compressing more gradually. This analysis is a way to easily manipulate the electron beam and design an electron gun with the appropriate beam diameter for use in the slow-wave structure. Next, a magnetic field will be introduced that prevents the divergence of the beam, so that the electron beam can be used with the small radius. With an appropriately matched field, the beam will stay compressed due to matched forces, as shown in Figure 2-5(b).

2.2.2 Magnetic Field Confinement

Magnetic field was not mentioned in the role of the electron gun, but it is a major influence on the formation of the beam and direction of the beam after the anode. The magnetic field influences the beam in two parts. First, the peak magnetic field keeps the beam confined to the minimum beam radius over a distance. Secondly, the compression of the beam is influenced by a matched magnetic field, which is near zero at the cathode, and grows to the peak field at about the location of the minimum beam radius. The combination of these two fields, if perfectly matched to the beam, results in a compression which looks like Figure 2-5(b). In this section, we will discuss solenoid magnetic field focusing with Brillouin flow, however other types of focusing are often used, such as Periodic Permanent Magnet (PPM) focusing, which results in a laminar flow of the beam.

For solenoid focusing, the peak magnetic field must be large enough to counteract the space-charge forces of the electron beam and keep the beam confined to the minimum beam radius. A solenoid magnet is placed around the beam tunnel, such that the magnetic field is $\hat{z}$-directed and is near zero at the cathode. The field limitation for confined flow is called the Brillouin field, and can be solved by analyzing the forces on the beam and the equation of motion for the electrons. The result is that the beam is confined when the Larmor frequency, $\omega_L = \omega_c/2$, satisfies the equation:

$$\sqrt{2}\omega_L = \omega_p \tag{2.16}$$

where ω_p is the plasma frequency of the beam. Substituting for these two frequencies, and solving for the Brillouin magnetic field, B_B,

$$B_B = \sqrt{\frac{2mI_0}{\varepsilon_0 \gamma e v_e \pi r_b^2}} \tag{2.17}$$

where r_b is the radius of the beam and all of the parameters are already known quantities of the electron beam. This equation can be rewritten using the Alvén

current, $I_A = 17$ kA.

$$B_B = \sqrt{\frac{8m^2c^3 I_0/I_A}{\gamma e^2 v_e r_b^2}} \tag{2.18}$$

Note that the ability of the Brillouin field to cause confined flow is the case for Brillouin flow, where the field at the cathode is zero. For immersed flow, where the magnetic field at the cathode is not zero, the magnetic field required for balanced flow is slightly larger. If the field is not matched to the beam, a ripple in the radius of the beam will develop as the beam travels along the $\hat{z}$-axis. Insufficient magnetic field will result in a ripple that is larger than the minimum beam radius, whereas excessive magnetic field will lead to an over-compressed beam with a ripple smaller than the ideal radius.

Secondly, the compression of the beam is influenced by the magnetic field at that location. In a thermionic, space-charge limited cathode, the magnetic field is near-zero at the cathode for Brillouin flow. Alternatively, for immersed flow, there is a field at the cathode. In either case, as the beam is compressed, the magnetic field should grow in a matched method. The addition of an magnetic pole piece, a piece of ferrous material, such as iron, and/or an opposing-field gun coil magnet can help to match the beam and the field. A pole piece disturbs the magnetic field in a very predictable way. For instance, if a thin pole piece with an aperture of size radius r_{pole} is placed at z=0 next to a solenoid magnetic which provides $B_z(z > 0) = B_0$, then the magnetic field can be described as

$$B_z = B_0 \left(\frac{1}{2} + \frac{1}{\pi} \tan^{-1} \left[u + \frac{u}{1+u^2} \right] \right) \tag{2.19}$$

where $u = z/r_{pole}$ [6]. It can be seen that a smaller aperture will cause a sharper rise in the magnetic field.

As with the peak magnetic field, a mismatch between the compression magnetic field and the beam can cause rippling due to over-compression or under-compression of the beam. In general, minor scalloping will occur in the beam due to these mismatches which cannot be entirely avoided experimentally. In addition, an axis offset or tilt

between the electron gun and magnetic field can cause oscillations in the field. In general, any deviation from ideal operation leads to decreased performance of the TWT from theory. It is best to match the magnetic field in order to get an ideal flow for the electron beam, with minimal scalloping and velocity spread.

2.2.3 Collector

After the beam is formed and used in the circuit, the beam exits the magnetic field and expands so that the collector can gather the beam. Typically composed of copper, the collector's purpose is to ensure that the beam is terminated in a way that is good for the vacuum system. For high power vacuum systems, this can be a challenge. One must ensure that the beam disperses enough that is does not completely damage the copper of the collector and that outgassing in the system is kept to a minimum.

Depressed collectors can be used to create a more efficient experiment. Only a fraction of the power in the electron beam is transferred to the electromagnetic beam. To combat lost energy, the collector can be biased with a voltage, and the beam can be collected in stages. This is a way of recycling the power in the system and designing a more efficient device. Multi-stage depressed collector designs can increase experimental efficiencies by up to 65 % [17]. This consideration can be key to a practical application of a TWT. However, for the experiment considered in this thesis, a simple copper collector was used, and efficiency was not a priority in the circuit.

2.3 Analytical Theory for Slow-Wave Structures

Now that we have formed an electron beam that is confined by a magnetic field to a small beam radius over an axial length, we can discuss using that beam in a slow-wave structure (SWS). First, the interaction that happens between the beam and an electromagnetic wave will be derived. Then, certain structures which will cause the electromagnetic wave of the parameters necessary for interaction will be discussed.

The interaction structure, or circuit, is called a slow-wave structure (SWS) because

it reduces the group and longitudinal phase velocities of an electromagnetic wave in order to match the phase of the wave with the electron beam that passes through a beam tunnel in the structure. The electron beam and electromagnetic wave are traveling at a speed much less than the speed of light. By matching the velocities of the beam and wave, an interaction takes place where the wave causes velocity shifts in the electron beam. Figure 2-2 shows how part of the beam consistently sees an accelerating field and part of the beam consistently sees a decelerating field. This effect causes longitudinal bunching of the electron beam. After bunching occurs, the electromagnetic wave is able to extract energy from the beam. The extraction of energy causes the wave to be amplified and the beam to de-bunch. At this point of de-bunching, maximum amplification has occurred and saturation is reached in the device. If the interaction does not end at this point, the beam and wave will continue to exchange energy and the amplitude of the wave will oscillate. As such, the interaction should be ended before the saturation point of the structure.

The dispersion relation between the electromagnetic field and electron beam is easy to understand by considering small perturbation theory. The electric field of the $+\hat{z}$-traveling wave goes as $E \propto \exp[j(\omega t - \beta z)]$, where ω is the frequency of the wave, and β is the wavenumber. If β is imaginary, the electric field will have an exponentially growing (or decaying) real component, $\exp[\mathrm{Im}(\beta)z]$. To determine the growth of the wave, we need to establish a relationship between the ω and β by using continuity equations for the beam and electromagnetic field relationships. To do this, the electron beam and electric field will be considered separately to establish a relationship between the disturbed current and the electric field in the circuit.

First, parameters with small perturbations are introduced to understand the motion of the electron beam with the electric field. Assume that the electron beam has small disturbances in the velocity, current, and density that correspond to the electric field disturbance, such that

$$v_{tot} = v_0 + \bar{v}, \tag{2.20}$$

$$i_{tot} = -I_0 + \bar{i}, \tag{2.21}$$

$$\rho_{tot} = -\rho_0 + \bar{\rho}, \tag{2.22}$$

the initial quantities are indicated with a subscript of zero, and the small perturbations are indicated with the bar above the variable. The perturbations are all proportional to $\exp[j(\omega t - \beta z)]$, and small in comparison to initial quantities. First, the electron equation for current is introduced,

$$J_{tot} = \rho_{tot} v_{tot} \tag{2.23}$$

or, making substitutions for the perturbed equations,

$$\frac{-I_0 + \bar{i}}{A} = (-\rho_0 + \bar{\rho})(v_0 + \bar{v}) \tag{2.24}$$

where A is the cross-sectional area of the beam. This can be reduced to second order (ignoring very small terms),

$$\bar{i} = (\bar{\rho} v_0 - \rho_0 \bar{v}) A \tag{2.25}$$

Next, consider the current equation, which establishes the relationship between current and density,

$$\nabla \cdot J = -\frac{\partial \rho}{\partial t} \tag{2.26}$$

Since the perturbations are of the form $\exp[j(\omega t - \beta z)]$, the derivatives can be reduced, so that

$$\frac{-j\beta\bar{i}}{A} = -j\omega\bar{\rho} \tag{2.27}$$

Combining equations (2.25) and (2.27), establishes an equation for the perturbed velocity and current,

$$\bar{i} = \left(\frac{\beta v_0 \bar{i}}{\omega A} - \rho_0 \bar{v} \right) A \tag{2.28}$$

which can be rearranged,

$$\bar{v} = \frac{-\bar{i}}{\omega \rho_0 A} (\omega - \beta v_0) \tag{2.29}$$

Next, for the electron beam, consider that the electrons are accelerating in the electric field, which we will call E_{zT}, such that $E_{zT} = E_{zn} + E_{sc}$. In this case E_{zn} is

the electric field in the circuit, and E_{sc} is the space charge field that is due to the beam itself and its interaction with the beam tunnel in which it is propagating. The electrons accelerate as

$$\frac{dv}{dt} = \frac{-e}{m} E_{zT} \tag{2.30}$$

The velocity derivative must be split up into its partial derivatives,

$$\frac{dv}{dt} = \frac{\partial v}{\partial t} + \frac{\partial v}{\partial z}\frac{\partial z}{\partial t} \tag{2.31}$$

with $\frac{\partial z}{\partial t} = v_0$, the partial derivatives can be analyzed with the perturbed functions,

$$\bar{v}\left(j\omega - j\beta v_0\right) = \frac{e}{m}\left(E_{zn} + E_{zsc}\right) \tag{2.32}$$

The space-charge electric field is defined via Poisson's Law.

$$\nabla \cdot E_{zsc}\hat{z} = -j\beta E_{zsc} = \bar{\rho}/\varepsilon \tag{2.33}$$

which can be combined with equation (2.27)and solved for E_{zsc},

$$E_{zsc} = j\frac{\bar{i}}{\varepsilon\omega A} \tag{2.34}$$

The above equations assume an infinite beam, but since the beam is finite, a space-charge reduction factor, R, is introduced to account for the finite beam radius,

$$E_{zsc} = jR^2\frac{\bar{i}}{\varepsilon\omega A} \tag{2.35}$$

The reduction factor is, essentially, a reduction in the plasma current that the electron beam sees due to the conductive wall of the beam tunnel; a plot of the space charge reduction factor is shown in Figure 2-6. In this plot, you can see that R is dependent on the relative size between the electron beam radius, b, and beam tunnel radius, a. For simplicity, this can be re-written in terms of the reduced plasma current,

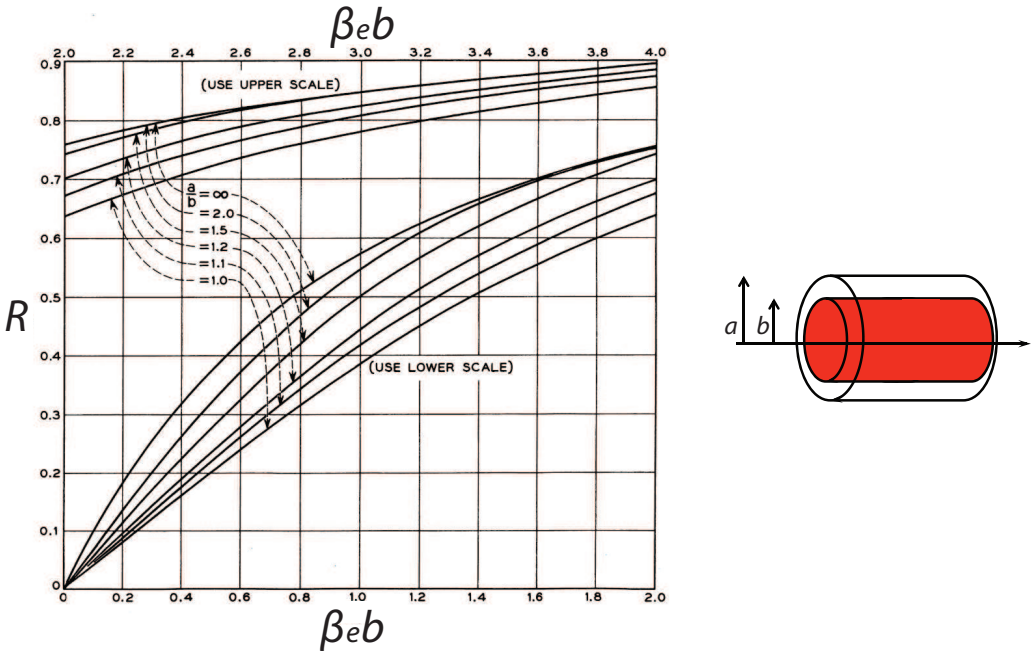

Figure 2-6: A plot of the space charge reduction factor, R vs. $\beta_e b$ for different fill-factors, a/b. To the left an illustration of an electron beam with radius b inside a beam tunnel with radius a. The case for a beam in free space is $a/b = \infty$ and for a beam that is the same diameter of the beam tunnel is $a/b = 1$ [20].

$\omega_q = R\omega_p$ such that

$$E_{sc} = j\frac{m\omega_q^2}{e\rho_0\omega A}\bar{i} \tag{2.36}$$

Finally, combining equations (2.29) (2.32) and (2.36) establishes a relationship between current and electric field.

$$\bar{i} = \frac{\omega\rho_0 eA}{mv_0^2}\frac{jE_{zn}}{(j\frac{\omega}{v_0} - j\beta)^2 + \frac{\omega_q^2}{v_0^2}} \tag{2.37}$$

This can be reduced, by considering that $\beta_e = \omega/v_0$, $I_0 = \rho_0 vA$, and $V_0 = mv^2/2e$,

$$\bar{i} = \frac{j\beta_e I_0 E_{zn}}{2V_0(\beta_e - \beta)^2 + \frac{\omega_q^2}{v_0^2}} \tag{2.38}$$

A simplified version of this equation does not consider space charge. If $E_{zsc} = 0$,

$$\bar{i} = \frac{j\beta_e I_0 E_{zn}}{2V_0(\beta_e - \beta)^2} \tag{2.39}$$

where I_0 and V_0 are the current and voltage operation conditions of the electron gun.

Now, we will consider circuit equations to explain the electromagnetic field, and find a relationship for $\bar{i}$ and E_{zn} due to the SWS. Quite simply, the impedance of the circuit is described as the coupling impedance, K, such that

$$K_n = \frac{|E_{zn}|^2}{2\beta_{cn}^2 P} \tag{2.40}$$

where P is the power in the field and $\beta_{cn} = \omega/v_{pn}$, where v_{pn} is the phase velocity of the wave, and the subscript n indicates the mode of operation (typically $n = 1$, and only β_c is indicated). Since the beam has a finite cross-sectional area, K can be averaged over the area which the beam would occupy. The electric field in the coupling impedance equation refers to the unperturbed field present in the structure without the beam. This electric field has been integrated along the beam tunnel axis, so we are dealing with the average electric field that the electron beam sees per period,

$$E_{zn} = \frac{1}{p}\int E_z(z)e^{j\beta_{cn}z}dz \tag{2.41}$$

where p is the period of the circuit. The coupling impedance is purely dependent on the geometry of the circuit, assuming ideal beam interaction within the circuit at the frequency of interest [70].

The coupling impedance is a measure of how well the electromagnetic wave can interact with the electron beam in a given circuit. A higher coupling impedance indicates a better transfer of energy between the beam and wave. Typically, TWTs have a coupling impedance anywhere between 1–50 Ω. Using the coupling impedance along with circuit equations, the electric field can be described as, [70]

$$E_{zn} = \frac{j\beta^2\beta_c K_n}{(\beta^2 - \beta_c^2)}\bar{i} \tag{2.42}$$

The two equations from the electronics and circuits methods of analysis, (2.38)

and (2.42), can be combined to arrive at the dispersion relation, without space-charge

$$1 = \frac{\beta_c \beta^2 \beta_e 2C^3}{(\beta_e - \beta)^2 \ (\beta_c^2 - \beta^2)} \tag{2.43}$$

or with space-charge,

$$1 = \frac{\beta_c \beta^2 \beta_e 2C^3}{\left[(\beta_e - \beta)^2 + \frac{\omega_q^2}{v_0^2}\right] (\beta_c^2 - \beta^2)} \tag{2.44}$$

where $\omega_q = R\omega_p$. In these equations, the pierce parameter, C, has been introduced,

$$C^3 = \frac{KI_0}{4V_0} \tag{2.45}$$

The Pierce parameter establishes an easy relationship between beam parameters, I_0 and V_0 and the circuit coupling impedance, K.

2.3.1 Gain in the Circuit

Using the dispersion relation, we can solve for the gain that occurs in the circuit. First, consider synchronous operation with the beam and wave, such that $v_p = v_0$. For now, we will ignore space charge and loss in the SWS. In this case, $\beta_c = \beta_e$. The solution for β, where $E_z \propto e^{-j\beta z}$, is of the form

$$\beta = \beta_e + \xi \tag{2.46}$$

From equation (2.43), $\xi = (-1)^{1/3}\beta_e C$. This leads to three solutions for β, corresponding to three different waves. Two slow forward waves are described with

$$\beta = \beta_e \left(1 + \frac{C}{2} \pm j\frac{\sqrt{3}}{2}C\right) \tag{2.47}$$

The imaginary component of β provides either a growing or a decaying wave. The solution which grows is the desired interaction in the TWT; this solution accounts for the gain that is seen in the circuit. There is also a fast forward wave, with $\beta = \beta_e - \beta_e C$. In addition, there is a fourth solution to the dispersion relation which

results in a fast backward wave, with $\beta = -\beta_e + \beta_e C^3/4$. The gain, G, in dB that is seen in the circuit is a result of the slow, forward growing wave,

$$G = 10 \log_{10} \left(\frac{1}{3} e^{\frac{\sqrt{3}}{2} C 2\pi N} \right)^2 \text{ [dB]} \tag{2.48}$$

where $N = 2/(\pi\beta_e)$ is the number of longitudinal wavelengths in the circuit and C is the Pierce parameter. The fractional amplitude scaling of 1/3 results from the fact that only one third of the wave couples into the slow forward growing wave. The other 2/3 is lost to the decaying slow wave and the forward fast wave. In general, the gain observed in a TWT can be written as,

$$G = -9.54 + BCN \text{ [dB]} \tag{2.49}$$

where B is dependent on the assumptions made to solve the dispersion relation. In the case of synchronous motion, with no space charge, and no loss $B = 47.3$. The initial loss due to the three separate solutions to the dispersion relation is -9.54 dB.

For non-synchronous motion, where the wave and electron beam are not traveling at the same speed, a non-synchronous parameter is introduced, b, such that

$$b = \frac{v_e - v_p}{C v_p} \tag{2.50}$$

therefore,

$$\beta_c = \beta_e (1 + Cb) \tag{2.51}$$

Equation (2.43) can be solved with β taking the form of

$$\beta = \beta_e + \beta_e C \epsilon, \tag{2.52}$$

with $\epsilon = jx - y$. Then, the exponentially growing field is of the form $E \propto \exp[\beta_e C x z]$. Assuming small b, the dispersion relation reduces to

$$\epsilon^2 (\epsilon - b) = -1 \tag{2.53}$$

where ϵ can be numerically solved and has three distinct solutions. The gain equation, (2.49), remains the same, but B is now defined as

$$B = 40\pi x \log_{10}(e) = 54.6x \tag{2.54}$$

Note that the solution for synchronous motion occurs when $x = \sqrt{3}/2$.

Next, circuit loss is added into the solution. Assuming a loss per unit length in the SWS, α, such that $E \propto \exp[-\alpha z]$ in the circuit, we can define a parameter d,

$$d = \alpha/(\beta_e C) \tag{2.55}$$

Now, β_c has a loss component and is related to β_e as

$$\beta_c = \beta_e(1 + Cb - jCd) \tag{2.56}$$

Taking β to be of the same form as equation (2.52), the dispersion relation reduces to

$$\epsilon^2(\epsilon - b + jd) = -1 \tag{2.57}$$

Once again, ϵ can be numerically solved and has three distinct solutions. The gain equation remains the same with B as defined in (2.54). However the solution for x (and calculated gain) will be less than case without loss considered.

Finally, consider the effect of space charge in the interaction. Taking the case with loss and non-synchronous motion, we can solve equation (2.44) for the conditions of equations (2.56) and (2.52).

$$\epsilon = \frac{1}{\epsilon - b + jd} + 4QC \tag{2.58}$$

where the space charge parameter, $4QC$ is defined as

$$4QC = \left(\frac{\omega_q}{C\omega}\right)^2 \tag{2.59}$$

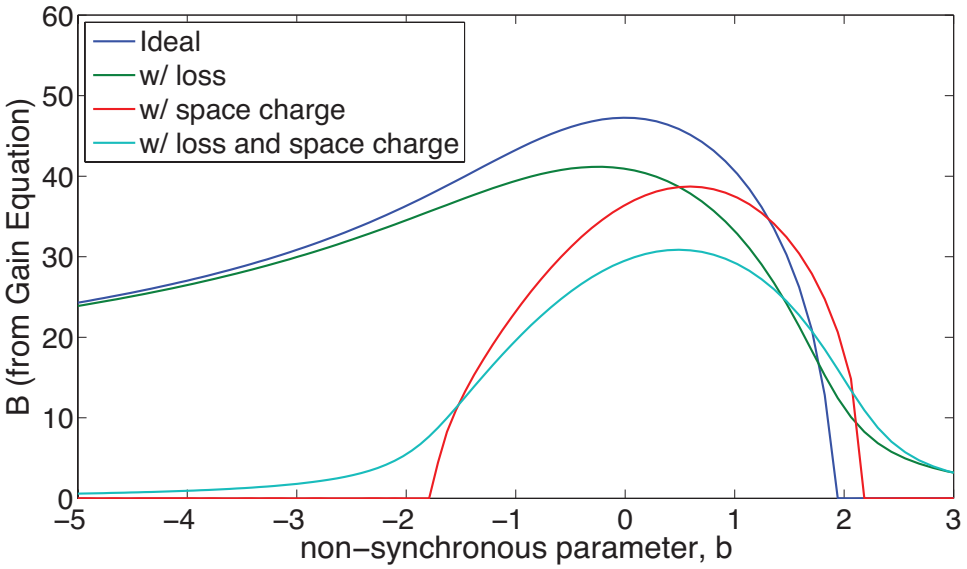

Figure 2-7: B vs. non-synchronous parameter, b, for various conditions, where $G = -9.54 + BCN$. The ideal case, with no loss or space charge, shows the highest gain. The realistic case, with the lowest gain, accounts for both loss and space-charge in the system. The parameters for this graph will be discussed in the next chapter.

These conditions establish an optimum operation parameter which is not at a synchronous motion. For ideal operation, $v_e > v_p$. Figure 2-7 shows how these parameters all affect the gain that can be seen in a circuit. Both space charge and loss reduce the gain in the device from ideal conditions. When space charge is considered, optimum operation occurs for a value of b greater than zero, where the electron beam is traveling slightly faster than the phase velocity. In addition, space charge limits the bandwidth of the device.

2.4 Types of Slow-Wave Structures

The analytical theory relies on the assumption of synchronous motion (or near-synchronous motion), meaning that the phase velocity of the wave along $\hat{z}$ must be close to the velocity of the electron beam. Since the electron beam is typically non-relativistic, it is useful to have a SWS, which causes the electromagnetic wave to travel slower than the speed of light in the axial direction.

There are several different ways to create a SWS, which is characterized as a

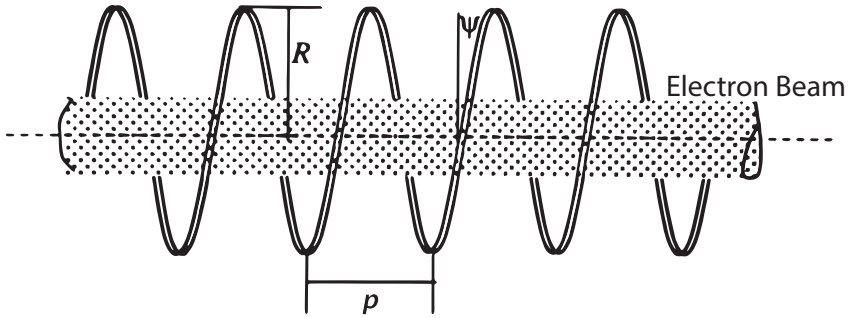

Figure 2-8: A diagram of a helical TWT slow-wave structure with the electron beam traveling through the middle of the helix. Figure from [70].

structure where the group and phase velocities of the wave are less than the speed of light. In this section we will discuss, in detail, helical TWTs and coupled-cavity TWTs.

2.4.1 Helical TWTs

A helical SWS was the design of the first invented TWT. A diagram of a helical structure with an electron beam is shown in Figure 2-8. In this device, the electromagnetic wave travels along the wire conductor that has been wrapped into a helix. The wave travels at the speed of light along the wire. However, in the frame of the electron beam, the wave travels much slower than c along the $\hat{z}$-axis. The field travels along the helix, with a certain pitch factor, ψ, which slows down the wave such that

$$v_p = c \sin \psi \tag{2.60}$$

where the pitch factor can be described in terms of the length between helical rotations, or period, p, and the radius of the helix, R,

$$\tan \psi = \frac{p}{2\pi R} \tag{2.61}$$

The phase velocity calculation, (2.60), indicates that the phase velocity does not depend on frequency. Though some generalities have been taken into account, there

is still very little dependence on frequency in the phase velocity, therefore helical TWTs are able to support very wide bandwidths; up to 3 dB bandwidths (50 %) are common in low frequency TWTs. However, the field near the center of the electron beam is small, and the coupling factor from a helical TWT is typically low (about 1 Ω).

The frequency dependence of the helix shows up when you consider the number of wavelengths per period, N_p.

$$N_p = \frac{\lambda}{2\pi R} \tag{2.62}$$

This parameter establishes a relationship between wavelength, λ, and the radius of the helix, R. Consider a helical structure of radius R at various frequencies. For high frequencies, N_p is small. In the extreme case ($N_p < 1$) the electric fields remain very close to the helical wire; this will severely decrease the interaction that can take place ($K \ll 1\Omega$), and the structure will not function as intended. At extremely low frequencies, N_p is large. As N_p increases, the electric field will be farther away from the wire and the interaction will decrease due to wave interference with itself [70]. The ideal situation is about $N_p = 4$. In this case, N_p is appropriately sized such that the electric field is contained near the wires where magnetic flux exactly cancels between the turns of the wire which enhances the field at the location of the electron beam.

The trouble with helical TWTs is that, as the frequency of the device increases, the size of the helix becomes incredibly small. Considering this relationship between N_p and TWT performance for a helical TWT at high frequencies, a very small radius needs to be constructed for ideal performance. For example, a 94 GHz TWT with $N_p = 4$ must have a radius of $R = 127$ μm, which is incredibly small. Outside of construction considerations, this radius leads to a very small beam-tunnel which could not support a large current. Even to get a small amount of current through the beam tunnel would require a large current density and a strong magnetic field must be used. In addition, the delicate nature of small structures leads to the inability for high frequency helical TWTs to support high average powers. As such, it is necessary

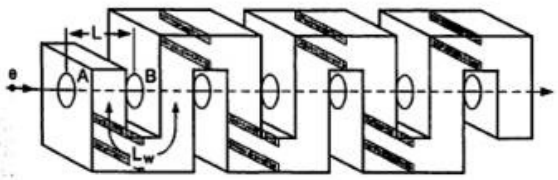

Figure 2-9: A folded waveguide coupled-cavity design. (Picture from [37].)

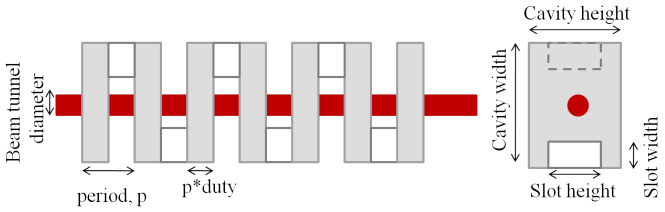

Figure 2-10: A rectangular folded-waveguide coupled-cavity TWT with staggered coupling slots.

to explore other types of TWTs for the W-band if we would like to find high power devices.

2.4.2 Coupled-Cavity TWTs

A generic folded waveguide TWT is shown in Figure 2-9. The waveguide has been folded to a certain period length to create a SWS and allow for an electron beam to travel through the waveguide and interact with an RF wave. The phase velocity of the wave along the electron beam tunnel, v_p, is nearly equivalent to the velocity of the electron beam, v_e, allowing a transfer of energy from the beam to the wave. A staggered coupled-cavity TWT is formed when the upper and lower portions of this waveguide are made into coupling slots instead of loaded waveguides, as shown in Figure 2-10, with useful parameters labeled. The staggered slots allow for a specific phase advance per cavity for a forward wave interaction [37]. The cavity can be any shape that resonates with the operation frequency; often circular or rectangular cavities are used.

For a coupled cavity TWT, a generic dispersion relation is shown in Figure 2-11(a). As seen, the dispersion follows a near-sinusoidal relationship between phase advance and frequency. Assuming interaction near the center of the cold circuit bandwidth,

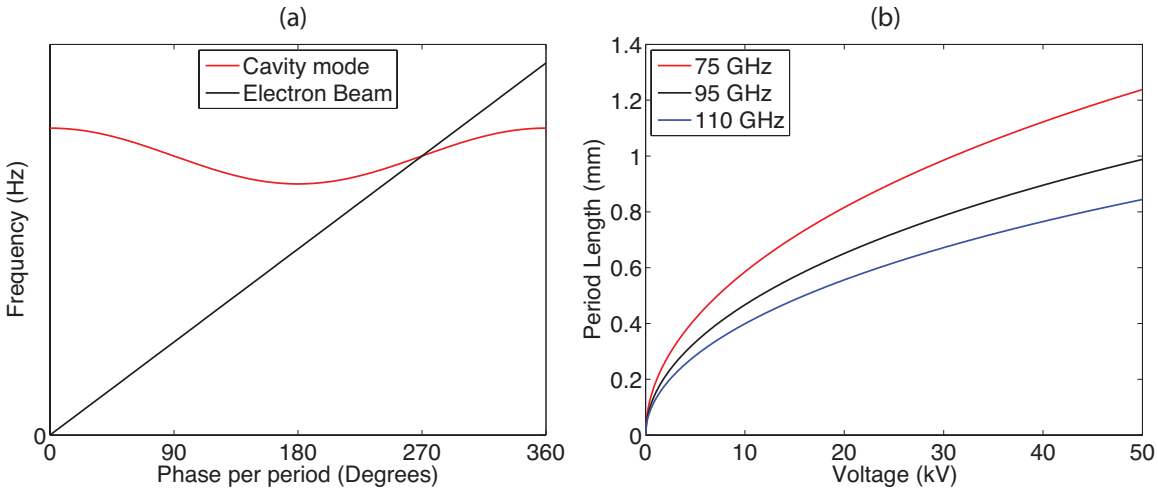

Figure 2-11: (a) A generic dispersion relation for a coupled-cavity TWT shown along an intercepting electron beam-line. (b) The period requirement for certain operation voltages along various operation frequencies in the W-band as calculated with equation (2.63).

the period length, p, for forward wave interaction is calculated as

$$p = (3/4)v_e/f \tag{2.63}$$

assuming that operation is wanted near the center of the bandwidth. Figure 2-11(b) shows the relationship between operation voltage and period of a SWS. One can see that operation points with a larger voltage are desirable due to the larger period size; this would make a structure at high frequency easier to fabricate. However, there are negative consequences of operating at high voltage. First, in experimental implementation higher voltages are harder to implement. Second, the voltage plays an effect in the gain of the TWT, recall that the gain is proportional to the Pierce parameter, C, which is, in turn, proportional to $1/V_0^{1/3}$. Therefore, a balance must be struck between these trade-offs to determine operation voltage.

In general, many of the parameters for the coupled-cavity TWT are determined by the desired operation of the device. In general, the frequency of operation determines the size of the cavities. The period between the cavities sets the operation voltage. The beam tunnel size must be below cut-off for the operation wavelength, and must be chosen such that it allows minimal coupling between the cavities; this allows for

a larger bandwidth of operation. In design, the size of the coupling slots between the cavity will determine both the coupling impedance and the operation bandwidth. These parameters will be discussed in detail in the next chapter. In general, the bandwidth of a coupled-cavity TWT will be much smaller than the helical TWT, but it will have a much larger coupling impedance (on the order of 10 Ω). The robust nature of the cavities also allows for larger power loading.

Chapter 3

Design of a 94 GHz Overmoded Coupled-Cavity TWT

Having established the theory of a TWT, the specific design of an overmoded coupled-cavity TWT will be discussed along with the advantages that can be achieved with an overmoded device. The design specifics for the 94 GHz overmoded TWT will be presented along with simulations of the experiment.

3.1 Problem Statement

The goal of this thesis is to design and build a W-band TWT with a center-frequency of 94 GHz that demonstrates more than 30 dB of gain and a high saturated output power, greater than 100 W. In order to meet these design constraints, achieving a large bandwidth or high efficiency in the device is not a primary concern. However, the tunable bandwidth should be greater than 1 GHz, and the instantaneous bandwidth should be more than 100 MHz. An overmoded TWT is an ideal design to meet these specifications since it will allow for a large amount of beam power to be coupled into the device.

The design will have an overmoded cavity with a large beam tunnel. This will be used to operate at a low magnetic field, which will support an electron beam with a low current density. The design will be limited by a 2.5 kG solenoid magnet that

was available for the experiment which limited the current available for the design. Alternatively, a large magnetic field could have been used to increase the current available in the system.

The experiment will also be pulsed operation, not continuous wave (CW). As such, heating considerations have not been taken into account in the design. Water cooling channels could be added to the design to scale the operation to longer pulse widths, but that is outside of the scope of this thesis and would complicate the initial proof-of-concept for the overmoded TWT design. The lab is equipped with a 2.8 microsecond pulse generator that can provide a well-shaped voltage pulse between 10–100 kV.

The specifics of the magnet and pulse modulator will be discussed in the next chapter, but the parameters are worth noting since they add engineering constraints to the cavity design and must be considered for TWT simulations.

3.2 Electromagnetic Cavity Design

The coupled-cavity structure allows for many elements to be changed to alter the electromagnetic fields in the TWT. For example, ridges can be placed along the beam tunnel in the cavity to increase the coupling impedance of the TWT without reducing the bandwidth of the structure. These ridges cause an increase in the electric field along the axis of the TWT [28]. Unfortunately, the ridges are rather small, difficult to manufacture, and subject to damage at high powers. Another possibility for change in the structure is the shape of the TWT cavity. Oftentimes, cylindrical cavities are used instead of the rectangular cavities depicted in Figure 2-9 to take advantage of matching the shape of the electromagnetic fields to the beam tunnel. In addition, there are many possibilities for placing the coupling slots between the cavities and in manipulating the phase advance seen between the cavities. Many other cavity designs are possible, but are typically unrealistic to build. Since this thesis will have an experimental validation of design, an emphasis was put on the practicality of manufacturing the cavities. In this thesis, a coupled-cavity TWT has been designed

which takes advantage of the robust nature offered by operating in a higher order mode of the rectangular cavity for the frequency of interest; this operation mode is what designates the device as an overmoded TWT.

3.2.1 Cavity Fields

To begin, consider the resonant electromagnetic field of a rectangular cavity. A coupled-cavity TWT has a certain electromagnetic mode of operation, as determined via Maxwell's equations. In the case of a TWT cavity, the electric field should be directed along the axial direction of the TWT, $\hat{z}$, in order to couple to the electron beam passing through the cavity. If we solve Maxwell's equations for a rectangular cavity, we are primarily interested in the Transverse Magnetic (TM) modes of the cavity where the electric field has a $\hat{z}$-directed component. For a rectangular cavity, with sides a, b, and d, we can solve for the TM electric and magnetic fields in a cavity,

$$E_x = \frac{j\eta k_x k_z}{k_0^2} H_0 \cos k_x x \sin k_y y \sin k_z z \tag{3.1}$$

$$E_y = \frac{j\eta k_y k_z}{k_0^2} H_0 \sin k_x x \cos k_y y \sin k_z z \tag{3.2}$$

$$E_z = \frac{j\eta (k_x^2 + k_y^2)}{k_0^2} H_0 \sin k_x x \sin k_y y \cos k_z z \tag{3.3}$$

$$H_x = \frac{k_y}{k_0} H_0 \sin k_x x \cos k_y y \cos k_z z \tag{3.4}$$

$$H_y = -\frac{k_x}{k_0} H_0 \cos k_x x \sin k_y y \cos k_z z \tag{3.5}$$

$$H_z = 0 \tag{3.6}$$

where H_0 is the normalized amplitude of magnetic field, η is the impedance of vacuum, and the wavenumber is calculated in the cavity as,

$$k^2 = k_x^2 + k_y^2 + k_z^2 \tag{3.7}$$

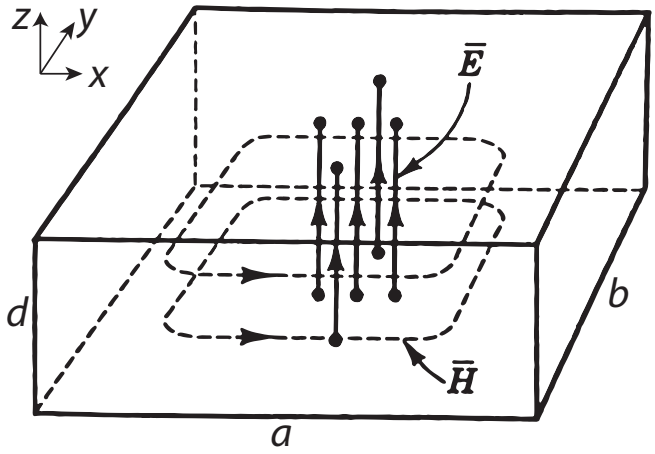

Figure 3-1: An illustration of the electric and magnetic fields in the TM_{110} cavity mode. (Figure modified from [12].)

where

$$k_x = m\pi/a \tag{3.8}$$

$$k_y = n\pi/b \tag{3.9}$$

$$k_z = s\pi/d \tag{3.10}$$

where m, n, and s are integers. The cases that lead to the best interaction with the electron beam require that the electric field exist only in the $\hat{z}$-direction, or $E_x = E_y = 0$. This condition is easily satisfied for the TM_{mn0} modes where

$$k_z = 0. \tag{3.11}$$

Figure 3-1 displays the fundamental cavity mode, TM_{110}, where $\bar{E} = E_z\hat{z}$.

The cavity frequency for the TM_{mns} mode is determined via the wave equation, where

$$\omega^2\mu\varepsilon = k^2 \tag{3.12}$$

with $\omega = 2\pi f$, and can be solved such that

$$f_{mns} = \frac{1}{2\sqrt{\mu\varepsilon}}\sqrt{\left(\frac{m}{a}\right)^2 + \left(\frac{n}{b}\right)^2 + \left(\frac{s}{d}\right)^2} \tag{3.13}$$

This is the resonant frequency for a perfect rectangular cavity. In reality, the fields and frequency of the cavity are affected by both the beam tunnel and the coupling slots in the circuit, which will shift the frequency higher or lower, depending on where they are placed in the circuit.

In general, a cavity has a strict operation frequency with a very small bandwidth, since the bandwidth is proportional to the resonant Q of the cavity [40]. However, by adding coupling slots in the cavity, the Q decreases and the bandwidth becomes larger than just the single operation point. In this way, the size of the coupling slots determines the bandwidth of the TWT as well as having the ability to enhance or decrease the resonance of the cavity and, therefore, the coupling impedance of the TWT.

Typically, the cavity of a TWT is chosen such that the operation mode is the fundamental cavity mode, TM_{110}. By choosing a fundamental mode, a majority of the electric field's power is in the center of the cavity and able to interact well with the electron beam passing through. However, the size of the TWT is predetermined due to the nature of the modes in the waveguide. For a 94 GHz TWT, the sides of a square cavity, a and b, would be 2.26 mm (slightly less than 0.1 inch). This is small enough to cause manufacturing difficulties when using standard machining tools and materials for vacuum, especially when tight manufacturing tolerances are taken into account. In addition, the size of the coupling slots and beam tunnel must be smaller than the cavity size, which causes an even larger burden on manufacturing. A small beam tunnel also leads to either small currents or large magnetic fields for confinement. The fundamental mode may be the obvious choice for operation, but it is not the only possibility.

3.2.2 The TM_{31} Mode

An overmoded coupled cavity TWT operates in a higher order mode of the cavity. By choosing to operate in a higher order mode, the size of the cavities increases for the same frequency of operation. Figure 3-2 shows the first four modes of a cavity of the form TM_{mn0} which has been tuned for operation at 94 GHz. In this case,

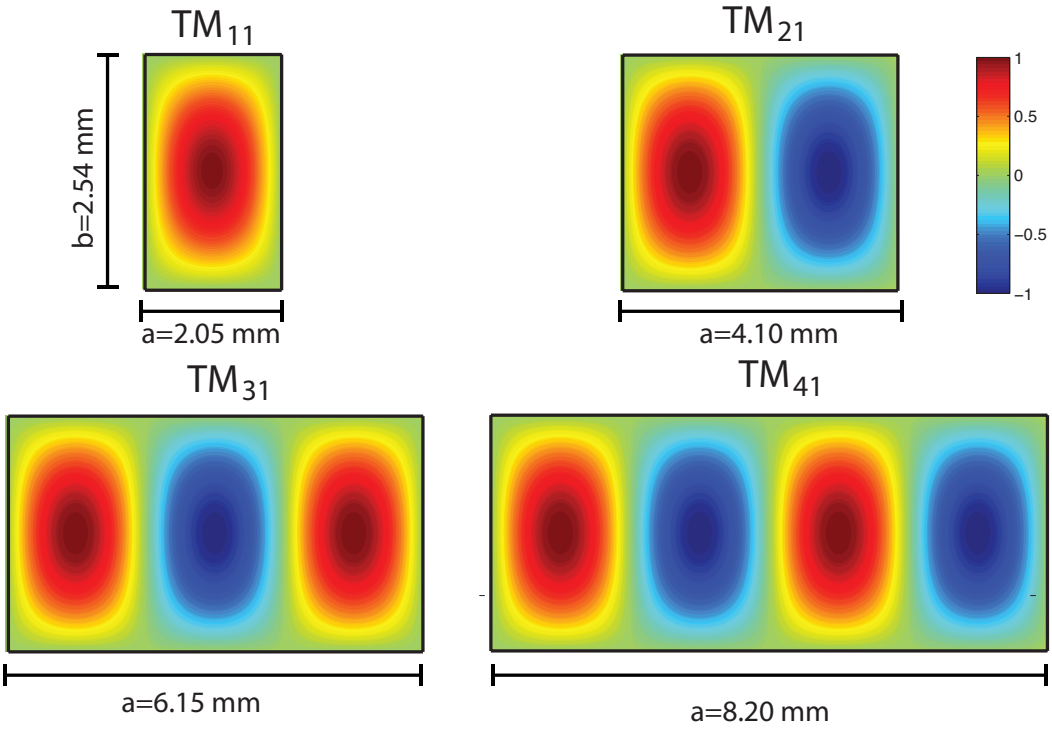

Figure 3-2: Contour plots of the electric field, $E = E_z$, for some of the lowest order cavity modes. For each mode, b has been set to 2.54 mm, and a is determined such that the mode will oscillate at 94 GHz.

b has been taken to be consistent among the cavities, and a has been changed to select the frequency of operation. A larger cavity has several advantages: easier to manufacture, a larger beam tunnel, and lower heat loads are just a few. These points can lead to many more advantages in the design of the TWT, as well. For example, a larger beam tunnel allows for an increase in the operation current, or it can lead to a lower current density and operation with a lower magnetic field. The design of the overmoded TWT will be determined in detail in the next section. Of the cavities depicted in Figure 3-2, only the fundamental mode and the TM_{310} (or TM_{31} mode, for simple designation) have a peak electric field at the center of the cavity. For simplicity in design, the TM_{31} mode was chosen as the high order mode of operation for this design in order to keep the electron beam at the center of the cavity.

Without considering coupling slots or the beam tunnel, a rectangular cavity which operates at 94 GHz in the TM_{31} mode is simple to design. The frequency of the TM_{31}

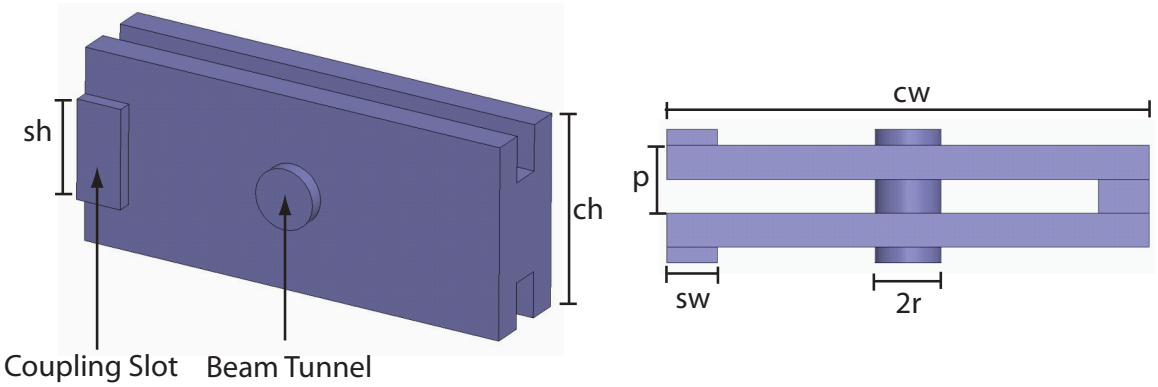

Figure 3-3: Two cavities of the TWT structure linked via staggered coupling slots, as seen with an isometric view and from the top of the structure. The purple areas show the negative vacuum space, which is surrounded by copper metal to make the cavity. The dimensions for the slot width, sw, slot height, sh, cavity width, cw, and cavity height, ch are indicated.

mode is

$$f_{310} = \frac{1}{2\sqrt{\mu\varepsilon}}\sqrt{\left(\frac{3}{a}\right)^2 + \left(\frac{1}{b}\right)^2} \tag{3.14}$$

Since there is no electromagnetic field variation in the $\hat{z}$-direction, d, is independent of the frequency of operation. Since d is in the same direction as the electron beam, the simple relationship was chosen,

$$d = p/2 \tag{3.15}$$

to allow for uniform beam bunching. The period length, p, is set by the desired voltage of operation. Therefore, only two free variables are left to adjust to set the frequency of the mode, a and b.

For simplicity that will be apparent when designing input and output couplers, one of the sides of the cavity should be the same height as standard WR-10 waveguide. WR-10 waveguide is the standard rectangular W-band waveguide, which is 0.10 x 0.05 inches in size (2.54 x 1.27 mm). Therefore, $b = 2.54$ mm, and equation (3.14) can be solved such that $a = 6.15$ mm. These dimensions are solved for various modes in Figure 3-2.

In reality, coupling slots and a beam tunnel must be added to the design, as

shown in Figure 3-3. The variables a, b, and d have been changed to ch, cw, and $p/2$, respectively, since the cavity equations are no longer completely valid. The full structure will be a series of these cavities repeated over a certain length. The addition of the coupling slots and beam tunnel will change the frequency of operation for the cavity slightly. In addition, these features will change the Q and the bandwidth of the cavity.

3.2.3 Other Modes and Dielectric Loading

In any given cavity, it is important to note that an infinite number of higher order modes exist at different frequencies. When building a TWT, there is a possibility of oscillations happening in the mode of interest as well as in any of the other modes in the waveguide. These oscillations would disrupt the operation of the TWT and prevent high powers from being reached. For operation in the fundamental mode of a cavity, oscillations in other modes are generally not a problem since all other modes will exist at higher frequencies and have higher start currents for oscillation than the fundamental mode. For the overmoded cavity, other modes must be considered, particularly lower order modes with low start currents for oscillations.

The three lowest order modes are shown in the dimensions for the 94 GHz TM_{31} mode cavity in Figure 3-4. These modes were calculated in ANSYS HFSS, a high frequency 3-D finite element electromagnetic field solver. Unless otherwise noted, all field solutions in this thesis were obtained with HFSS. The fundamental mode of this cavity is at about 67 GHz and is a large threat to operation. Since it is the fundamental mode, it has a low start current for oscillations, high electric field on axis, and a large predilection for the electron beam to interact with the mode. The other mode shown, TM_{21}, is of only minor interest. Under the right operating conditions, there is a possibility for oscillations, but there is no peak electric field in the center of the cavity (where the electron beam is located). Therefore, an offset in the beam tunnel would be needed to excite the mode, and it would be a small interaction even under that condition.

With the addition of coupling slots and a beam tunnel, the bandwidth of the modes

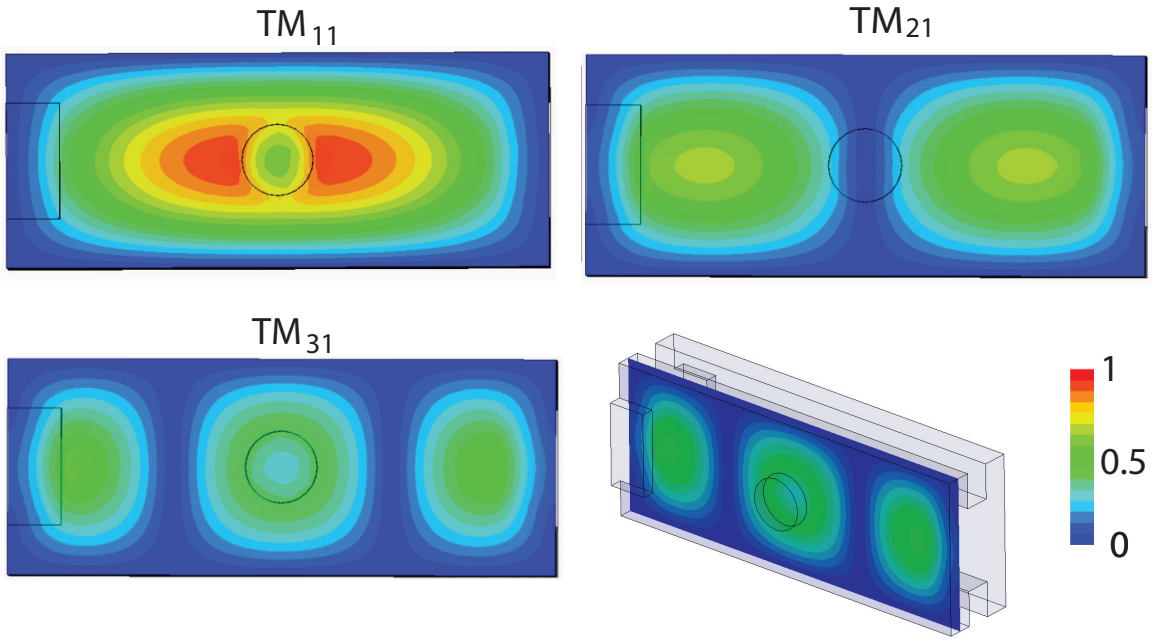

Figure 3-4: The electric field patterns of the three lowest order TM modes in a rectangular cavity tuned to 94 GHz for the TM_{31} mode.

is increased. These features are outlined in Figure 3-4. The dispersion relation for the three lowest order modes is shown in Figure 3-5, where the frequency dependence of each mode is shown as a function of the phase advance per cavity. This plot also shows the electron beam line, defined as $\omega = k_z v_e$, which has been tuned for operation with the 94 GHz mode. In the locations where the electron beam crosses with a dispersion relation, the phase velocities of the two are matched and they are in synchronous motion. This intersection means that there can be a strong coupling interaction between the beam and the mode. The interaction which occurs with the fundamental mode could, potentially, cause an oscillation at about 67 GHz.

In order to eliminate the threat of the fundamental mode from interacting with the electron beam, additional losses should be added to reduce the start current for the TM_{11} mode. If the walls of the cavity were made out of a lossy material, all of the modes in the waveguide would see a high loss in the circuit. For example, if the walls of the cavities were made of a dielectric material instead of copper, there would be a significant amount of loss in the system. Ignoring the fact that this would be an impractical cavity design, the lossy dielectric would reduce the potential for

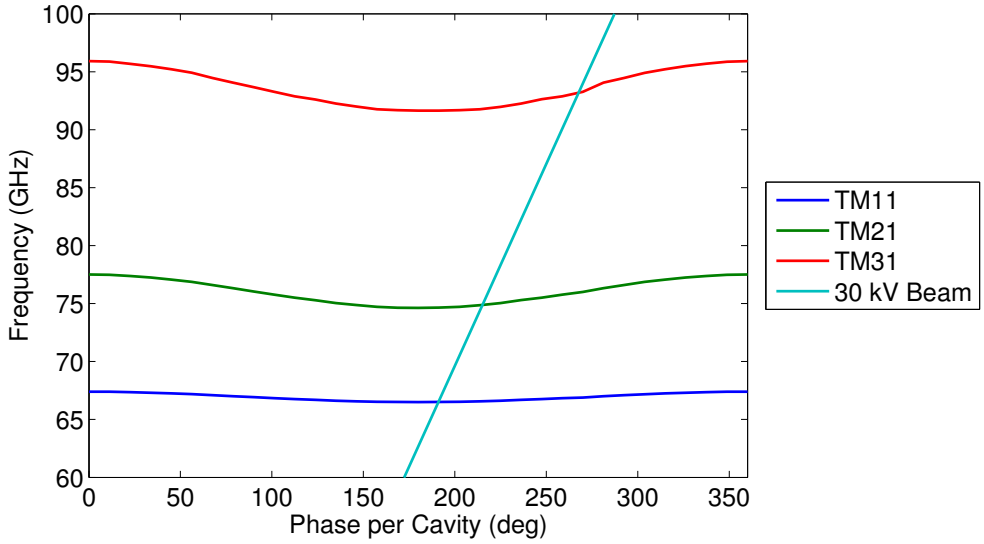

Figure 3-5: The dispersion relation for the lowest order TM modes of the cavity along with an electron beam line optimized for interaction with the TM_{31} mode.

oscillation of all of the modes in the system - including the TM_{31} mode.

However, it is possible to selectively damp the TM_{11} mode while maintaining the TM_{31} mode with minimal losses. A way to achieve this is by selectively adding dielectric to the walls of the cavities in very particular locations. If we were to add dielectric in places where the TM_{11} mode has high field and the TM_{31} mode has low fields, this effect can be achieved. Figure 3-6 shows the placement of dielectric loading on the top and bottom of the cavity. The cavity is machined out of copper (with the vacuum of the cavity, coupling slots, and beam tunnel shown in purple), and the dielectric (pink) is placed on top of the cavity, inset into the surrounding copper. Figure 3-7 shows how the dielectric placement corresponds to low-field regions of the TM_{31} mode, as calculated in HFSS. In the region that the dielectric is placed, the TM_{31} mode also has low surface currents, leading to minimal interaction with the wall at that location. However, the electric field of the TM_{11} and TM_{21} modes is seen leaking into the dielectric loading, and these modes have high interaction at the wall where the dielectric is located. Figure 3-8 shows the S_{21}, or transmission, through a single cavity with dielectric loading. The pass-bands of the lowest frequency cavities are seen in the graph. It is noticeable that the fundamental mode and the TM_{21} mode

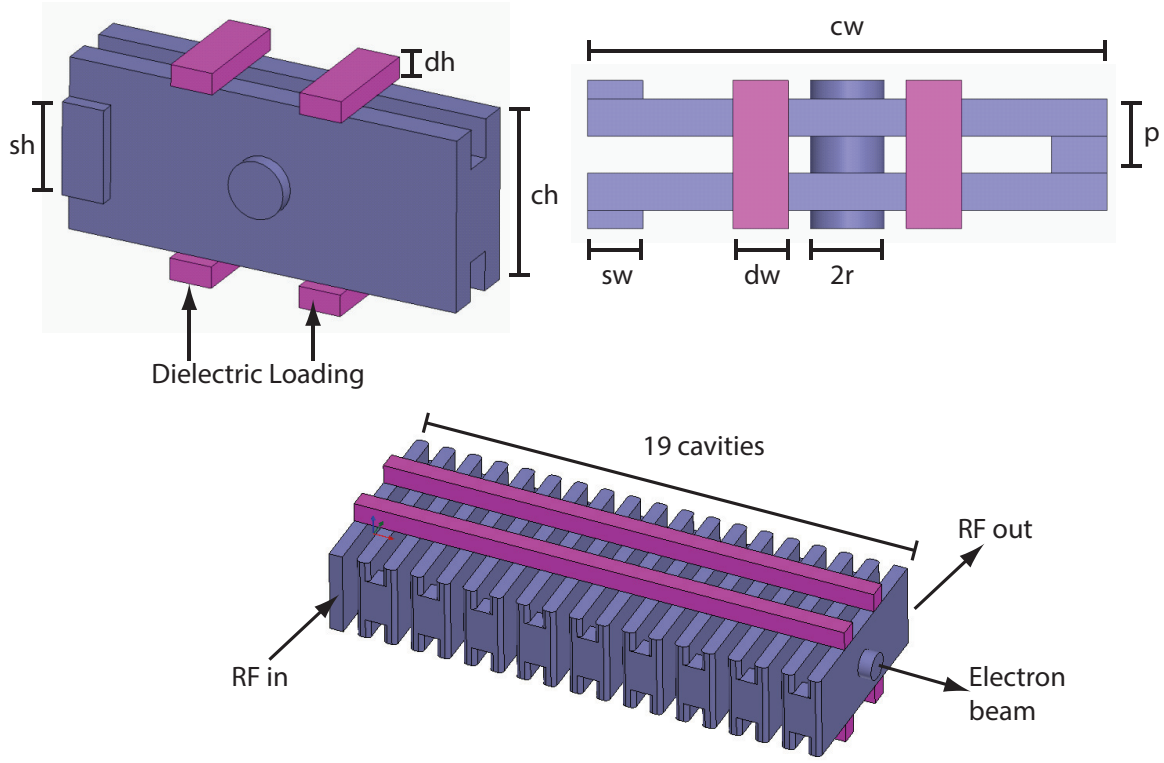

Figure 3-6: Placement of dielectric on the top and bottom of the cavity. Purple is the negative vacuum space, pink is dielectric, and the vacuum space is surrounded by copper. Two cavities are illustrated which are repeated indefinitely for an infinitely long TWT with a specific phase advance specified between the two-cavity sections. A sample circuit with 19 total cavities is shown with RF input and output marked on the first and last cavities, respectively.

see high losses due to the dielectric loading, while the TM_{31} mode has a minimal loss due to the dielectric loading. In fact, the small loss that the TM_{31} mode sees is useful for TWT operation. Over the entire length of the circuit (10–100 cavities), the TM_{11} mode will see significant losses and will not be a threat to oscillations. The TM_{31} mode will have slightly more loss than in the pure copper structure, but the relatively high-loss circuit eliminates the possibility of round-trip oscillations in the TM_{31} mode due to reflections from the output, as will be shown in simulation. In the final design, a sever is not needed due to these losses, as will be discussed later.

The material used for the lossy dielectric loading must have several key properties. First, and foremost, it must be safe to use in vacuum, otherwise it cannot be used in the TWT. Secondly, in order for the dielectric to perform as we have described,

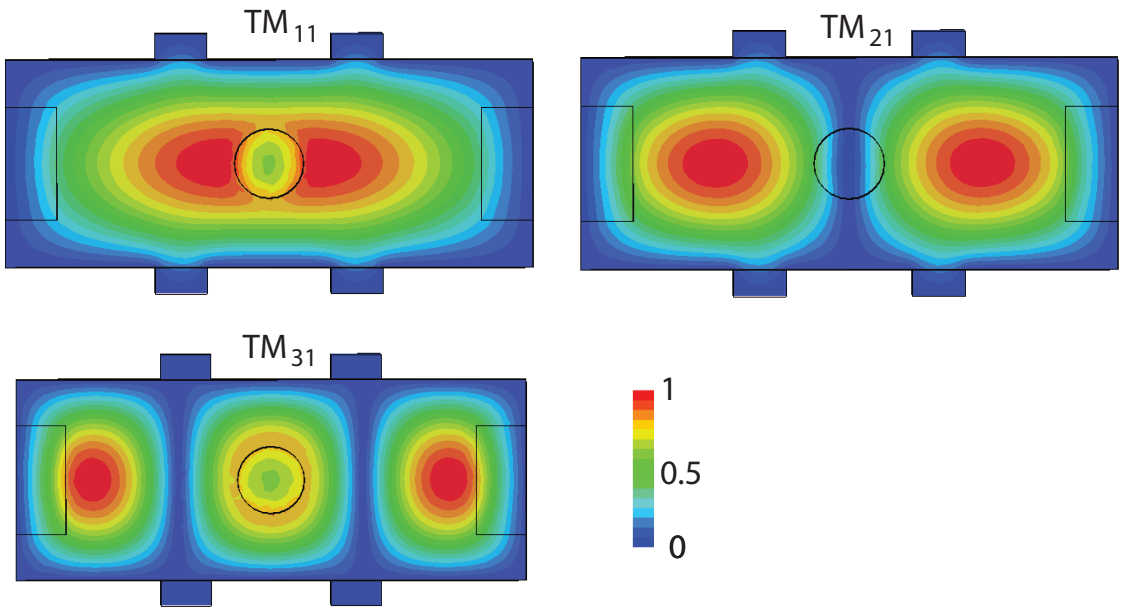

Figure 3-7: The electric field patterns of the three lowest order TM modes in a rectangular cavity tuned to 94 GHz for the TM_{31} mode with dielectric loading added.

it must have a large loss tangent at high frequencies. Many dielectrics will not provide sufficient losses for frequencies above 10 GHz, and this material must suppress oscillations at 67 GHz and above. In addition, it would be ideal to have a dielectric with good thermal properties so that it will be able to deal with the possible stresses of the TWT. Several possible dielectrics fit these categories, but aluminum nitride composites are particularly good at providing high relative permittivities and large loss tangents at high frequencies. The aluminum nitride (AlN) composite from Sienna Technologies that will be used in experiment has a loss tangent of $\tan\delta = 0.26$ and a relative permittivity of $\varepsilon_r = 34$ at 12 GHz [60]. Previously, this material was used to show the suppression of 10 GHz modes in a proof-of-concept TM_{31} coupled-cavity design on which this work is based [10] These values were used in HFSS simulations, though they may be lower at higher frequencies. Cold tests, as reported in Chapter 4, show that the AlN composite properties are sufficient for the overmoded TWT performance.

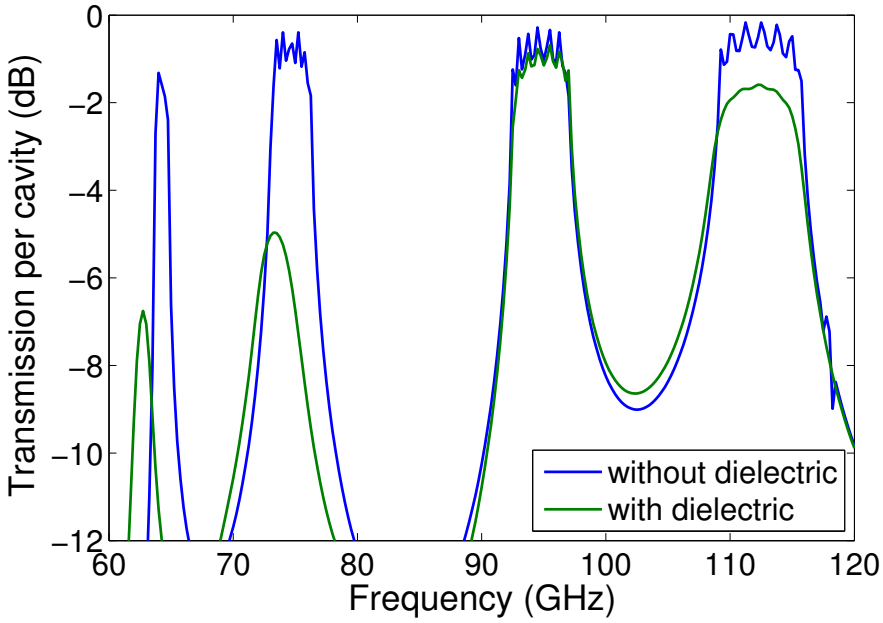

Figure 3-8: The transmission through a single cavity with and without dielectric loading for the lowest four TM modes. The dielectric used in simulation had a high loss tangent, $\tan\delta = 0.25$, and ε_r =24 for all frequencies.

3.2.4 Final Design Parameters

The goal of the TWT design is to create a cavity structure, with coupling slots and a beam tunnel that will allow for high gain and high peak power. In order to achieve this, a large Pierce parameter is wanted in the circuit since the gain is proportional to C. To reiterate, the Pierce parameter is defined as,

$$C^3 = \frac{KI_0}{4V_0} \tag{3.16}$$

In essence, this amounts to two parameters that can be manipulated in the circuit: the coupling impedance, K, and the ratio of current to voltage, I_0/V_0.

A large coupling impedance primarily results from having a peak electric field region on-axis and with alignment to the beam tunnel. As a reminder, K is a result of the integral of the magnitude of electric field along the beam tunnel. In addition to the peak field on-axis, the design of the coupling slots should ensure that the wave does not couple to the next circuit via the beam tunnel; this behavior would

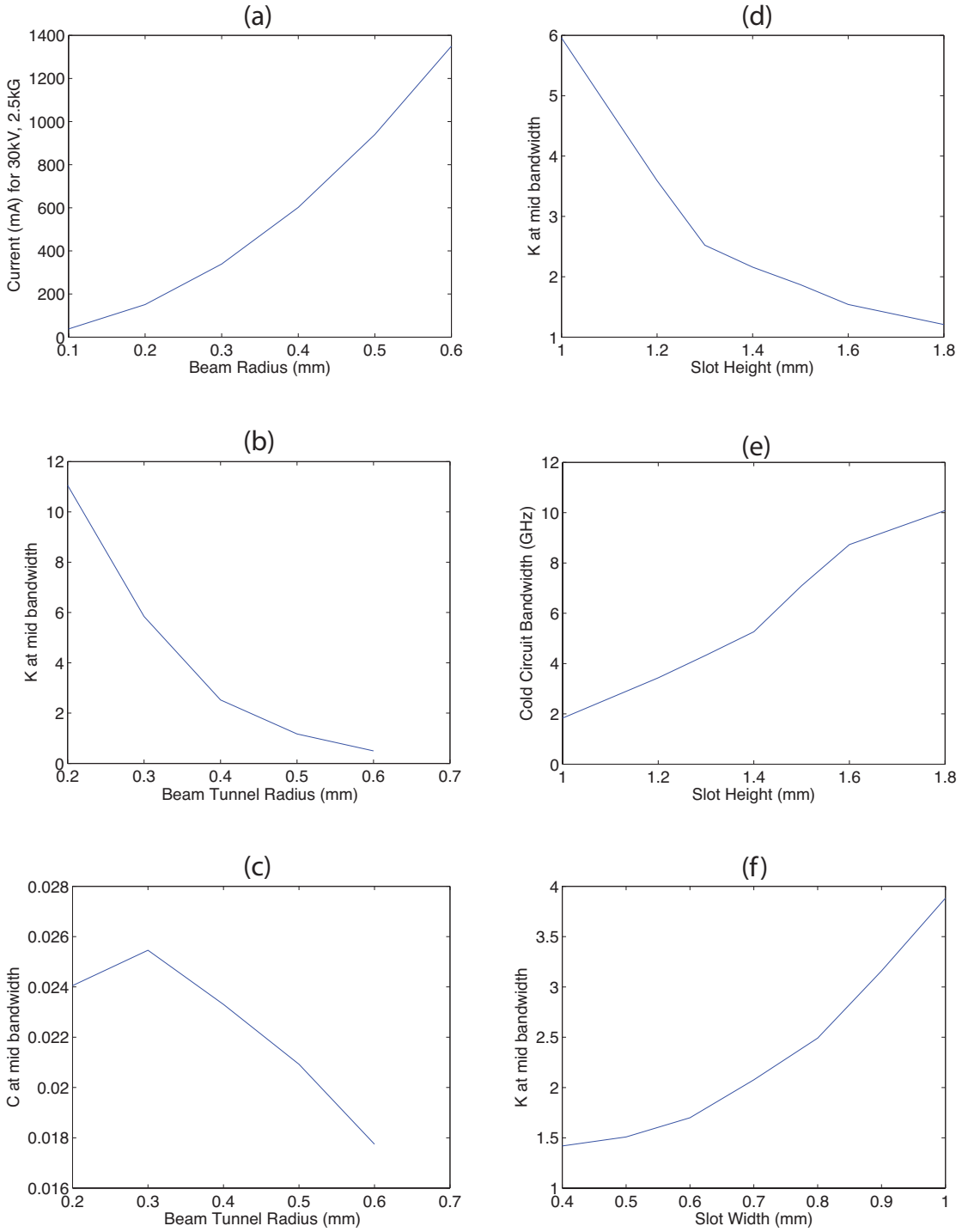

Figure 3-9: The variation of the (a) current, (b) K and (c) C, as dependent on the beam tunnel radius with constant coupling slot parameters and assuming a 2.5 kG limiting field. Alongside the variation of (d) K and (e) cold-circuit bandwidth vs. slot height and (f) K vs. slot width (Graphs taken with all other parameters kept constant.)

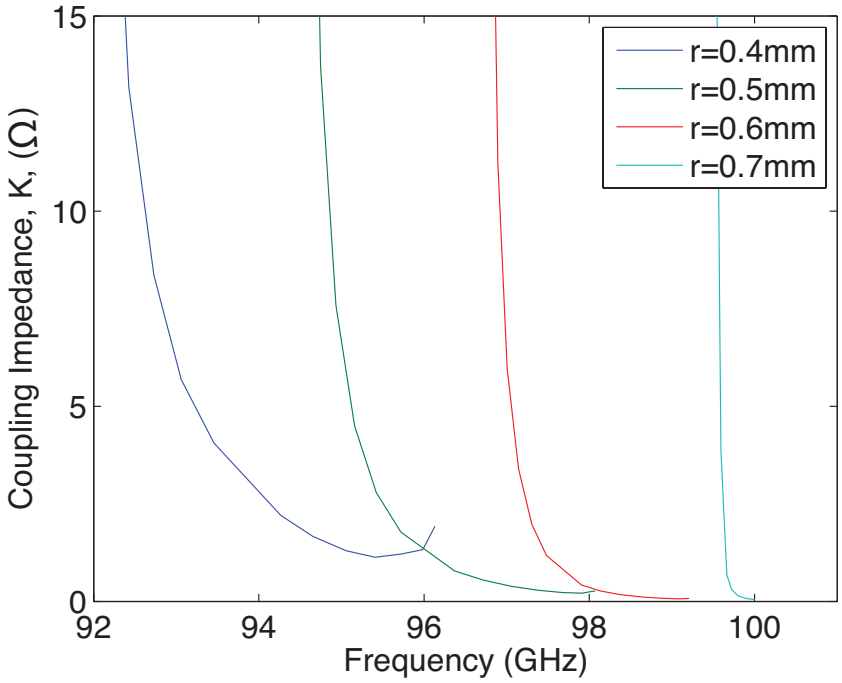

Figure 3-10: The effect of beam tunnel size on calculated coupling impedance through the middle of the circuit. For each simulation in HFSS, all other parameters were kept consistent.

reduce the coupling impedance since the oscillations between the cavities would be less pronounced.

Therefore, the relative size between the coupling slots and beam tunnel greatly affects the coupling impedance observed in the circuit. The relationships between these circuit dimensions, the coupling impedance, and Pierce parameter are shown in Figure 3-9. In essence, it is wanted for both the coupling slots and beam tunnel to be of sizes that are below cut-off for the 94 GHz mode (this equates roughly to having dimensions less than 1.5 mm). To couple through the slots and not the beam tunnel, the slots should always be kept slightly larger than the beam tunnel; this parameter ensures a larger coupling impedance. Figure 3-10 shows how the coupling impedance is inversely proportional to the beam tunnel radius. However, more current

can be pushed through the circuit with a larger beam tunnel. As it is, this allows for an optimum beam tunnel and slot dimensions to be found. Figure 3-9(c) shows a peak in the Pierce parameter at about 0.3 mm radius, though this data was taken while keeping the coupling slots at a consistent size. With further optimizing of the circuit, the beam tunnel became slightly larger allowing for more current in the system without severely limiting the coupling impedance.

Bandwidth is also of consideration when optimizing the circuit. Figure 3-9(e) makes it clear that larger coupling slots increase the cold-circuit bandwidth of the device. The cold-circuit bandwidth is equivalent to the bandwidth of the pass-band for the TM_{31} mode as seen in the dispersion relation for the mode. It is distinct from the hot-circuit instantaneous bandwidth, which can be significantly smaller since it is bound to a single voltage operation condition. Unfortunately, larger bandwidths typically lead to a decrease in the coupling impedance for the mode. This observation corresponds with the extreme case of a folded waveguide TWT - which has a wide bandwidth but very little coupling impedance (less than 1 Ω). Though, this relation is not true when considering the effect of beam tunnel size, as seen in Figure 3-10; one must keep in mind that a smaller beam tunnel radius cannot support the same quantity of current in the circuit. For the coupled-cavity design in this thesis, bandwidth was not made a priority, and the coupling dimensions were optimized such that we would have at least 30 dB of gain in the circuit; this ended up limiting the cold-circuit bandwidth to about 5 GHz (Details will be shown later in this chapter.)

The limitations on the current in the design are also a large factor in the gain that the TWT will see and play a large part in the design of the circuit. One of the goals of using an overmoded circuit to allow for a larger beam tunnel in the design. We see with the limitation due to the coupling slots, that the beam tunnel can be large for the TM_{31} circuit design, but it is useful to know the amount of current that can be supported in the design for particular beam radii. In that limitation, the magnetic field also sets certain limitations in the design that are important to discuss. Due to the Brillouin limitation (described in Chapter 2), only a certain current can be supported in the TWT at a particular voltage. Figure 3-11 shows the limit for the

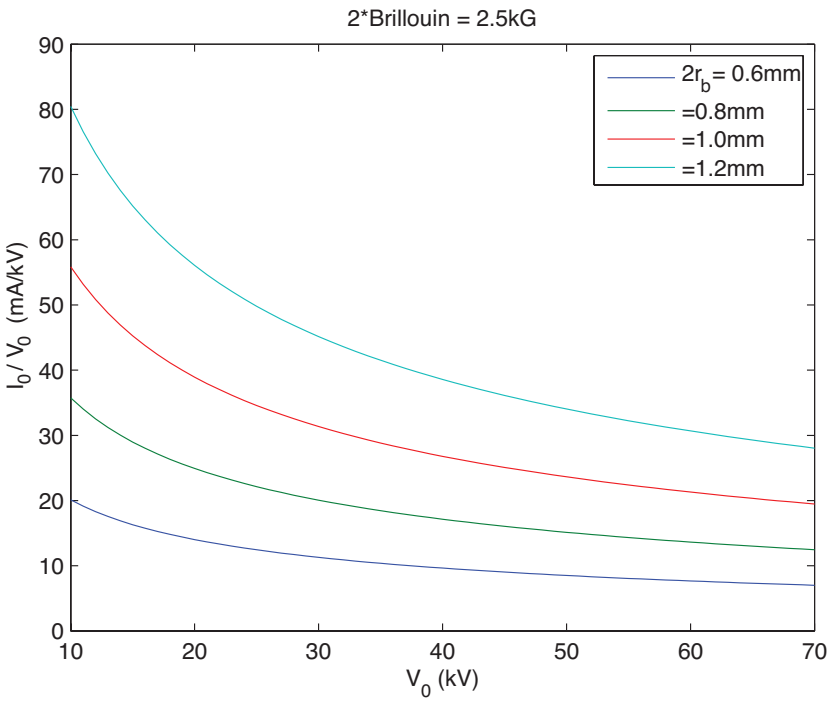

Figure 3-11: I_0/V_0 ratio vs. operation voltage, V_0 for different electron beam radii (and subsequent electron beam tunnel radii). The I_0/V_0 limitation was calculated considering a magnetic field of 2.5 kG, and operation at 2 times the Brillouin field condition.

current and voltage that can be supported by a 2.5 kG field with various beam radii, assuming an operation condition of two times the Brillouin field (generally recognized as a safe operation condition), $B_z = 2B_B$. From this graph, it's clear that the I/V ratio scales significantly with the size of the beam radius. In this regard, a larger beam tunnel will allow the TWT to reach high gain while still operating in a relatively small magnetic field.

Another component of gain is the interaction length and period of the TWT. Arbitrarily, we could set the length at any value to obtain the gain that we desire. (Though a long TWT will limit the peak power and bandwidth that can be obtained.) In reality, several factors limit the achievable gain in the device. These factors can be split into mechanical factors and interaction factors. The main mechanical factor that limits the length of the device is the solenoid magnet that will be used in this experiment, which has a limit on the flat-top field region that can be used in the

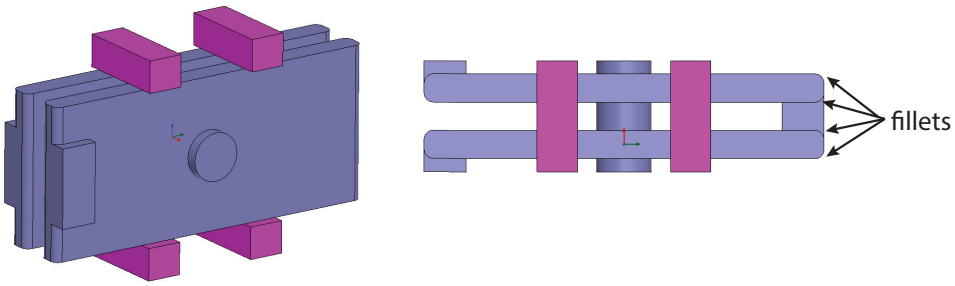

Figure 3-12: The final cavity design showing the dielectric loading and manufacturing fillets which create a small internal radius on part of the cavity structure.

interaction length, about 10 cm. The interaction factors that limit the length of the circuit deal with saturation, bandwidth, and velocity spread. As the circuit becomes longer, the velocity spread of the electron beam limits the gain per unit length in the device and can be detrimental. In addition, the circuit must end prior to saturation occurring; this is a design consideration which limits the peak power achievable in the device. Also, longer circuits have more gain but less bandwidth. Therefore, the trade-off in factors must be considered. With iteration in design, it was found that the entire length of the circuit should be kept to less than 7 cm, which allows for a high gain and high peak power though it limits the bandwidth and operation efficiency.

For the circuit, the period length is simply determined by the operation voltage. At high voltage, less current can be pushed through the system, and the gain decreases. However, at low voltages, the cavities become difficult to manufacture. For this reason, a modest voltage of about 31 kV was chosen, leading to a period length of 0.8 mm. Combined with the 7 cm interaction length, this leaves room for about 90 cavities in the full circuit. In the end, an 87 cavity structure was chosen.

One thing to consider in the design is the manufacturing process. A picture of the vacuum space for the final TWT design is shown in Figure 3-12, where fillets have been added to some of the corners of the cavities. This design takes into account manufacturing practicalities; the cavities will not be perfectly rectangular. This rounding is due to the manufacturing via CNC machining that will be discussed in Chapter 4. The rounding, if not accounted for, would lead to an offset in the cavity frequency from the design. However, the rounded corners can lead to long simulation times.

Table 3.1: Dimensions of Final Structure

Property	Variable	Size (mm), Design A	Size (mm), Design B
Cavity Width	cw	5.60	5.79
Cavity Height	ch	2.54	2.54
Cavity Length	cl	0.40	0.40
Slot Width	sw	0.60	0.60
Slot Height	sh	1.30	1.32
Beam Tunnel Radius	r	0.40	0.40
Dielectric Height	dh	0.30	0.53
Dielectric Width	dw	0.70	0.58
Period	p	0.80	0.80
Fillet Radius	r_f	0	0.13

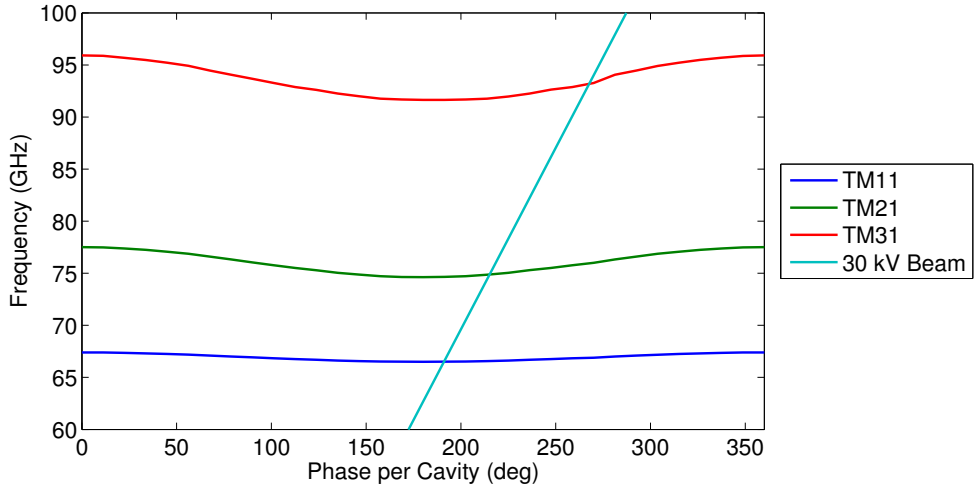

Figure 3-13: The dispersion relation for the first three cavity modes of Design A, as calculated by HFSS.

For the majority of simulations, fillets were not included; the design with no fillets is referred to as Design A. Meanwhile, Design B included fillets and simulations with this design were only used to check that the coupling impedance and frequency of the manufactured components would be similar to Design A. The final dimensions for both Design A and Design B of the TWT circuit are depicted in Table 3.1.

Using the final dimensions from Table 3.1, the parameters of the circuit were calculated in HFSS. Figure 3-13 shows the dispersion relation for the first three modes of the structure specified as Design A along with a 31 kV electron beam. The 31 kV

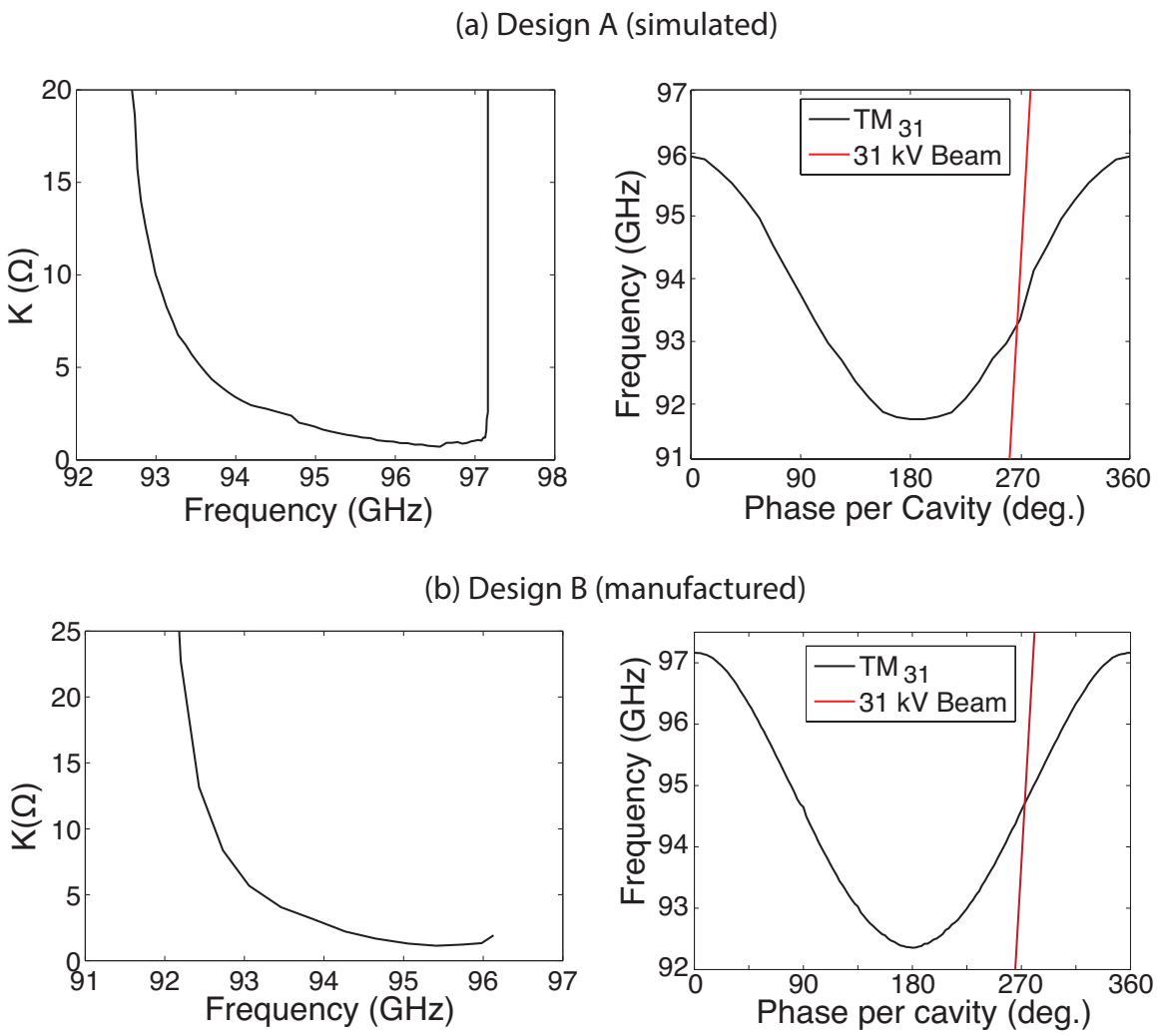

Figure 3-14: The coupling impedance and dispersion relation as calculated by HFSS for the cavity design (a) for Design A without fillets and (b) for Design B with fillets.

electron beam interacts with the mode at 93.86 GHz. Figure 3-14(a) shows the dispersion and coupling impedance calculations for both designs discussed operating in the TM_{31} mode. In experiment, an electron beam between 26 kV to 36 kV could interact with the TWT at different frequencies. The calculations for the coupling impedance of the TM_{31} mode assume an ideal electron beam. At 94 GHz, the coupling impedance is 3.2 Ω for Design A. For completeness, Figure 3-14(b) shows the coupling impedance and dispersion relation as calculated for Design B, which accounts for fillets in the cavities due to the manufacturing process. The frequency has shifted higher by 1 GHz, however the impedance is still comparable to Design A. Since Design

A is easier to simulate, those parameters will be used in the next section. These calculations show that Design B is close enough for reasonable expectations in circuit parameters.

Note that this coupling impedance is small in comparison to the coupling impedance for a fundamental-mode coupled-cavity TWT. This is due to the fact that the electromagnetic field is spread throughout the cavity more than the fundamental mode would be. However, the gain lost due to a low coupling impedance will be compensated by a larger beam tunnel allowing for a large current to interact with the wave. The beam tunnel of the design is 0.8 mm in diameter and this beam tunnel is larger than all other W-band TWT experiments. In addition, the magnetic field of 2.5 kG is lower than all other W-band TWT experiments. These decisions lead to a design with a modest current.

For the mode of operation, the loss in the circuit is due to a combination of ohmic and dielectric losses in the cavity. These losses are due to both the copper walls of the cavity, which were simulated with a finite conductivity, and the dielectric loading in the structure. HFSS predicted that the loss would be about 0.3 dB per cavity in the TM_{31} mode; about half of the loss is due to the copper conductivity and half is due to the AlN composite dielectric loading.

3.2.5 Other Design Considerations

It should be noted that the design discussed in the previous section was kept simple due to manufacturing considerations. Many other components can be taken into account with the design, but were rejected because they impeded the practicality of implementation in the circuit.

For example, the coupling slot in the final design was kept along the edge of the cavity. This detail simplified the manufacturing. Yet, the slot could be designed to be anywhere inside of the cavity. Placing the coupling slot at a location with a larger electric field would lead to a higher coupling impedance but less bandwidth in the circuit. Though the design could be optimized for 94 GHz operation, the difficulties it presented in manufacturing were too large and designing an offset in the coupling

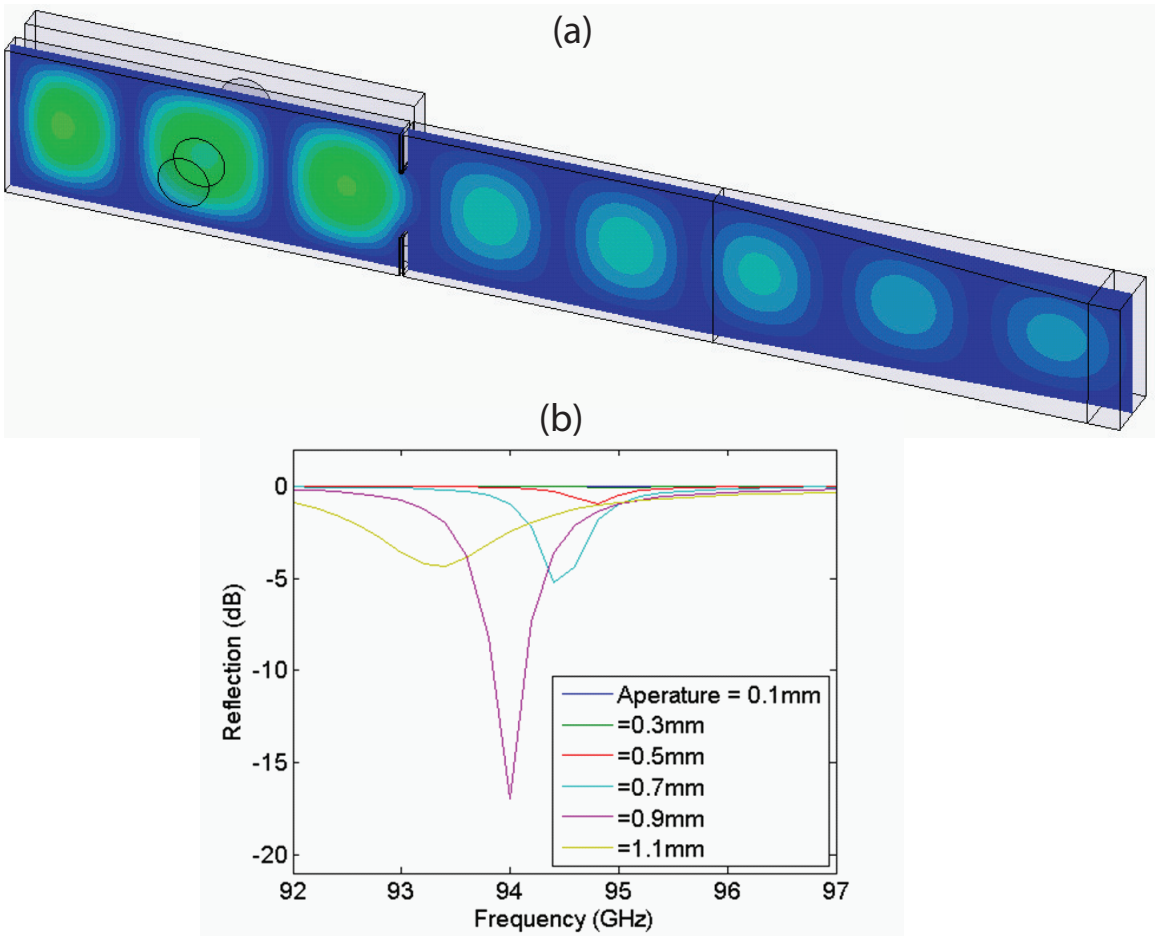

Figure 3-15: (a)The input coupler from standard waveguide into the first cavity of the TWT. (b) Reflection from the cavity structure back to the standard waveguide port for different sizes of the coupling aperture. The optimized aperture design is shown.

slot was not pursued.

In addition, a coupler was designed for the circuit that could be used at both the input and output of the circuit. A schematic of an input coupler is shown in Figure 3-15(a) and HFSS results for the reflection from the input coupler are shown in Figure 3-15(b). By adding an aperture at the entrance to the first cavity, the reflection from the cavity was greatly reduced [56]. However, manufacturing of this small feature was not practically possible due to the delicate nature of the thin aperture walls, so it was not implemented in the final design.

Another design consideration is the addition of a sever about mid-way through the interaction length of the circuit. A sever is a point in the circuit where the

electromagnetic wave is completely absorbed. The sever is typically a matched load or an area of large diffraction losses placed about midway through the circuit. This causes a high loss point in the circuit where the RF wave is dissipated, but the beam remains bunched. The bunched beam re-enters a second length of interaction circuit after the sever and continues to amplify the RF wave. A sever has little effect, less than 3 dB, on the overall gain of the circuit while preventing oscillations. If the circuit were not lossy, reflections from the output could result in oscillations in the circuit. In general, the "round trip" transmission of the circuit must be below zero for output reflections to not be problematic. That is, the gain that is seen in the forward wave must be less than the loss that is seen in a reflected reverse wave. Simulations will show in the next section that there is enough loss in the system (0.3 dB/cavity) due to the dielectric loading to prevent oscillations. Therefore, a sever is not necessary for stable operation.

3.3 Analytical Calculations and Simulations

With the design of the cavity in HFSS, the TWT gain and bandwidth can be simulated with a variety of methods. First, we will look at analytical calculation and consider 1-D simulations. These calculations consider the loss, coupling impedance, and dispersion relation as calculated by HFSS. As the final steps in the design, 3-D Particle-in-Cell (PIC) simulations of the full cavity were performed in CST Particle Studio.

3.3.1 Pierce TWT Analytical Theory

Analytical calculations using Pierce TWT theory, as described in Chapter 2, can be solved assuming parameters as calculated by HFSS. Table 3.2 depicts the operation parameters taken for the calculations. In addition, dispersion relation and coupling impedance as shown in Figure 3-14(a) were used in calculations.

First, consider ideal synchronous motion without losses. In this case, the gain evaluates to $G = -9.54 + 47.3CN$ [dB]. The Pierce parameter C can be solved with

Table 3.2: TWT Operation Parameters

Property	Variable	Value
Voltage	V_0	31.1 kV
Current	I	310 mA
Beam Radius	r_b	0.3 mm
Magnetic Field	B_0	2.5 kG
Number of Cavities	n	87
Synchronous Operation Frequency	f	94 GHz
Coupling Impedance at 94 GHz	K	3.2 Ω
Loss per cavity	l	0.3 dB

the known parameters, such that $C = 0.0203$. The number of wavelengths in the synchronous system is

$$N = Lf/v_p = pnf/v_e \tag{3.17}$$

where L is the entire length of the circuit and n is the number of cavities in the circuit. With 87 cavities in the interaction structure, $N = 65.24$ wavelengths in the structure at 94 GHz. In this case, the ideal gain in the circuit is calculated to be 52.8 dB.

Though impressive, the ideal calculation is not practical. Non-synchronous motion, space charge effects and loss must be taken into account. Figure 3-16 shows the calculated gain under these conditions. (These parameters were also used to calculate Figure 2-7.) It can be seen that space charge limits the hot-circuit bandwidth of the device. However, the TWT still performs with above 40 dB of gain. Taking loss into account, the gain is further reduced to 30.4 dB.

Simulations from 1-D LATTE were used to collaborate with the analytical theory and 3-D simulations. LMSuite LATTE is a code which solves the non-linear gain equation for TWTs [74]. Since it is a quick 1-D code, it is easy to run simulations while designing the TWT with parameters such as the dispersion relation and coupling impedance calculated via HFSS. A comparison between LATTE and Pierce analytical theory for the design parameters shows good agreement. It should be noted that LATTE calculates the velocity of electrons assuming non-relativistic

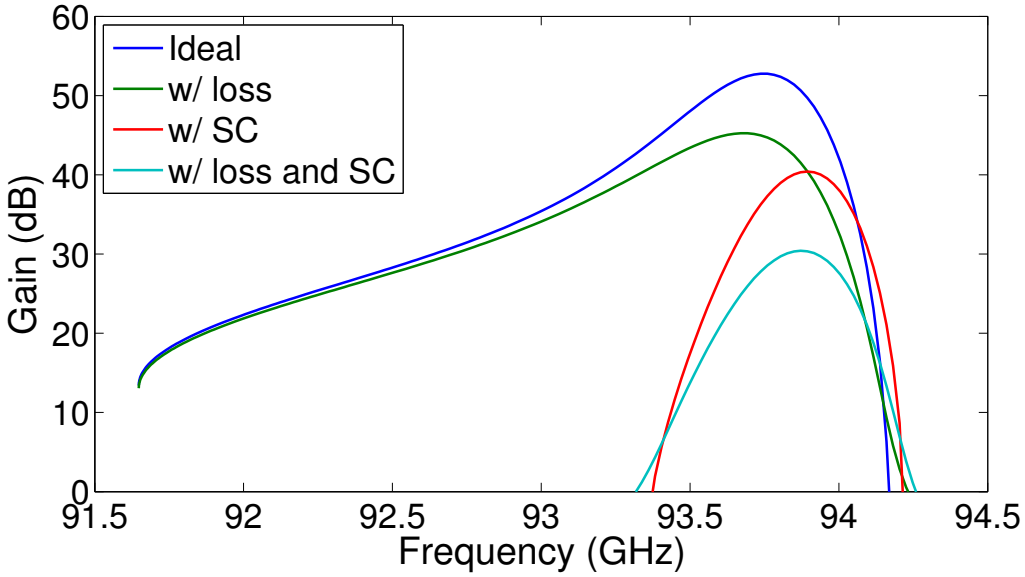

Figure 3-16: Linear gain vs. operation voltage for 94 GHz operation and design parameters discussed in Table 3.2. Calculations with and without space charge and/or loss were considered.

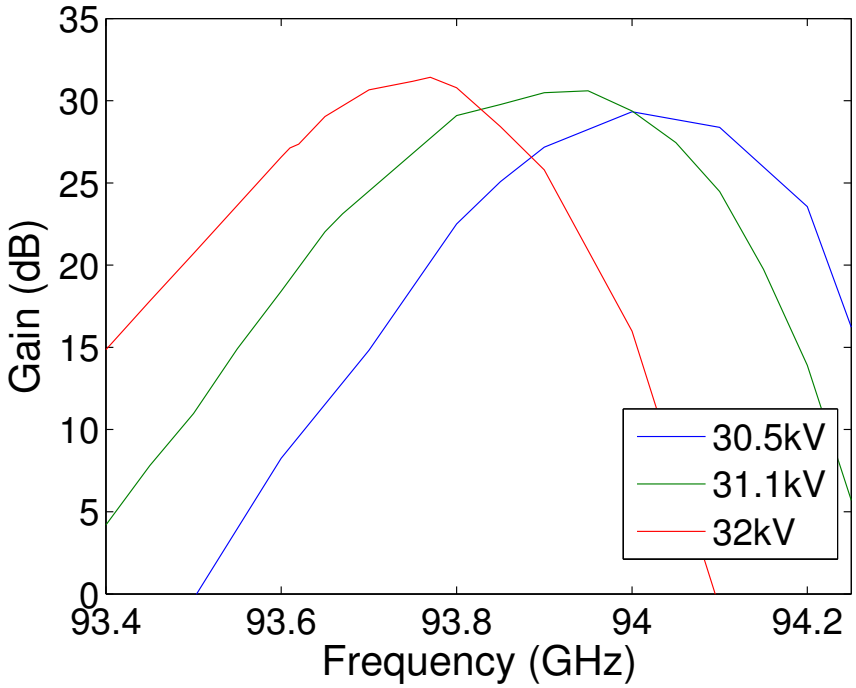

Figure 3-17: Linear gain vs. frequency for LATTE simulations at various operation voltages, V_0, with all other operation conditions as described in Table 3.2.

operation. For the device designed in this thesis, relativistic effects cannot be ignored; therefore, this graph and all LATTE results reported in this thesis correct for relativistic velocity from the LATTE results. This is done by calculating the relativistic operation voltage during post-processing from the electron velocity, v_e, that was used in LATTE simulation,

$$V_{rel} = 511 \left(\frac{1}{\sqrt{1-(v_e/c)^2}} - 1 \right) \text{ [kV]} \tag{3.18}$$

Note that this calculated voltage does not agree with the voltage set in the LATTE simulation. Figure 3-17 shows the gain vs. frequency output from LATTE for various operation voltages. Via these simulations, the operation parameters shown in Table 3.2 were optimized along with cavity parameters which were determined via HFSS calculations for the coupling impedance and dispersion relations as shown in the previous section.

3.3.2 3-D CST Simulations

3-D CST Particle Studio is a PIC code which was used to simulate the entire operation circuit with a realistic electron beam and magnetic field. These calculations refined the design from the 1-D simulations and agreed well with previous results. CST simulations also helped direct the design to prevent oscillations in the system: both oscillations in the fundamental mode of the cavity as well as round-trip oscillations in the operation mode were eliminated.

Figure 3-18 shows the entire 87 cavity structure as it was simulated in CST. The cavity parameters and operation parameters used have already been discussed. The RF input and output ports are at faces in the cavity which face away from the circuit, as shown in Figure 3-18. These ports are the same height as WR-10 waveguide. In the final design, a simple taper along the width of the WR-10 waveguide is utilized to couple from fundamental waveguide into the overmoded cavity.

CST 3-D particle studio launches an electron beam with an angular velocity and a percentage of velocity spread. For these calculations, 1 % velocity spread was

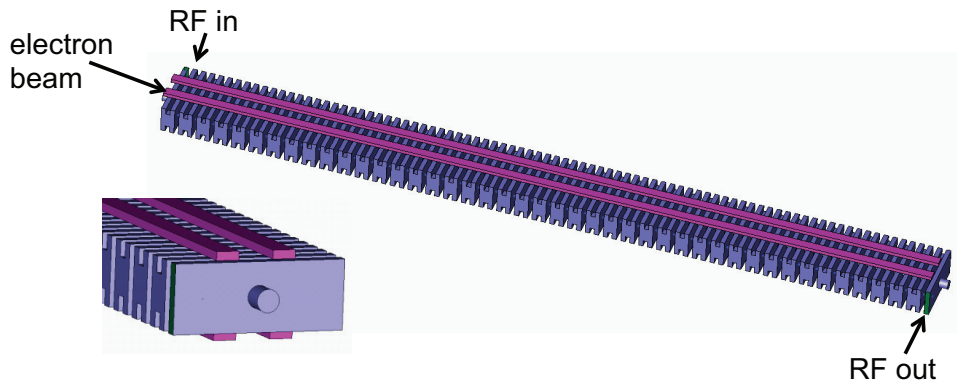

Figure 3-18: The full 87 cavity structure with dielectric loading as simulated in CST. The vacuum sections of the circuit are shown in purple, and the dielectric is shown in pink. An electron beam source transmits electrons through the beam tunnel. RF input and output ports are outward-facing sides of the the first and last cavities.

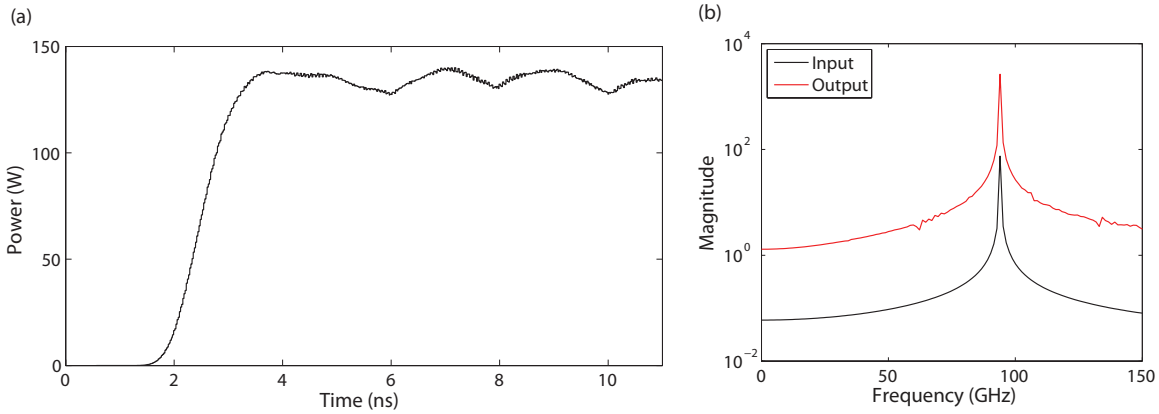

Figure 3-19: Output power vs. time for a 90 mW input signal along with an FFT of the output signal, showing oscillation at the TM_{31} input frequency of 93.86 GHz.

considered with no angular velocity. These electron beam characteristics will be discussed with the design of the electron gun in Chapter 5. Figure 3-19(a) shows a sample of the output seen from a CST simulation. The power at the output port is shown versus the simulation time for an input signal of 90 mW. A small-signal gain of 31.8 dB is observed. A very small reflection at the output is observed at the start of amplification. Since there is no return reflection at a later time in the simulation, this indicates that the round trip transmission is greater than zero and that oscillations will not be problematic in the circuit. This means that the loss seen by the backward wave is greater than the gain seen by the forward wave in the circuit. If less loss is

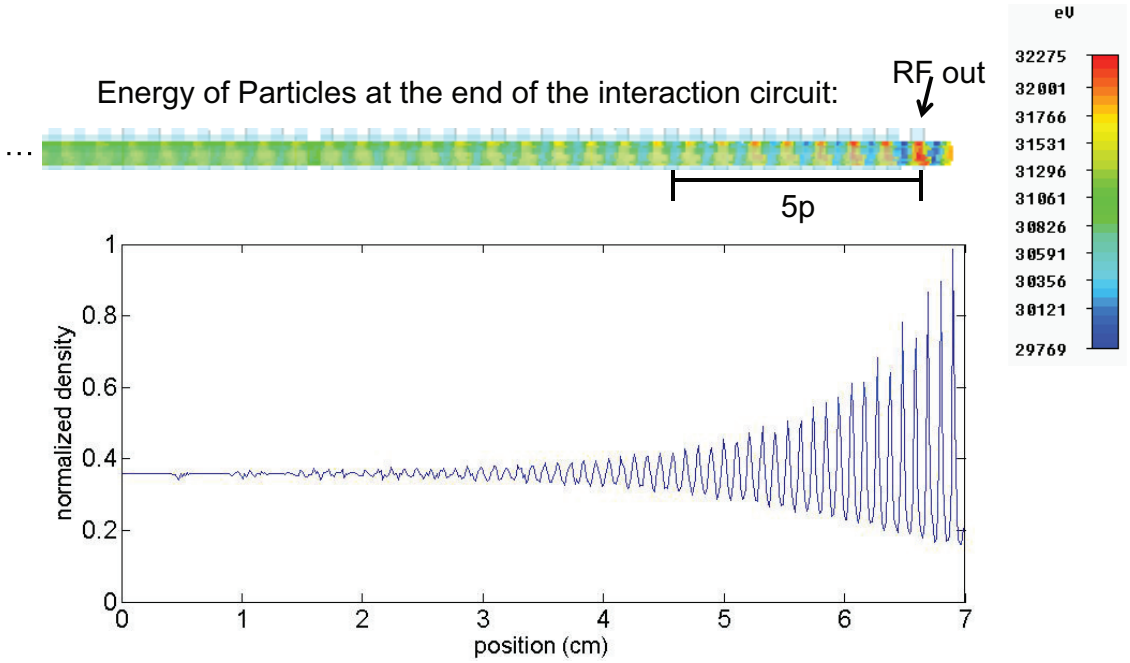

Figure 3-20: The energy of the particles in the beam tunnel at the end of the circuit, and the particle density along the length of the cavity.

considered in the circuit (by simulating the circuit with less dielectric loading), round-trip transmission greater than zero is observed along with oscillations that develop at the operation frequency. The ringing that is seen later in the pulse is due to low sampling of the data (which was recorded as electric field magnitude). Figure 3-19(b) shows the frequency components of the output and input signals in the device. The simulation indicates that the output signal is oscillating at the frequency of interest. No evidence of the TM_{11} mode at 65 GHz is seen in the signal, indicating that the dielectric successfully suppresses the fundamental mode from self-oscillating as well. There is a slight dip at 64 GHz and at 130 GHz which are orders of magnitude less than the amplified signal, but the signals never develop throughout the duration of the simulation, indicating that they will not be a problem.

The bunching of the circuit is shown in Figure 3-20 for a 10 mW input signal. It is seen that by the end of the circuit, electrons have both gained and lost energy (indicative of correct bunching in the TWT). An analysis of the particles in the simulation shows that bunches have formed at the end of the circuit. Since the bunches have not yet dispersed, this indicates that the simulation for 10 mW of

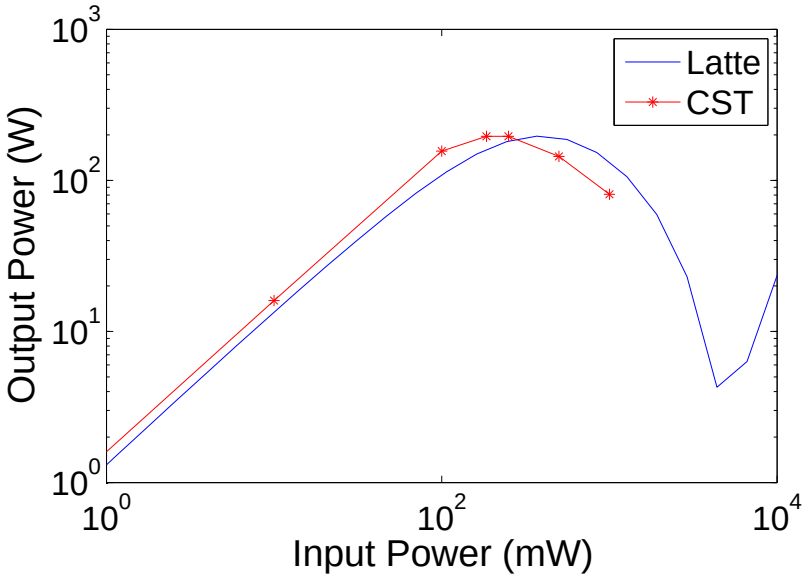

Figure 3-21: Output power vs. input power for the simulated TM_{31} coupled-cavity TWT as calculated in 1-D LATTE and 3-D CST Particle Studio. Linear gain and saturated output are shown.

power is lower than the saturation point of the TWT.

The gain and saturated output power that are predicted by CST are shown in Figure 3-21 alongside simulations from 1-D LATTE. The CST simulations predicted 32 dB of gain and 300 W peak output power. CST also shows stable operation for the 94 GHz amplifier and no evidence of oscillations in the fundamental mode were seen in the simulation. The good agreement between the two methods of simulation for the TWT indicate that the analysis is correct and follows our understanding of the TWT analytical theory.

With these results, a TWT amplifier operating in the TM_{31} mode has been successfully designed. The lower order modes will be suppressed with selectively placed lossy dielectric loading. It has been designed with experimental considerations so that it may be implemented. The overmoded TWT is predicted to have 32 dB of gain, 300 W peak output power, and 200 MHz bandwidth for the parameters of the design.

Chapter 4

Cold Tests of the Overmoded TWT Circuit

Before considering the experimental implementation of the TWT, it is useful to discuss cold tests of the overmoded TWT cavity designed in Chapter 3. These successive measurements were used to refine the mechanical design and machining process of the cavities prior to final experimental implementation. In this Chapter, the machining and assembly for the TWT structure will be discussed in detail along with cold test results and final design specifics.

4.1 Machining Techniques and Tolerances

One of the main difficulties in making W-band TWTs is machining the detailed structures necessary for interaction at high frequencies. By making an overmoded design, machining is easier than other TWTs due to its oversized nature. However, machining still requires careful consideration. To deal with small features, many W-band TWTs utilize nano-fabrication techniques [19] [3]. Development has also gone into UV-Liga fabrication for high-frequency structures [35]. The work in this area is important to the development of TWTs, especially at high frequency. However, with the overmoded design, the structure is able to be built with less complex machining. One goal of this thesis is to demonstrate the experimental operation of a W-band TWT using traditional machining techniques.

Two machining possibilities were considered for this structure: Wire EDM and

direct CNC machining. First, Wire Electrical Discharge Machining (EDM) was used along with a 4-plate design. The 4-plate design, shown in Figure 4-1(a), has the cavities machined through the inner two plates; wire EDM was used to cut the beam tunnel into the middle of block and to cut the cavities and input and output ports through the entire width of the inner two plates. The coupling slots between the cavities were machined separately. Second, the entire structure was redesign as a 2-plate structure and constructed with a Computer Numerical Control (CNC) milling machine (and an appropriately experienced machinist), as depicted in Figure 4-1(b) and (c). With both techniques, precise alignments and sub-mil (1 mil = 0.001 inches = 0.0254 mm) tolerances were achievable. With CNC milling, it was necessary for the design to have a sufficiently small width-to-depth ratio for the end mill that was used during machining. That is, the depth of the cavity is limited by the width of the cavity due to the fact that an end mill must be long and thin enough to create those dimensions within the metal block without breaking.

Both the 4-plate and 2-plate structures could be brazed together in order to finish the structures. Commercial TWTs are typically finished with this process since the cavities themselves must hold vacuum and brazing the cavities together would achieve this requirement. The ability to hold vacuum is not necessary for the cavities tested in this thesis. Chapter 5 will discuss the tube design for the experimental implementation of the TWT, which holds the overmoded TWT inside of a vacuum test chamber. Since the cavities in this design do not have to hold vacuum themselves, brazing the final structure was not a consideration in the machining. Since brazing often leads to complications in the design, the decision was made to opt-out of brazing which led to a quicker turn-around and analysis time for test structures. This decision does not invalidate the design for commercial use.

The 4-plate structure has an easier construction than the 2-plate structure, but is inherently flawed in design. During cold-test, it became evident that extreme pressure was needed to sufficiently clamp the 4-plate structure together and achieve transmission through the structure. As can be seen in Figure 4-1(a), when the plates are mated together, there is the possibility of three gaps which would cut through

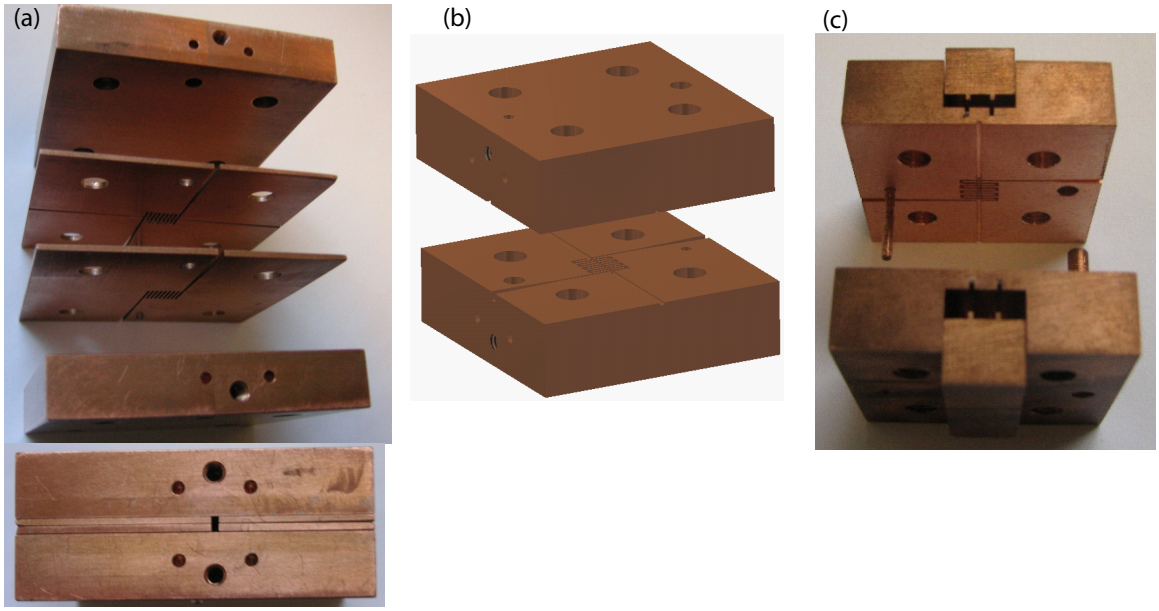

Figure 4-1: The assembly of the (a) 4-plate design, and (b) A CAD model of the 2-plate design for the 9-cavity cold test structure. (c) The assembly of the 2-plate design with dielectric loading added.

the design of the structure. Indium foil was placed between the cavities and outer plates (to fill the top and bottom gaps) in order to achieve measurable S-parameters through the 9-cavity structure. Though indium foil has a low melting temperature, it could be used in vacuum and was malleable enough to fill the gaps left between the plates. However, the transmission achieved was not sufficient. There was significant coupling at 94 GHz into the structure, but very high losses and minimal transmission.

The poor transmission in the 4-plate structure was due to the coupling of the electromagnetic wave into the gaps between the plates. Figure 4-2 shows how a wave will travel through WR-08 waveguide with gaps at the top, middle, and bottom of the guide. The gaps make parallel plate waveguides that intersect the WR-08 rectangular waveguide. The fundamental waveguide mode, TE_{01} couples into the TEM mode of the parallel plate waveguides formed by the top and bottom gaps, and power is lost. Fortunately, there is little coupling of power into the middle gap, as shown in Figure 4-2. These results are universal for any fundamental waveguide arranged in this manner; the electrical field is aligned correctly to couple well into the top and bottom gaps and does not couple into the middle gap [50]. A slight misalignment of the gap

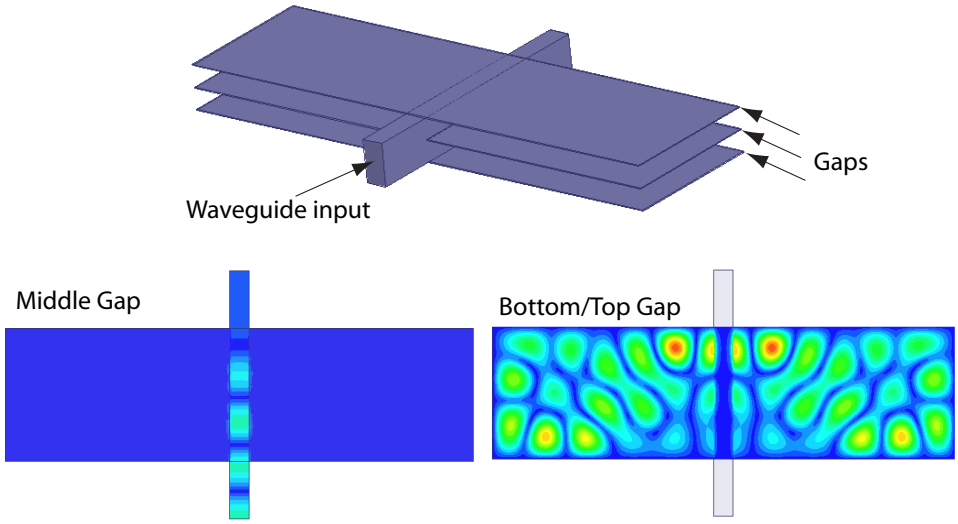

Figure 4-2: HFSS simulations showing a WR-08 waveguide with gaps at the top, mid-plane, and bottom of the waveguide. A 95 GHz wave was excited at the input. The simulated electric field magnitude in the middle gap and top/bottom (identical) gap is shown, indicating that the electric field couples well from the waveguide into the top and bottom gaps.

from center would lead to some losses into the middle gap, but this loss could be eliminated by introducing a quarter-wavelength choke flange in the gap, which would reflect any energy that couples into the gap [45]. Unfortunately, the TWT structure is too complex for the choke flange to be added, but the loss associated with the middle gap is small enough that it should not be problematic.

Though the 4-plate design was simpler than the two plate design, the transmission was inadequate. On the other hand, the next section will show that the 2-plate design had adequate transmission since a mid-plane gap is not susceptible to very high losses. Though the dielectric placement is complex in the 2-plate design, it is not insurmountable. For placement, slots must be machined from above the cavity and require care in machining, as shown in Figure 4-1(c).

The tolerances of the design were determined via HFSS simulations. For most features, ± 1 mil tolerances were sufficient for frequency and coupling consistency. The placement of the plates was held to the highest tolerance achievable and aligned with precision pins. Rounding on the corners with CNC milling was kept to 5 mils; the corners that must be rounded during fabrication were highlighted in Chapter 3

with the discussion of fillets in simulations.

4.2 Low Power Cold Test Measurements

For these measurements an Agilent 2-port General-Purpose Network Analyzer (PNA) was used with WR-08 millimeter wave heads. The heads are rated for use from 90 GHz to 140 GHz, but operation is possible between 74 and 140 GHz (WR-08 waveguide cuts off at 73.8 GHz). It is considered a "cold test" since no electron beam is in the circuit. In addition, all measurements were performed with low powers. These tests were designed to refine the machining process and explore variations for the cavities. Therefore, different materials and lengths of structures were tested in the process. Since only WR-08 equipment was available for measurements, the TM_{11} (67 GHz) and TM_{21} (72 GHz) modes could not be measured; they are below the cutoff of WR-08 waveguide. However, it is sufficient to measure the TM_{41} mode to know how unwanted modes are transmitted within the structure and compare the measurements to theory. If the measured modes agree with theory (HFSS), we can extrapolate that the TM_{11} and TM_{21} modes would also agree with theory and would behave as expected in the structure.

4.2.1 Materials

When considering material for construction of a coupled-cavity structure, Oxygen Free High Conductivity (OFHC) Copper is typically the best candidate. Though the material is malleable and difficult to machine, it is great for vacuum compatibility and has a high conductivity. This means that there is little ohmic loss over the course of a long structure. Most other materials that have a high conductivity and are harder than copper are typically not ideal for vacuum. For example, brass is easy to machine and has a high conductivity, but it has a low vapor pressure and is unable to be placed in an ultra high vacuum system. In addition, zinc (a component of brass) can poison an M-type thermionic cathode, causing reduced current emission. However, harder materials than copper are ideal for machining, since the material

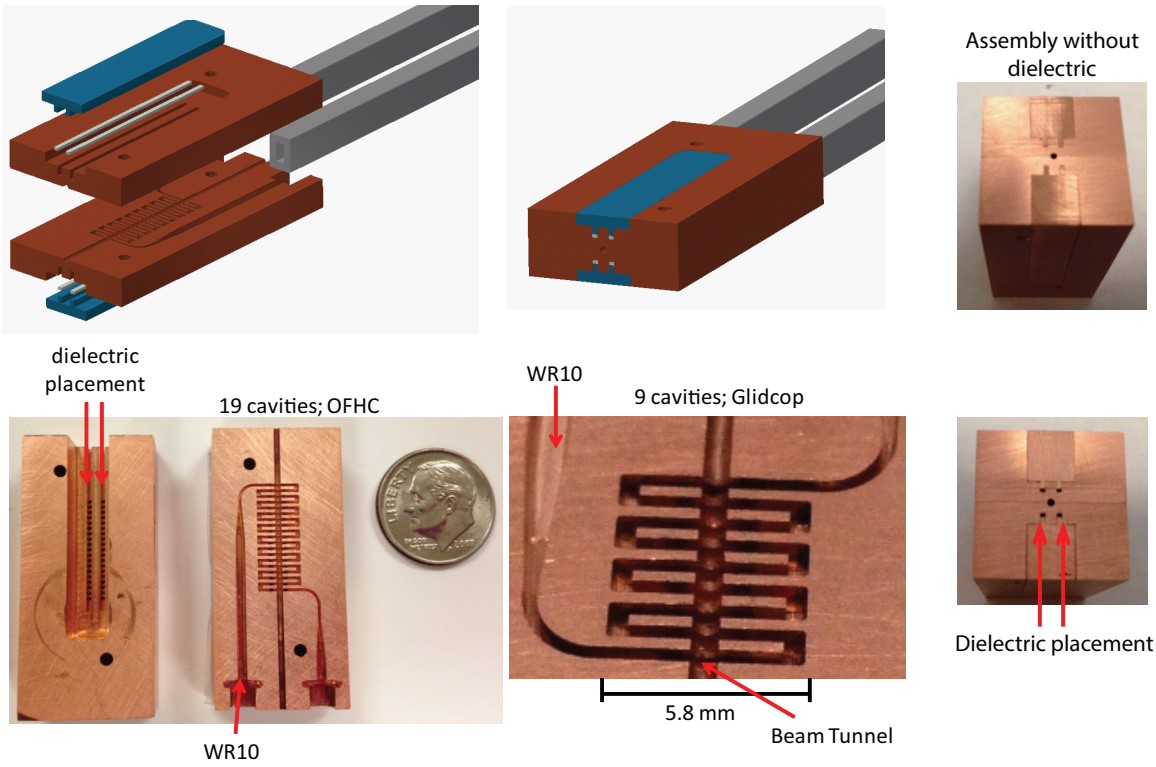

Figure 4-3: CAD drawings and machined 9 and 19 cavity cold test structures which were made out of OFHC copper and LOX glidcop. Slots were machined into the top of the cavities which could be filled with a copper insert or with dielectric loading.

is less likely to deform under stress and easier to machine with clean and consistent edges and surfaces.

Glidcop is another material that was considered in this thesis. Glidcop is a trademark copper alloy of Höganäs, Inc, a company that specializes in alloys and manufacturing techniques. It consists of copper that has been impregnated with a small amount of alumina (Al_2O_3), which leads to a small reduction in the electrical and thermal conductivity, but enhances the high temperature strength of the alloy. This leads to a material that is less susceptible to deformation during the stress and temperature rise of machining, but it has all of the positive aspects of copper for a vacuum application. Various types of glidcop exist with different percentages of alumina content, where higher percentages have a correspondingly higher threshold for thermal stresses and lower electrical conductivity (or higher resistivity). For example, AL25 glidcop has 0.25 wt.% alumina and 1.98 $\mu\Omega$-cm resistivity, while AL60 glidcop has

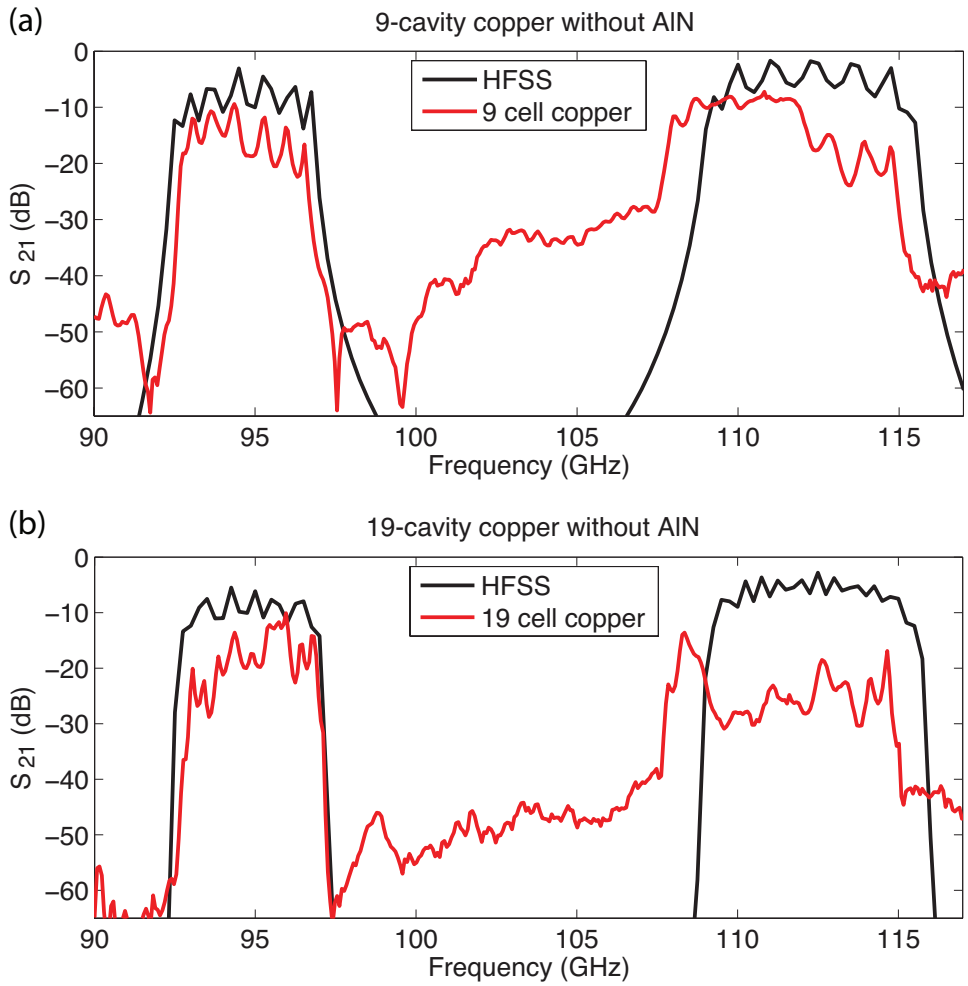

Figure 4-4: The measured transmission through (a) 9- and (b) 19-cavity OFHC copper structures compared to HFSS simulations.

0.6 wt.% alumina and 2.21 $\mu\Omega$-cm resistivity [65] [66]. (For reference, OFHC copper has an electrical resistivity of 1.72 $\mu\Omega$-m.) Though glidcop has a non-insignificant oxygen content, low oxygen (LOX) glidcop is made by impregnating a small amount of boron into the cavity (nominally 250 ppm). LOX glidcop is safe for vacuum and for cathodes and can be brazed, if necessary.

Recently, glidcop has been used in several vacuum devices. Most notable, it has been explored for high gradient accelerators due to its ability to withstand large temperatures [71] [2]. Glidcop has also been used for high temperature joints in the ITER fusion reactor [73] [24]. In addition, glidcop has been successfully used to construct electron gun anodes [14] and high power gyrotrons cavities [69], though

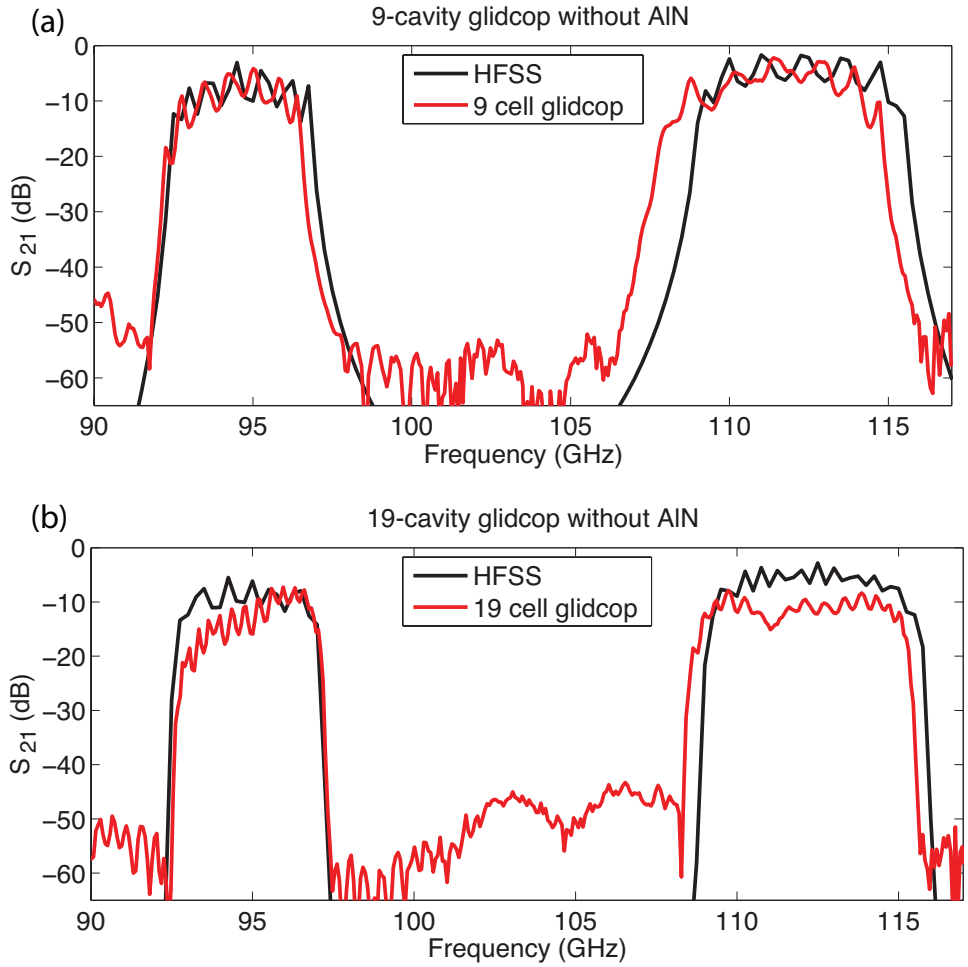

Figure 4-5: The measured transmission through (a) 9-cavity AL60 LOX glidcop and (b) 19-cavity AL25 LOX glidcop structures compared to HFSS simulations.

it has never been used in a TWT amplifier circuit. These experiments have shown that glidcop is able to perform well under high vacuum testing, is safe for operation, and will perform well under high temperature. It has also shown that it will perform well in the possible case of beam interception on the glidcop structure with limited out-gassing and damage due to melting.

For testing, short structures were constructed which consisted of 9-cavities and 19-cavities. These structures were used to test machining techniques, tolerances, coupling into the circuit, losses in the circuit, and the effectiveness of the dielectric loading. Transmission measurements for the copper and glidcop structures are shown in Figures 4-4 and 4-5, respectively. In the figures, the TM_{31} and TM_{41} pass-bands are

visible from 92–98 GHz and 110–115 GHz, respectively. Dielectric loading was omitted from this test and copper placeholders were used to fill in the slots that were machined to hold dielectric. In the copper measurements, it's clear that there is leakage of the TM_{41} mode into lower frequencies; this is evidence of poorly formed coupling slots and unmatched surfaces in the 2-plate structure. In addition, the TM_{31} agrees well with theory, but shows some additional losses in the 9-cavity structure. Figure 4-4(b) shows that the 19-cavity copper structure intensifies the losses observed in the 9-cavity structure. Figure 4-5(a) shows the measurement for a 9-cavity structure made from AL60 glidcop, which agrees very well with HFSS simulation. In addition, Figure 4-5(b) shows the 19-cavity results for AL25 glidcop, and indicates that the longer structure (though made of a softer glidcop alloy) is still in good agreement in theory. This indicates that there are minimal compiled manufacturing errors that would become evident in longer structures.

The resonances observed in both the copper and glidcop structures (also evident in the HFSS simulations) are due to reflections between the cavities. They are visible in these structures due to the low number of cavities that were machined. As more cavities are added to the structure, these resonances will become less resolved across the bandwidth of the mode and there will be a more consistent transmission across the band.

Though both copper and glidcop show good transmission through the cavity in both the 9- and 19-cavity structures, it is clear that the glidcop structures show better agreement with HFSS simulations. The glidcop structures showed increased transmission over the copper structures, even though they have a higher electrical resistivity. This is due to the fact that glidcop is a harder material than copper and was easier to machine to specifications without being susceptible to deformation. Due to its nature as a good vacuum material and the minimal losses measured in the cold test structures, AL60 LOX glidcop will be used in the final cavity design.

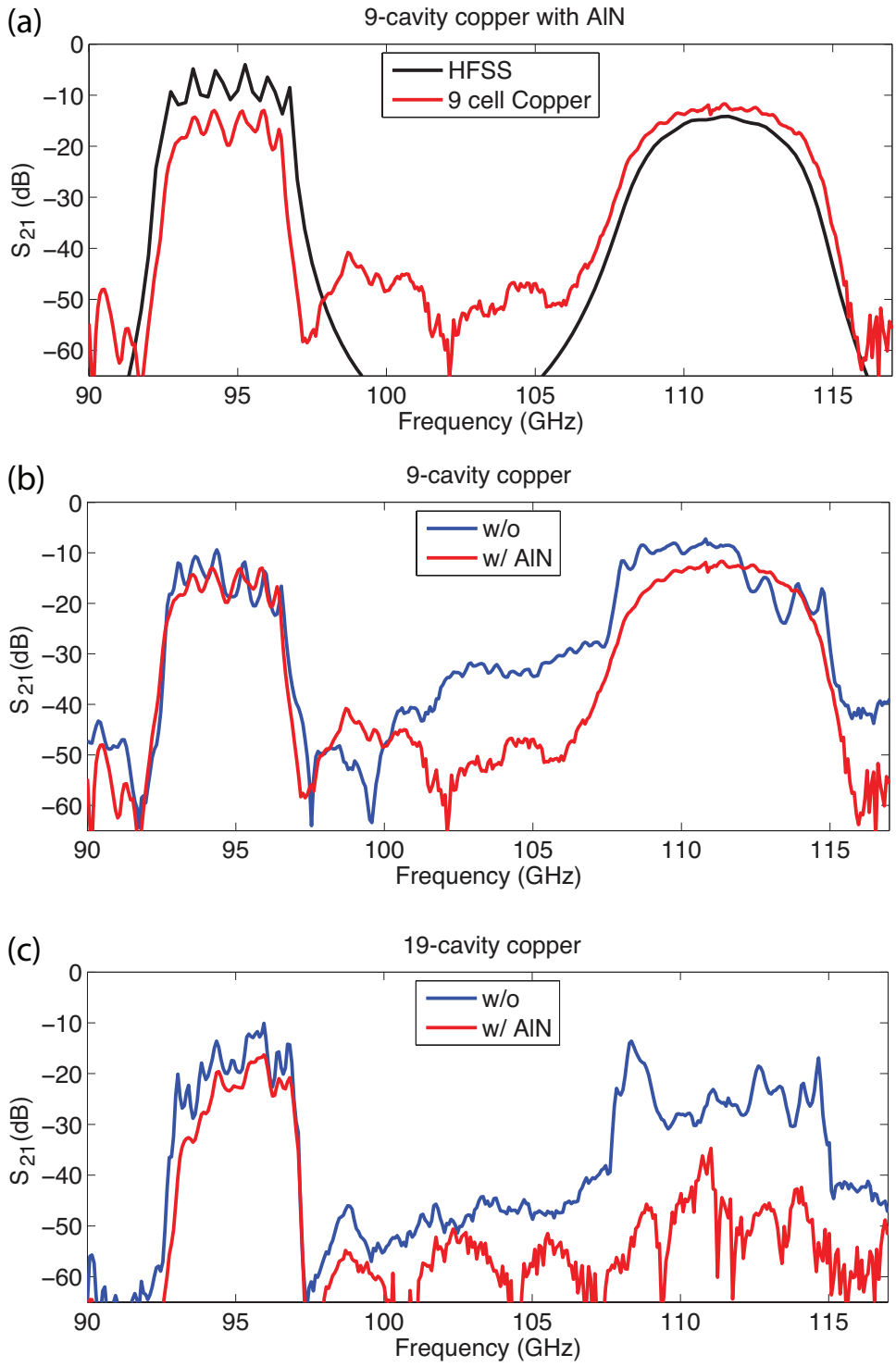

Figure 4-6: For copper structures, the measured transmission through (a) 9-cavity structure with dielectric loading as compared to HFSS simulation along with (b) comparison to results without dielectric loading, and (c) the measured transmission for a 19-cavity structure with and without dielectric loading.

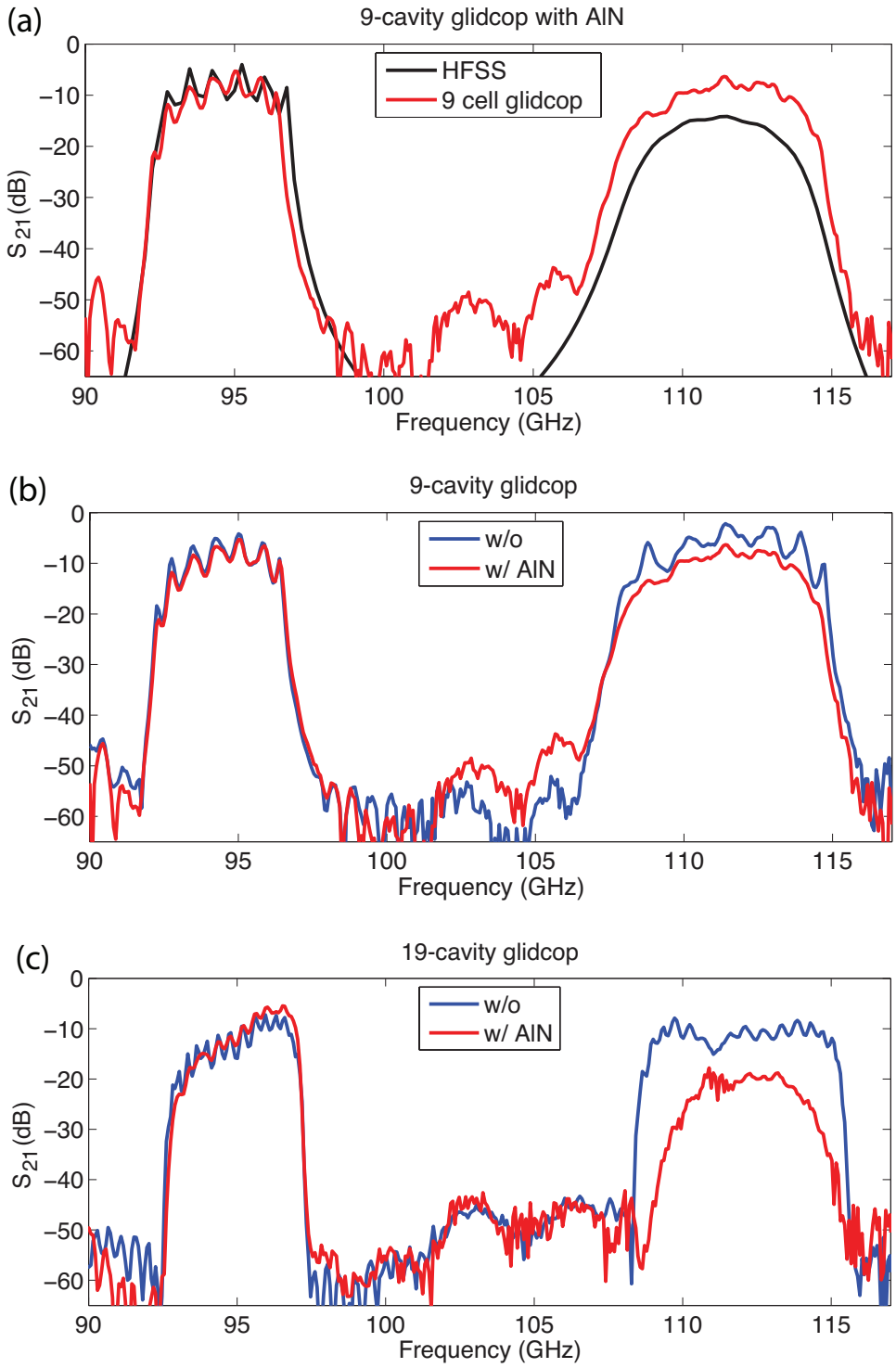

Figure 4-7: For glidcop structures, the measured transmission through (a) 9-cavity structure (AL60) with dielectric loading as compared to HFSS simulation along with (b) comparison to results without dielectric loading, and (c) the measured transmission for a 19-cavity structure (AL20) with and without dielectric loading.

4.2.2 Dielectric Loading

The dielectric used for loading the cavities must have several key properties. The most necessary property is that it must have high loss properties at high frequencies. It also needs to be compatible with vacuum. Though the dielectric loading won't see much stress, it would also be useful to have low heat-loading characteristics in the material. Common dielectrics with low heat-loading and minimal outgassing that are commonly used in vacuum include macor, fused silica, beryllium oxide and aluminum nitride. Macor and fused silica have low loss tangents and will not sufficiently suppress the unwanted modes. Some Beryllium oxide, BeO, composites are able to provide the necessary loss tangents, but BeO is a dangerous material to machine due to health risks and is not commercially used in vacuum systems at the present. Aluminum nitride composites have high loss tangents, are easy to machine, and are easily available.

Previously, a TM_{31} mode cavity was designed at 17 GHz and successfully tested to show lower order mode suppression with Aluminum Nitride (AlN) dielectric loading from Sienna Technologies, a ceramic supplier that deals with specialized composites [10]. The AlN composite suppressed other modes in the circuit, while leaving the TM_{31} mode with little additional losses. There are many types of AlN composite dielectrics, but the most promising one to use is the STL-100c AlN-SiC which has a dielectric loss tangent of $\tan\delta$ =0.32 at 12 GHz and a relative permittivity ε_r =25.

The AlN-SiC 100c composite from Sienna Technologies has good thermal and vacuum properties and was already shown to work in the Ka-band for mode suppression, so it was used as the dielectric for the overmoded TWT in this thesis. The dielectric pieces were machined with high tolerances to the width and height dimensions discussed in Chapter 3. The pieces are 2.54 cm in length, so multiple pieces must be used along the length of the final structure to cover all of the cavities.

The AlN dielectric was placed on top of the cold test cavities, and a copper cover kept the dielectric in place while the structure was under test, as shown in Figure 4-3. Results for the copper structures are shown in Figures 4-6. Figure 4-6(a) shows good

Table 4.1: Coupled-Cavity Loss with Dielectric Loading (dB/cm)

Mode	Simulated	Measured, Copper	Measured, Glidcop
TM_{31}	0.34	0.32	0.26
TM_{41}	1.2	1.4	0.69

agreement of the 9-cavity structure with theory. The dielectric loading very effective suppressed the TM_{41} mode. Figures 4-6(b) and (c) explicitly show the effect that the dielectric has on the transmission of the TM_{31} and TM_{41} modes in the structure by comparing the same structure with and without the dielectric loading in place. It's clear that the TM_{31} mode is affected very little by the dielectric loading. However, the TM_{41} mode has additional losses when the dielectric is added to the structure. In fact, it's clear that the 19-cavity structure has about twice as much additional loss due to the dielectric as the 9-cavity structure. This is due to the fact that the dielectric is adding a distributed loss into the circuit; so more cavities will induce a proportionally larger loss into the system.

The dielectric results for the glidcop structures are shown in Figure 4-7. Figure 4-7(a) compares the measured transmission of a 9-cavity glidcop cold test with dielectric loading against HFSS simulations. Once again, good agreement is shown for the TM_{31} mode between measurement and theory, an improvement over the copper results. Figures 4-7(a) and (b) show the effect that the dielectric has when added to the glidcop structures by comparing measurements made with and without dielectric for the 9- and 19-cavity structures, respectively. It is clear that the dielectric causes decreased transmission in the TM_{41} mode in the same manner as it had with the copper structure.

From the S-parameter measurement, the loss per unit length of the structure can be calculated. The losses as they were calculated are displayed in Table 4.1. It was found that about a 6 dB coupling loss was present in the glidcop structure, which agrees with HFSS simulation (slightly more coupling loss was present in the copper structure). For both materials, about 0.3 dB/cm loss was present with dielectric

loading; also good agreement with theory.

These cold tests have shown that the AlN composite dielectric is selectively suppressing the unwanted modes in the cavities, while having little effect on the wanted TM_{31} mode of operation. Therefore, the AlN composite will be used in the final structure. In addition, the successful performance of the glidcop structures also reinforces the decision to use glidcop rather than OFHC copper in the final structure.

4.3 87-Cavity Design Cold Test Results

After construction of smaller cold test structures, the final full-length structure was constructed with 87 cavities. Figure 4-8(a) shows the 2-plate cavity structure that has been designed for installation in the TWT experiment. The details of the experiment will be discussed in Chapter 5. The assembly of the structure and placement of the dielectric loading on the cavities is highlighted in Figure 4-8(b). This figure also highlights the conical tip around the input of the beam tunnel, which is an alignment surface to allow for the beam tunnel to be aligned with the electron gun and magnetic field axis, as will be discussed in Chapter 4. Figure 4-8(c) shows the fully assembled of the cavity along with input and output WR-10 waveguide components; a standard USB flash drive provides a scale.

Two 87-cavity structures were machined for experimental testing, which will be referred to as Structure A and B for simplicity. Structure A was manufactured first and underwent experimental testing while Structure B was being finalized. The two structures are identical, except for random machining errors, and Structure B was cleaned excessively to remove any machining anomalies, burrs, or errors, in the cavities.

The S-parameter measurements for Structure A are shown in Figure 4-9 with and without dielectric loading. With the dielectric loading in place, the last two cavities of the structure are left empty of dielectric loading and the dielectric is held in place by the copper inserts. For the measurements without dielectric loading, the slots are kept empty, simulations have shown that this set-up is nearly equivalent to the results

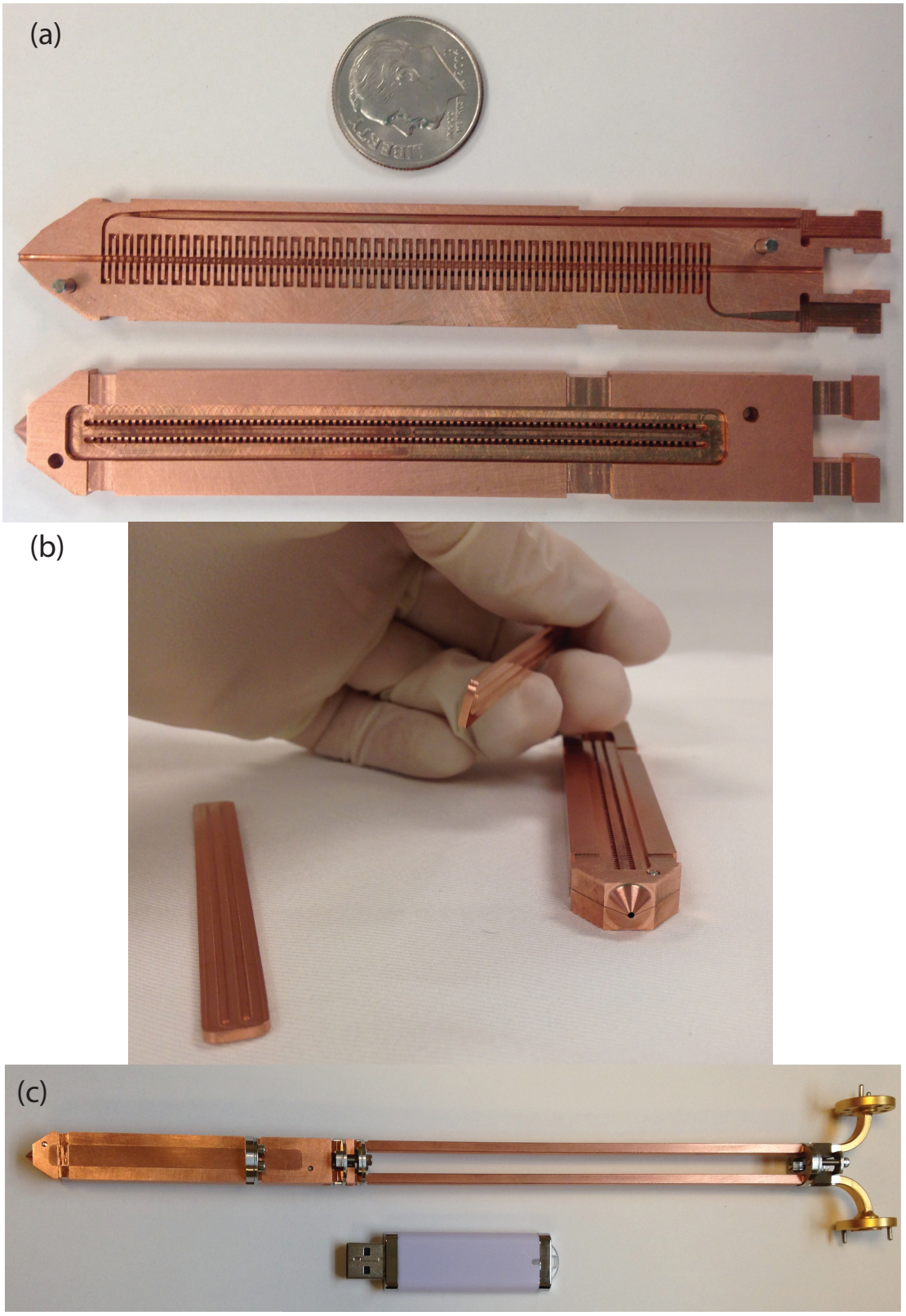

Figure 4-8: (a) The details of the 87-cavity structure with a U.S. dime for comparison. (b) Assembly of the structure, showing the front of the beam tunnel and alignment surface. (c) Assembly of the structure with input and output WR-10 Waveguide.

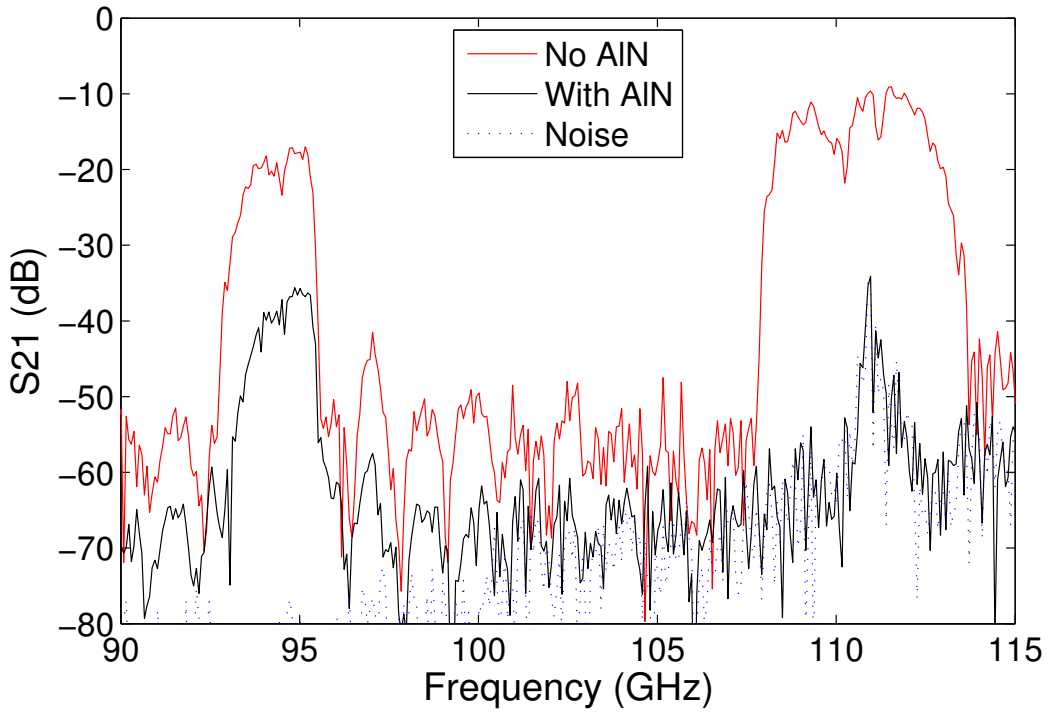

Figure 4-9: Transmission, S_{21}, measurements for the first 87-cavity structure with and without the dielectric loading installed. The transmission in the TM_{31} and TM_{41} modes are shown. The noise floor of the measurement is shown for reference.

with a pure copper cavity.

The dielectric loading performed as expected for the TM_{41} mode. In fact, with even just half of the dielectric loading, the TM_{41} mode is not distinguishable above the noise-floor of the measurement, as shown in Figure 4-9. This shows conclusively that the AlN composite will sufficiently reduce the unwanted modes in the circuit. Due to the high losses seen in the TM_{41} mode, one can conclude that it will not be present during operation. We can extract, too, that the TM_{11} mode will not oscillate since the AlN is performing as expected, allowing for amplification at 94 GHz in the TM_{31} mode.

Figure 4-10 compares the measurement of the transmission with the dielectric loading to the expected transmission. Since an 87-cavity structure would take too long to analyze in HFSS, the simulated data was extrapolated from 9- and 19-cavity simulations. The measured transmission in Structure A for the TM_{31} is about 15 dB less than the predicted transmission, while the transmission in Structure B agrees

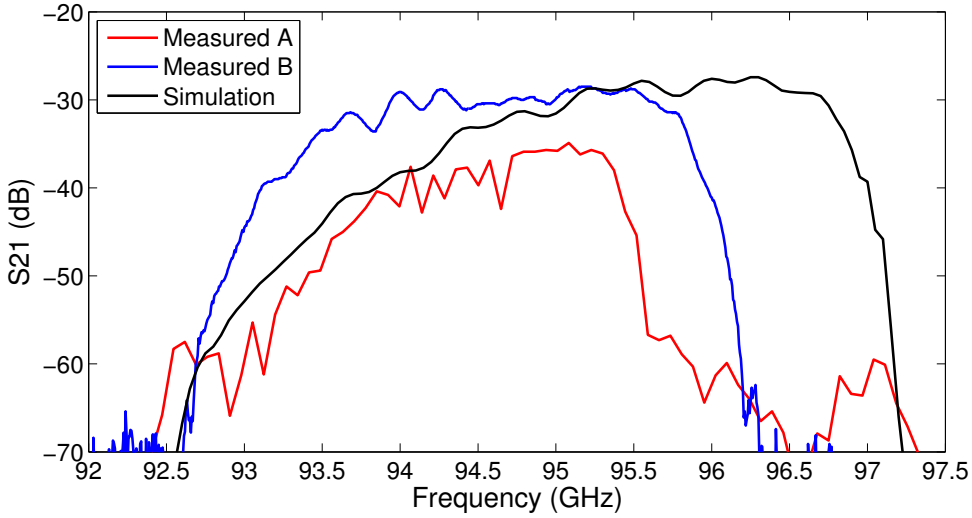

Figure 4-10: Transmission, S_{21}, measurements for the 87-cavity structures with dielectric loading as compared to calculated transmission from HFSS simulations for the TM_{31} mode.

well with theory. In addition, the cold circuit bandwidth for Structure A is 2 GHz less than the predicted bandwidth of the coupled-cavity circuit, and it is about 1.5 GHz less for Structure B. Structure A has more loss than predicted due to machining burrs incurring additional losses and reflections. Though the gain seen from Structure A will be less than predicted in Chapter 2, the structure has sufficient transmission to test the overmoded TWT.

Since Structure A had less transmission than anticipated, a second structure (B) was made to test the robustness of the machining process. The same specifications were used in machining Structures A and B, but Structure B was extensively cleaned and removed of machining anomalies (primarily consistent of small burrs on the dielectric slot edges). A direct comparison between the two structures is shown in Figure 4-11 without the dielectric loading installed. With the extensive cleaning, some improvements were noted: a significant increase in transmission (especially with the dielectric loading in place), more consistent transmission over the bandwidth, and about 500 MHz of bandwidth was recovered. In hot test, the gain seen in Structure B may agree better with theory, but it may still have a smaller bandwidth.

Overall, three TWT hot tests were performed. The S_{21} transmission measurements

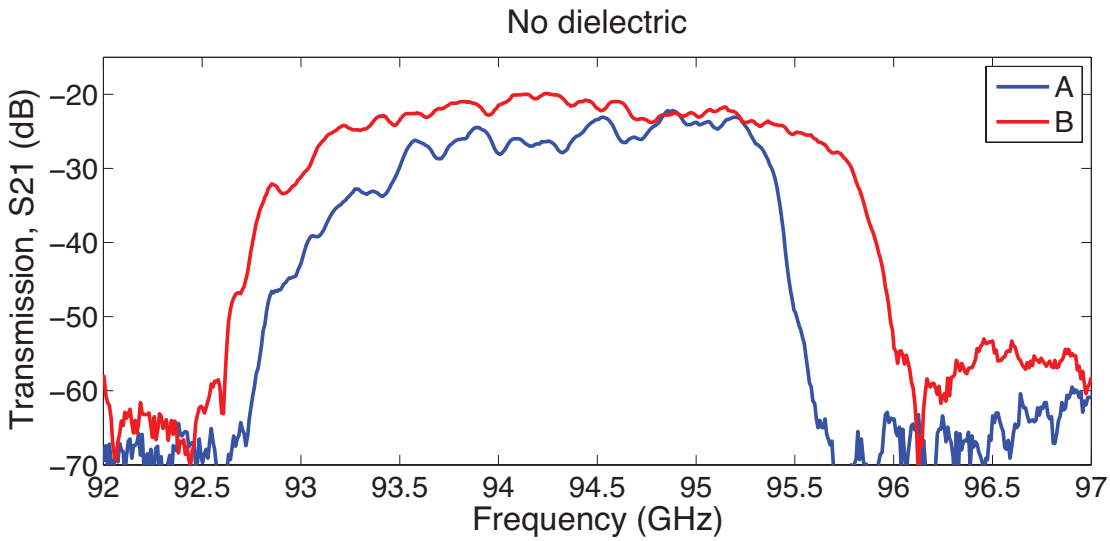

Figure 4-11: Transmission measurements for first and second 87-cavity structures with no dielectric loading installed. The second structure was extensively cleaned of machining burrs.

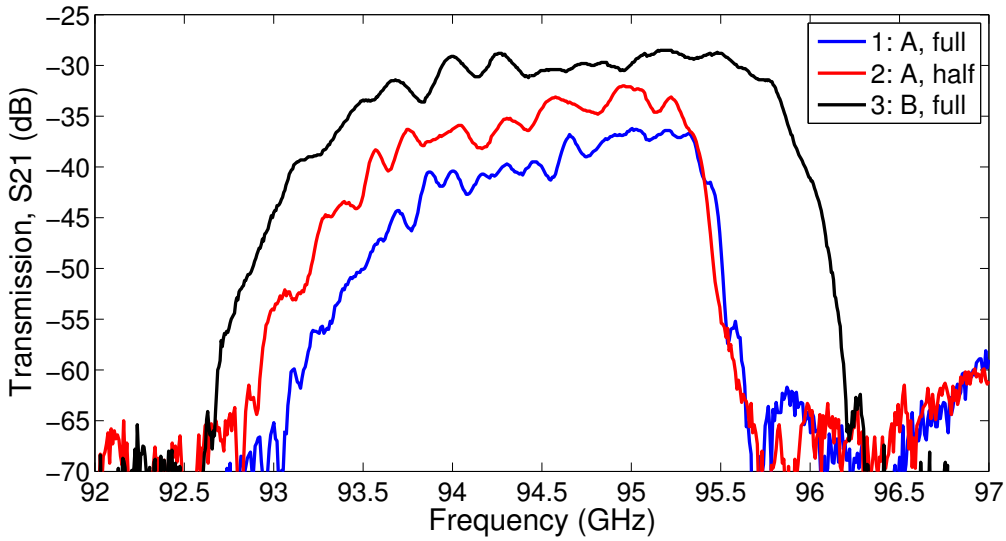

Figure 4-12: Transmission measurements for the assembled structures that underwent hot test: Structure A (full loading), Structure A (half loading), and Structure B (full loading).

for the TM_{31} mode of the three combinations tested is shown in Figure 4-12. First, Structure A was tested with full dielectric loading installed. "Full loading" means that the first 85 cavities of the structure were filled with dielectric, and the last two cavities were left without loading. This combination allows for slightly higher

gain without the possibility of inducing oscillations. Second, Structure A was tested with half of the dielectric loading installed; the first 40 cavities of the structure had dielectric loading, and the last 47 cavities were left with a vacuum gap where the loading would be. Third, Structure B was tested will full dielectric loading. The full experimental set-up will be described in Chapter 5, and the results from these three combinations under hot test will be described in Chapter 6.

Chapter 5

Experiment Design and Set-up

The overmoded TWT experiment was designed and built at MIT. Unless otherwise noted, all custom components were designed in-house and fabricated at the MIT Central Machine Shop. The design is made to be modular. It has a wide range of operation parameters, the test stand can be disassembled, and the TWT structure and RF components are replaceable. Due to its nature as a modular experimental design and the need for quick experimental turn-around times, it is not comparable to a commercial W-band TWT design in size or portability. However, the interaction structure within the experiment is of the same quality as its commercial counterparts.

5.1 Experiment Overview

An overview of the full laboratory set-up is shown in Figure 5-1. Here, the EIO driving source is shown; not shown is a low-power solid-state W-band source that will also be discussed and can easily replace the EIO. The solenoid magnet is displayed, and the electron gun is highlighted. Also shown is the transformer tank for the pulse modulator, which provides a high voltage pulse for the electron gun. All of these components, along with the RF windows and the safety interlock system, will be described in detail in further sections of this chapter.

The main component of the experiment is the vacuum tube which is placed inside of the solenoid magnet. Figure 5-2 is a CAD rendering which displays a cross-sectional

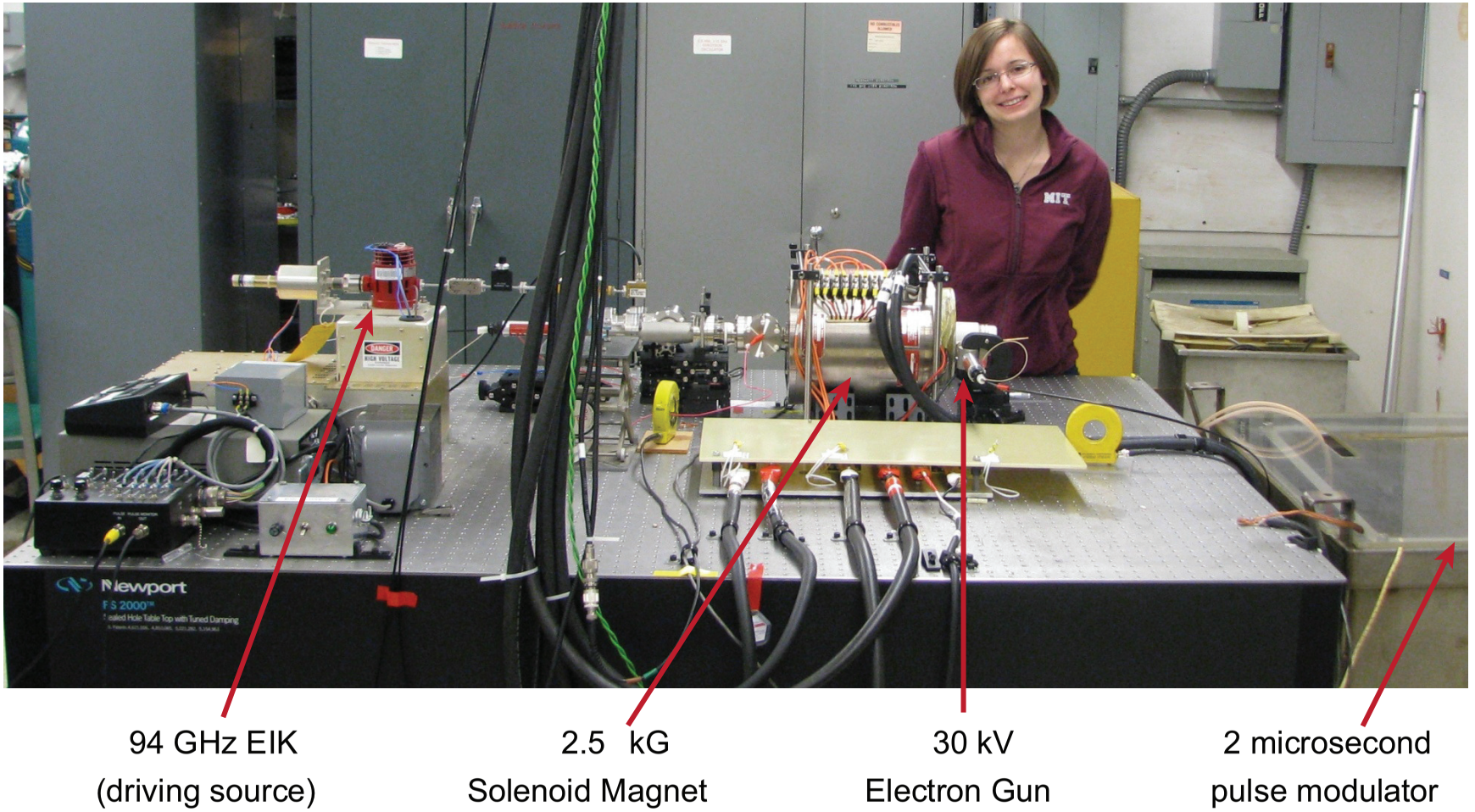

Figure 5-1: The full experimental set up, highlighting the EIO driving source, solenoid magnet, electron gun, and pulse modulator.

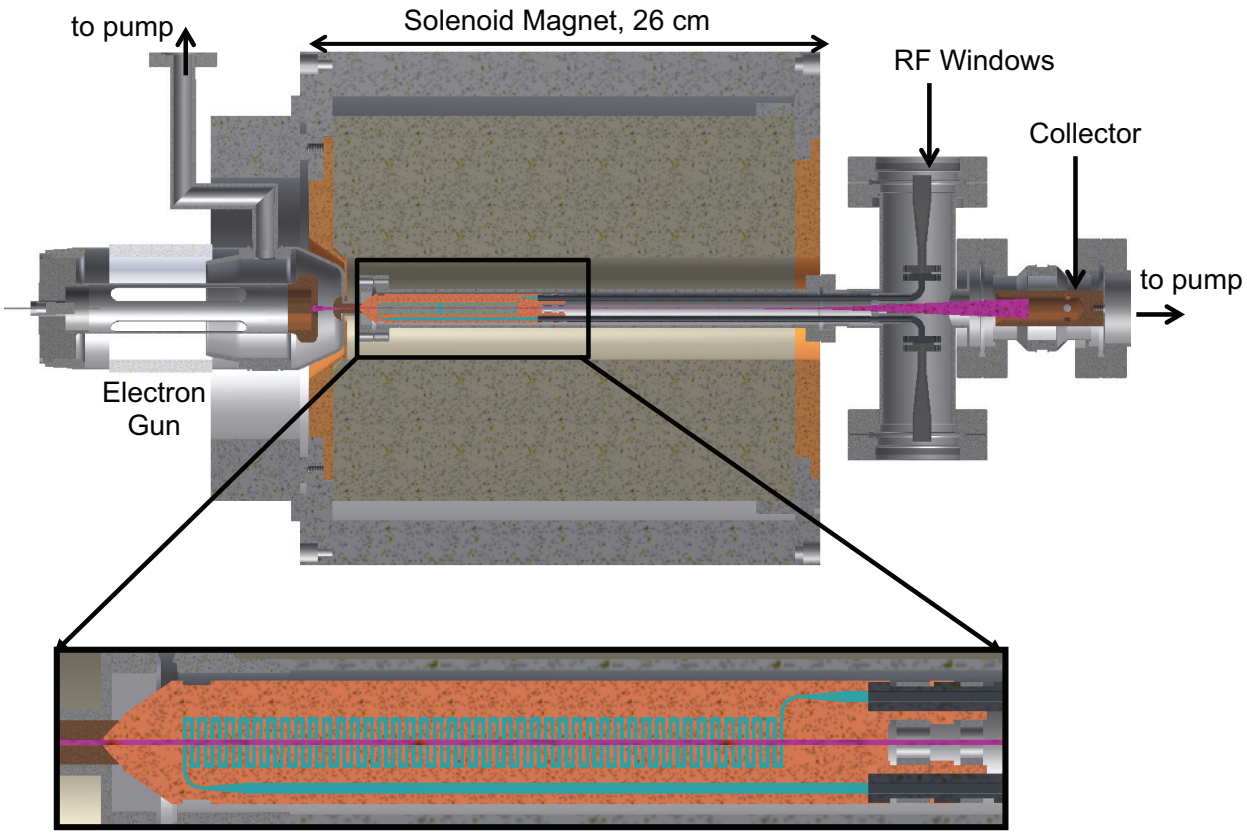

Figure 5-2: A rendering of the TWT tube assembly inside of the solenoid magnet. The cut-away highlights the TWT structure, where the coupled cavities have been colored cyan. The simulated electron beam trajectory is pink.

view of the TWT tube inside of the magnet. All assembly drawings and diagrams were made in Autodesk Inventor. In this figure, one can see how the electron gun, TWT structure, RF coupling, and collector are arranged inside of the tube. This tube is designed such that it must be assembled around the solenoid magnet. The simulated worst-case electron beam is shown in pink in the drawing. There are two 3-way translation stages on either side of the magnet (not shown) in order to finely adjust the position of the tube. The x- and y-adjustments on the electron gun (high voltage) side of the magnet are remotely controlled so that alignment can be performed while under operation.

Of particular note with the tube design is the TWT structure placement, which is highlighted in Figure 5-2. Four screws hold the alignment surface of the structure onto the anode of the electron gun. This alignment ensures a solid mating between

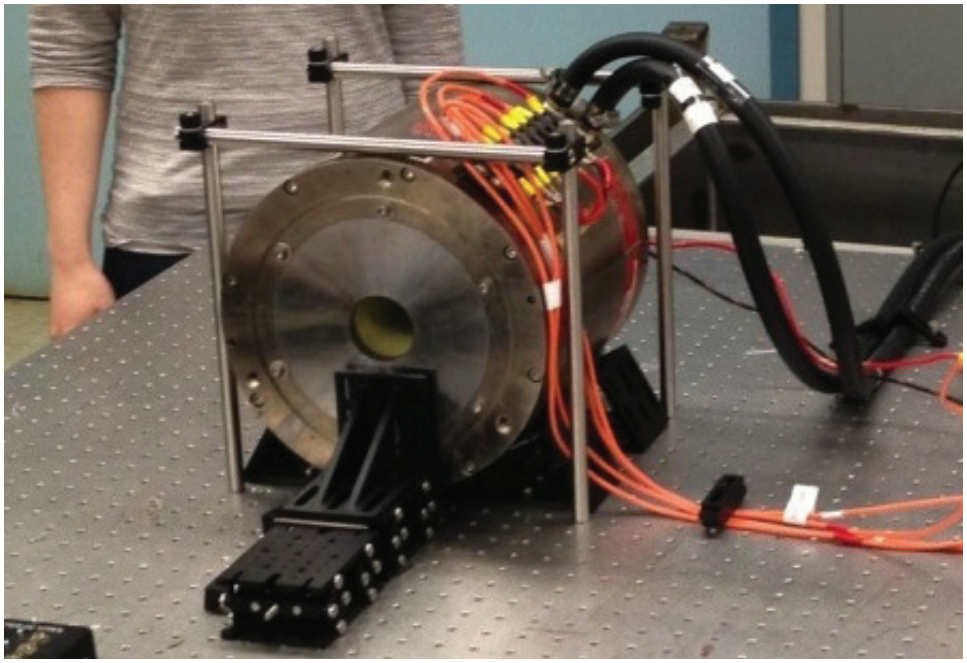

Figure 5-3: The 2.5 kG solenoid magnet installed on the experimental optical table for testing. The collector-side iron pole piece can be seen. The magnet is water-cooled.

the center-lines of the electron gun and structure, which is critical for operation. The structure was made to be modular. Any other structure with the correct mating surface can replace the TWT structure that is currently in place. This easy switching of components allows for a quick turn-around time between experimental tests.

5.2 Solenoid Magnet

The solenoid electromagnet used in this experiment is a 2.5 kG, four-coil electromagnet. Shown in Figure 5-3, the magnet is a wire-wound magnet from Arnold Magnet Technologies (Ogallala Electronic Division) and purchased from Varian Associates; it was previously used for a Pierce wiggler gun experiment [8]. The magnet is water-cooled with copper tubing installed around the solenoid windings. The four coils are each individually controllable, allowing for variable magnetic field shaping. The solenoid magnet can provide up to 3 kG peak field and is nominally operated at 2.5 kG peak field. With appropriate drive currents on the four coils, the flat-top of the magnet is 10 cm long. For convenience, the two inner coils of the magnet are

connected in series to a power supply, and the two outer coils are also connected in series to a power supply. TDK Lambda GEN40-85-3P230 3 kW power supplies are used, offering precision control for the current and voltage applied to the magnet. If necessary, the four coils can be controlled individually by separate power supplies.

A small solenoid electromagnet is installed on the electron gun side of the magnet, to be used as a gun coil. The gun coil is able to provide a magnetic field up to 260 G to help shape the field at the location of the electron gun. The gun coil is controlled with a TDK Lambda GENH20-38-U 750 W power supply which offers precision control.

An iron pole piece was designed for the magnet in tandem with the electron gun design. The iron pole piece provides a sharp rise in the magnetic field which works with the electrostatic focusing of the anode-cathode configuration in order to provide a high compression electron gun. A back pole piece was also implemented on the collector side of the magnet in order to control the electron beam expansion as it exits the magnetic field.

The code Poisson was used for calculations and design of pole pieces to shape the magnetic field. Poisson/Superfish is a 2-D Poisson's equation solver distributed by the Los Alamos Accelerator Code Group at Los Alamos National Lab. Superfish is an electromagnetic field solver often used for designing accelerator cavity structures [4]. The solenoid magnet with the gun coil and iron pole piece was calculated as a magnetostatic problem with ferrous materials. The pole piece was designed in tandem with the electron gun in order to provide the appropriate beam shaping. The final geometry of the pole piece from the Poisson simulation is shown in Figure 5-4, along with the calculated magnetic field lines. The main coils of the solenoid are outlined in green, and the gun coil is also shown in the geometry.

In the geometry for the Poisson simulation, the iron pole piece appears to be complicated. In reality, this complicated design was modified from the original, much simpler, design. Unfortunately, when manufacturing considerations had to be taken into account, the simpler design was not physically realizable since it needed to exist in the same physical location as the anode. That is, the pole piece had to be shaped around the electron gun geometry, while also allowing room for adjustments and

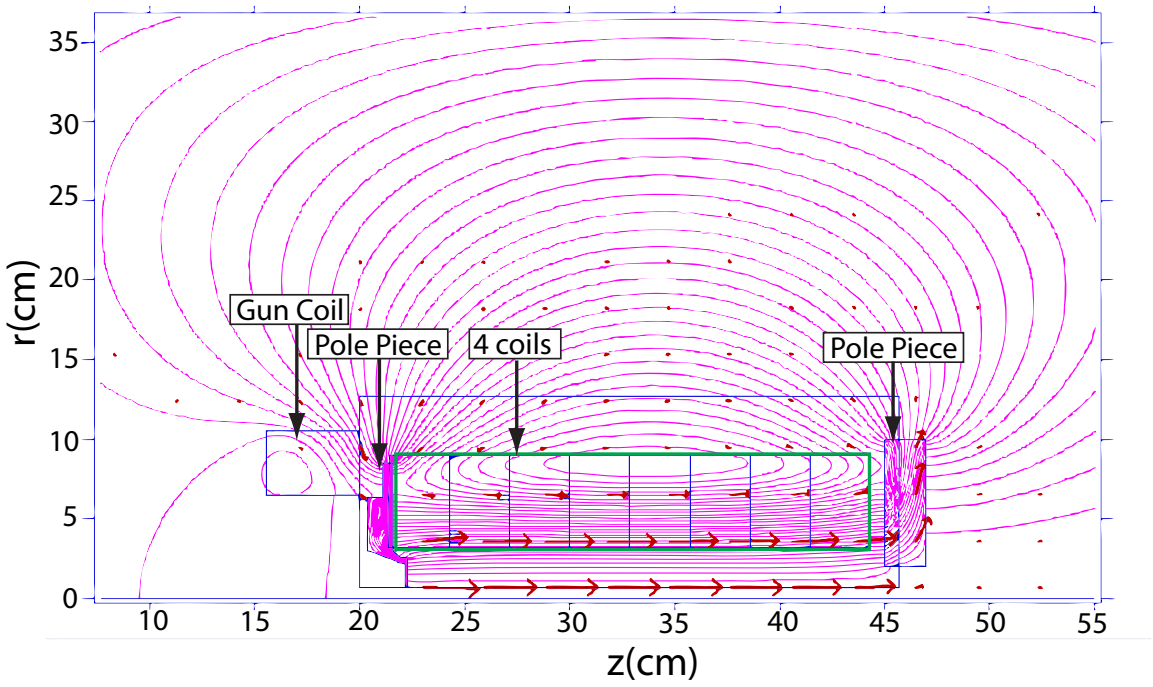

Figure 5-4: Poisson calculation of the solenoid electromagnet with the gun coil and pole pieces. Magnetic field lines are shown in pink and magnetic field vectors are marked in red.

alignments that would be necessary in the final implementation of the system. These requirements led to the tapered design of the iron pole piece.

The magnetic field was measured prior to installation of the TWT test stand with a 1-D Hall probe. Experimental measurements of the magnetic field are shown in Figure 5-5. The measurements for 1.8 kG operation are shown, and agree very well with Poisson calculations. The electron gun was designed to have optimized performance at this magnetic field. This conservative point of ideal operation will allow for adjustments to be made in the magnetic field. That is, a higher field can be obtained if it is found necessary under non-ideal experimental conditions. These adjustments will allow of optimizing the performance of the TWT.

Between two stages of experimentation, the magnetic field was re-measured with a 3-D Hall probe. Azimuthal measurements around the center of the magnetic bore indicated a small, 2.5 ± 0.5 mm, misalignment between the magnetic field axis and the cylindrical bore center at 55 degrees from the top of the magnet. This misalignment was fixed by re-machining the iron pole piece to have a larger inner hole that could

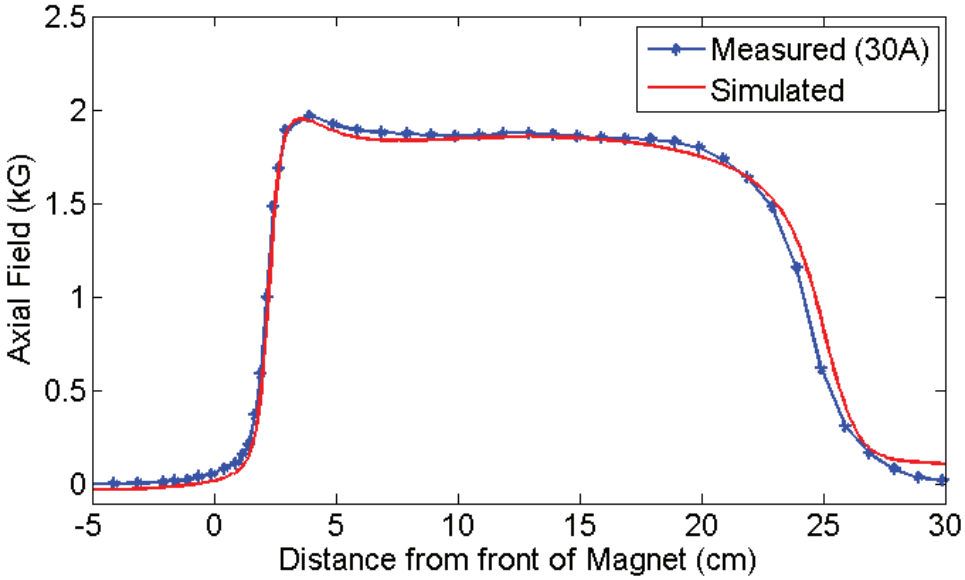

Figure 5-5: Measurement of the $\hat{z}$-directed solenoid magnetic field with the iron pole pieces and gun coils installed and operating at 1.8 kG (30 A driving current on each coil), with comparison to Poisson simulations.

be centered on the magnetic axis (instead of being centered on the bore). This adjustment allowed for the tube to be aligned to the magnetic axis, allowing for better beam formation in the electron gun. The on-axis axial magnetic field changed by less than 10 G with the new pole piece. The effect of the iron pole piece adjustments and tube alignment to the magnetic axis will be discussed further in Chapter 6.

5.3 Electron Gun

The Pierce electron gun for the TWT was designed and built at MIT. The TWT was designed to operate with a 31 kV, 310 mA electron beam. The electron beam diameter must be less than the beam tunnel diameter, 0.8 mm, and was designed to be no more than 0.6 mm in the ideal case. Minimal axial velocity and beam scalloping was required for ideal operation of the TWT.

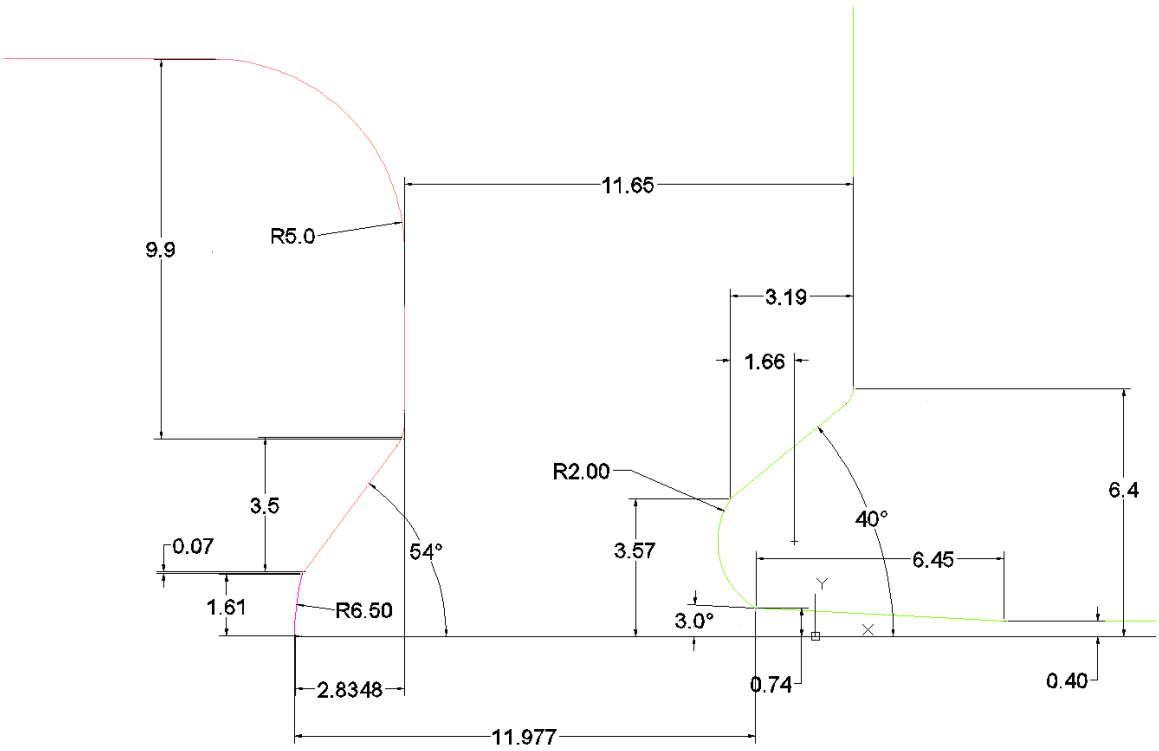

Figure 5-6: The 2-D cylindrical electron gun geometry (units in mm). The cathode consists of the emitter surface (pink) and the focus electrode (red). The anode and beam tunnel (green) are kept at ground potential. The black line indicates the rotational axis.

5.3.1 Design

The design was completed in Leidos (formerly SAIC) Michelle, an electron gun modeling software [54]. The geometry of the focus electrode, emitter cathode, and anode were modeled in 2-D for simplicity. Though, 3-D simulations were possible to detect alignment and manufacturing tolerances. Michelle calculates the emitted electron beam and transportation of the beam through the anode and beam tunnel with an external magnetic field applied. The axial magnetic field was calculated in Poisson and was used in the design of the electron gun.

Through an iterative design process, a Pierce electron gun was designed to meet the parameters of the experiment. The final parameters of the cathode and anode are shown in Figure 5-6, which displays the design in cylindrical coordinates. The emitter surface is a 3.2 mm diameter spherical cap, and the focus electrode is 54° from

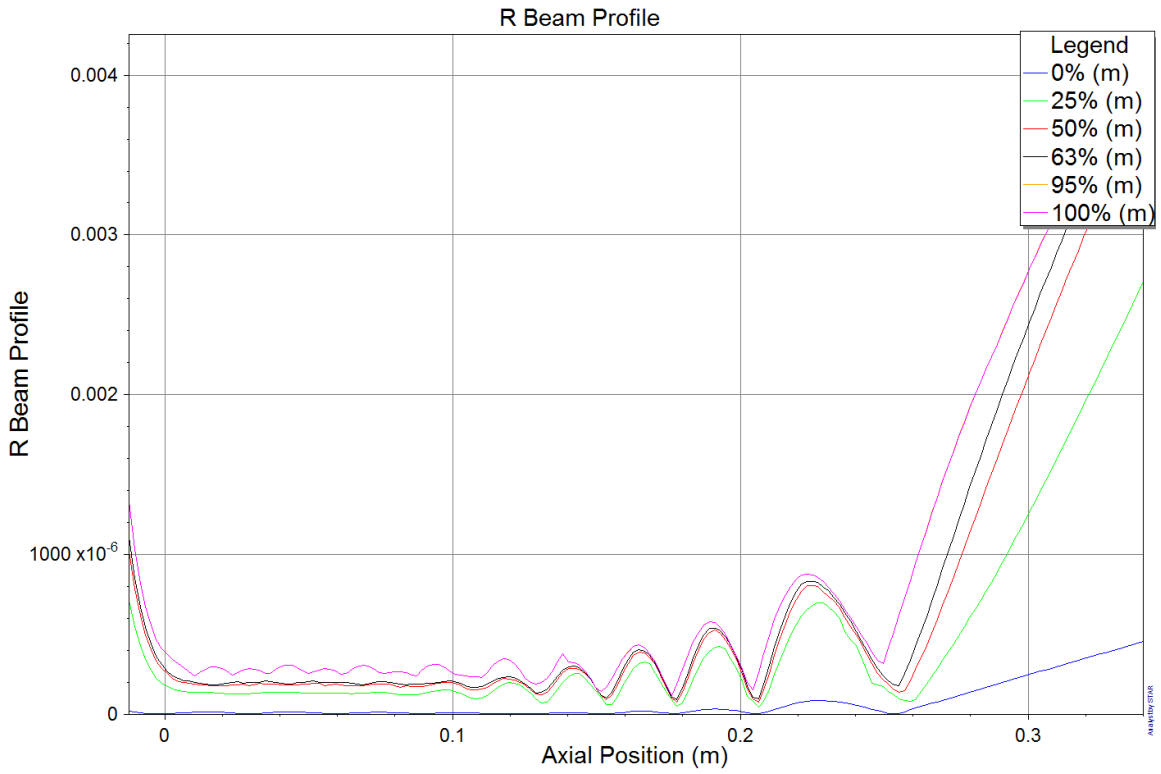

Figure 5-7: The beam envelope calculated via Michelle for 1.8 kG flat-top magnetic field. The axial position $z = 0$ is marked as the coordinate axis in Figure 5-6 and physically corresponds to the front surface of the magnet.

the center-line. The distance between the anode and cathode is nearly 12 cm. This distance allows for a high compression beam with minimal scalloping to be formed. Not shown in the picture is the anode extending to a 30 kV ceramic standoff, which connects to the cathode and provides vacuum.

During space-charge limited operation at 31 kV, 320 mA was emitted from the cathode. The cathode emitter has less than 5 A/cm^2 current density on its surface during space-charge limited operation. The electron beam profile which results when a magnetic field of 1.8 kG is applied is shown in Figure 5-7. In the beam tunnel, the electron beam is less than 0.5 mm in diameter under ideal conditions. When the magnetic field was adjusted to a slightly higher value for safe operation, minimal scalloping kept the beam diameter to be less than 0.6 mm in diameter. The beam is confined for the duration of the flat-top field (from 1–10 cm). After exiting the beam tunnel, the beam expands, which allows energy to dissipate when it deposits onto the

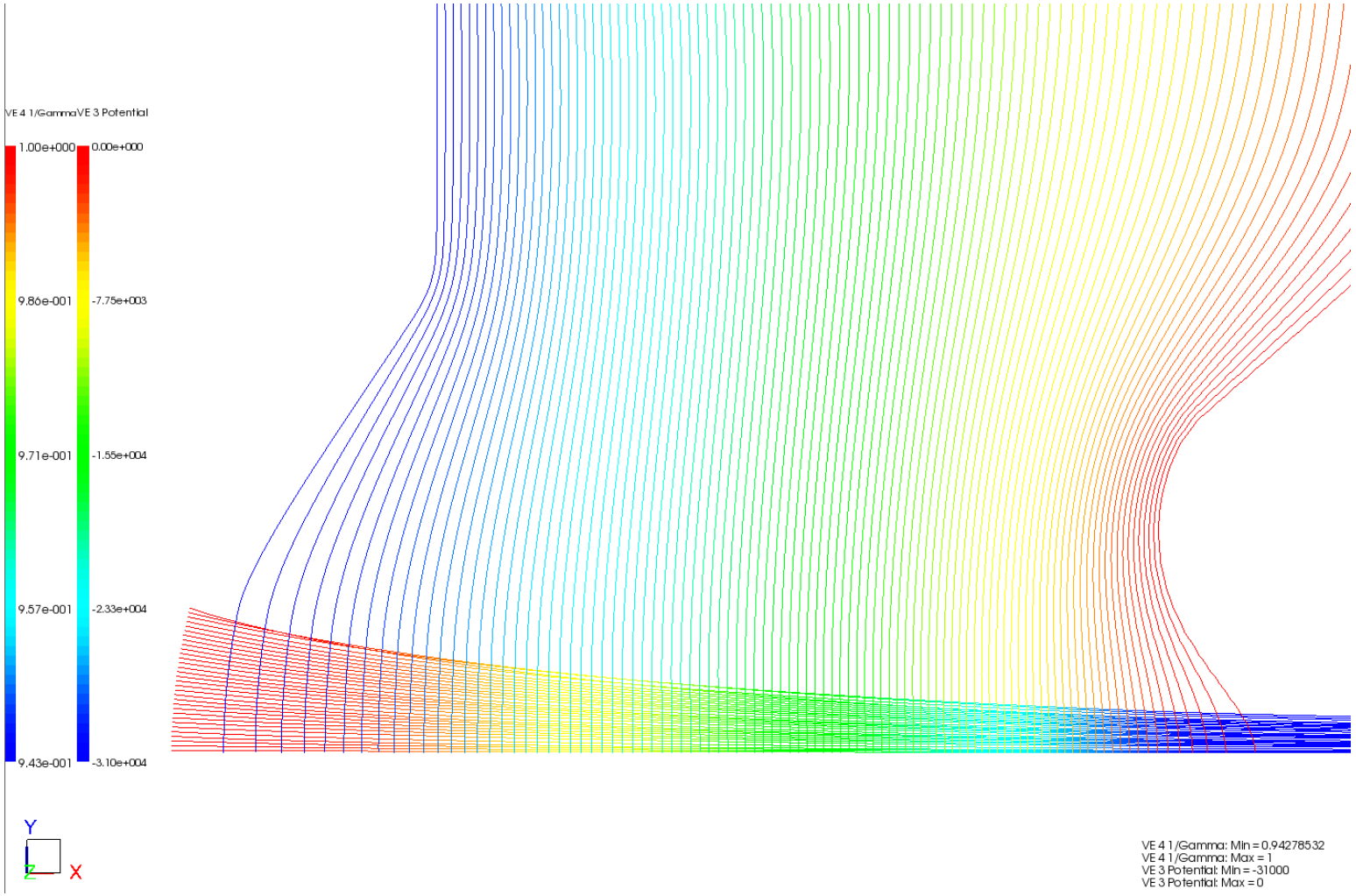

Figure 5-8: The equipotential lines and particle trajectories as calculated by Michelle for the 30 kV electron gun. The cathode emitter surface is on the left, where the particles originate. The figure is truncated at the right, where the beam enters the beam tunnel.

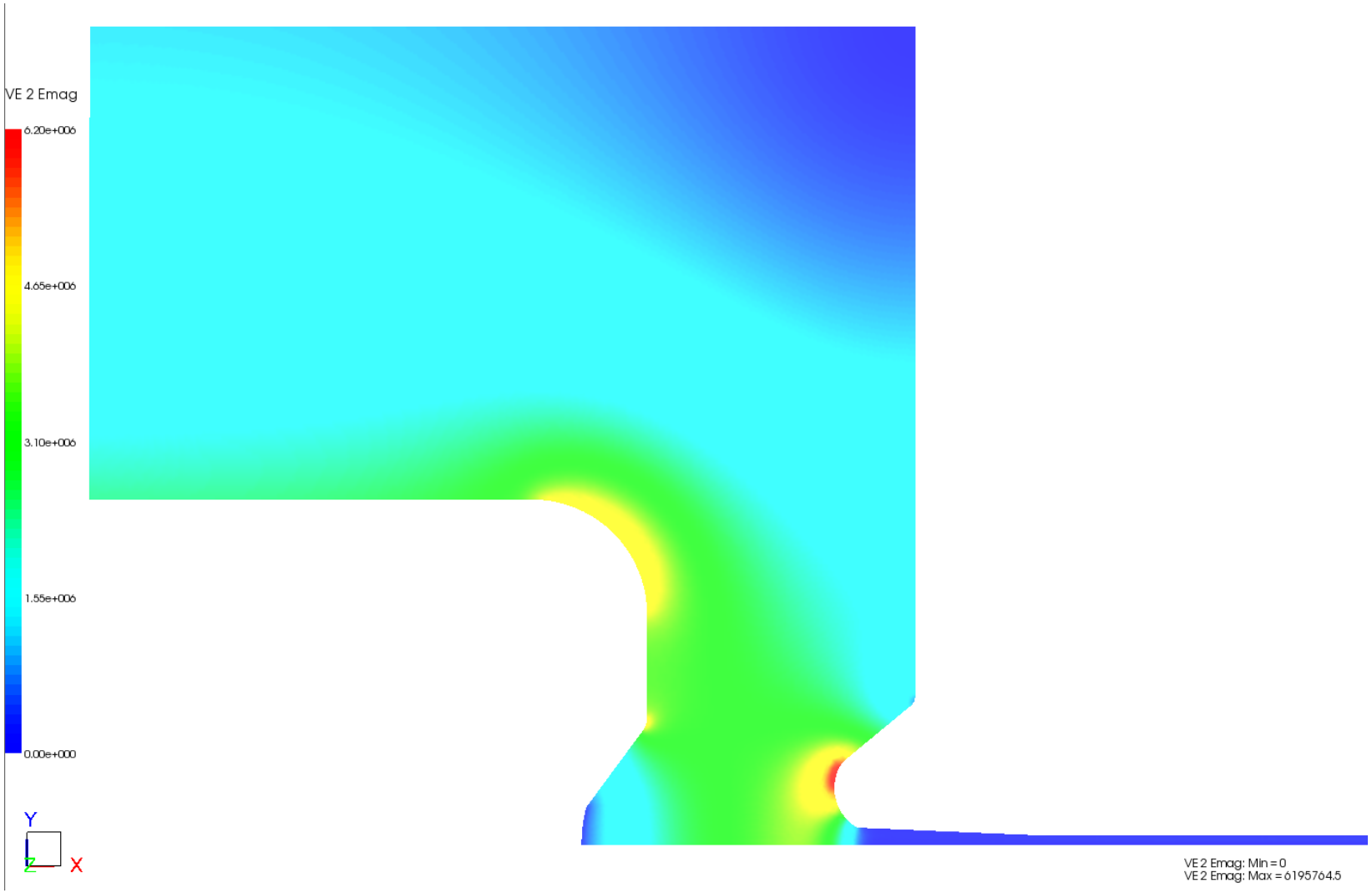

Figure 5-9: The electric field in the electron gun for operation at 31 kV as calculated in Michelle. The peak electric field occurs on the anode surface. The beam tunnel is truncated on the right to emphasize the electric fields within the region of the A-K gap.

collector. Adjusting for experimental operation and machining tolerances, 310 mA of current was expected from the cathode.

Figure 5-8 shows the equipotential field lines between the anode and cathode for the given geometry. In addition, the electron particles simulated are shown coming off of the emitter surface, gaining energy in the A-K gap, and entering the beam tunnel; minimal crossover is seen between the particles, showing that minimal axial velocity is present in the simulation. Keep in mind that this simulation is for the ideal case of alignment between the cathode, anode, beam tunnel, and magnetic axis; any misalignment in those components will cause an axial velocity to form. For simplicity, we have estimated there to be 1 % axial velocity spread for the TWT simulations that were referenced in Chapter 3.

The magnitude of the electric field for the electron gun operating at 31 kV is shown in Figure 5-9. The peak electric field occurs on the anode surface, 62 kV/cm, which is low enough for safe operation during vacuum. The design goal was to keep the electric field below 80 kV/cm. At all other surfaces, the electric field is kept reasonably low.

5.3.2 Manufacturing

After design, dimensions were scaled to account for thermal expansion during hot cathode operation. A CAD cross-section of the final design of the electron gun is shown in Figure 5-10. A 1 kV feed-through leads to the heating element on the cathode emitter, which heats up to 1200 °C. The cold cathode has a resistance of 1 Ω, and the fully heated cathode has a resistance less than 5 Ω. The heater power should not exceed 8.5 W for safe operation. A standard 30 kV ceramic standoff was used, and the design is able to withstand up to 35 kV operation safely.

Figure 5-10 highlights the pole piece and anode configuration of the electron gun. The pole piece is machined in two parts and is installed around the electron gun; the inner radius of the pole piece limits the size of the tube in that area. For vacuum, the anode creates a bad pumping conductance between the electron gun and collector

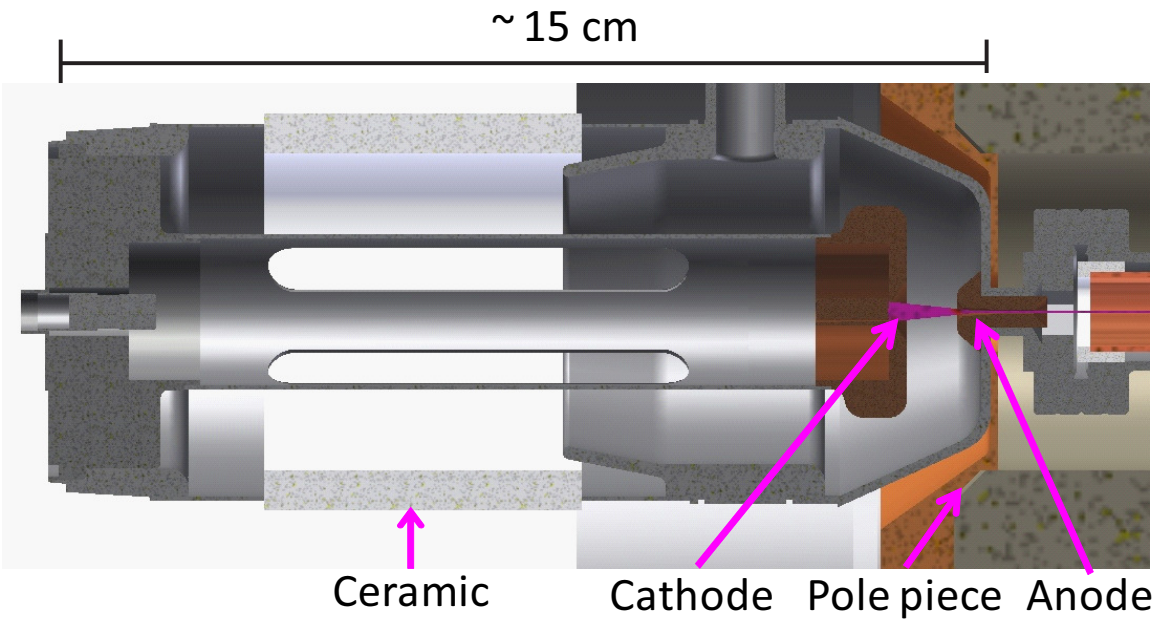

Figure 5-10: A cross-sectional view of the electron gun modeled in Autodesk Inventor with cold dimensions.

sides of the tube. For reference, conductance, C, can be calculated through a pipe as

$$C = 75D^3/L \text{ [L/s]} \tag{5.1}$$

where D is diameter and L is length of the pipe (in inches) [15]. So, the small diameter of the anode and the beam tunnel leads to a small conductance between the electron gun and collector sides of the tube. The mechanical design could be modified to increase this conductance in this region, however both sides of the tube are connected to 2 L/s ion pumps, which provide adequate pumping speed for the entire device. The dual pump approach prevents the need for additional conductance to be added around the iron pole piece.

The electron gun was made with 1–10 mil tolerances, as necessary, and precise alignment between the anode and cathode was achieved. The machined cathode and anode are shown in Figure 5-11. Prior to final assembly, the final welding joint was machined for accurate alignment and separation between the anode and cathode.

The electron gun components were machined at the MIT Central Machine Shop, with exception of the the heating element and cathode emitter, which was manufac-

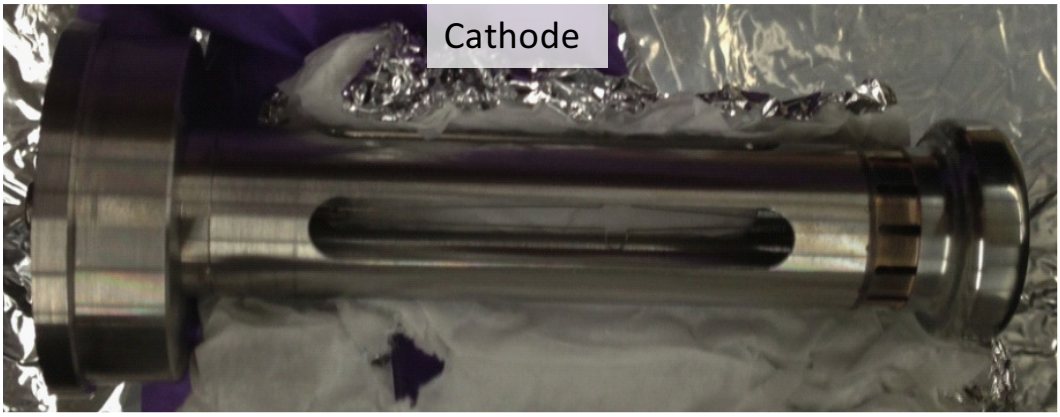

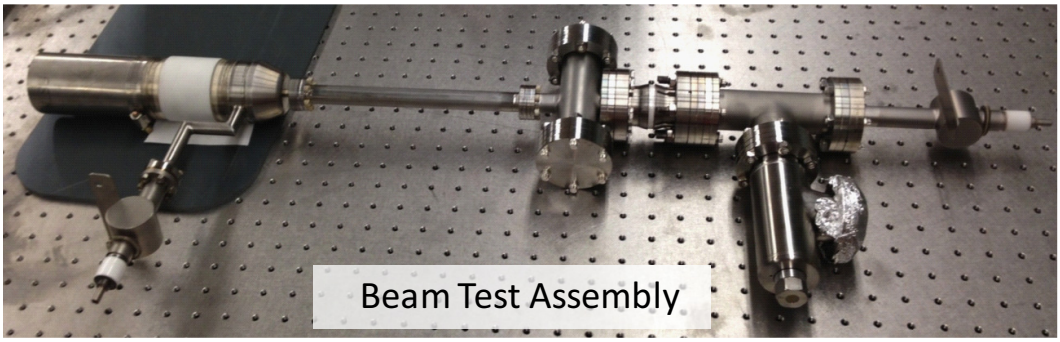

Figure 5-11: The cathode and anode prior to final welding of the electron gun. Also shown is the beam test assembly, where the assembled electron gun is visible on the left, with an ion pump attached.

tured by Heatwave Labs. The cathode used was modified from a standard dispenser cathode, model STD 134 [29]. A precision spot weld secures the cathode stalk to the base assembly. The copper anode was brazed onto the stainless steel surrounding structure, while all other joints were welded. Figure 5-11 also shows the electron gun after final welding when it was installed onto the entire tube assembly, which shows the electron gun ceramic stand-off and ion pumps. The tube assembly shown was baked at 150 °C prior to being installed in the solenoid magnet. This assembly was used to test the quality of the electron beam produced by the gun. Results from the beam test will be shown in Chapter 6.

Of final note on the machining of the electron gun is cooling considerations. The electron gun is air-cooled since the cathode is small and the power required to heat it is, at maximum, 8 W. The cathode stalk was machined for minimal expansion and for heat dissipation. A moderate air-flow is maintained around the electron gun during heating and operation.

5.4 Driving Sources

Two different W-band sources will be used to drive the TWT Amplifier circuit. For the circuit, at least 10 dBm of power is required to detect amplification. A low-power bandwidth of 10 GHz (90–100 GHz) will be needed for bandwidth measurements. In order to saturate the circuit in ideal conditions, at least 300 mW of power at 94 GHz is needed. Due to these broad necessities in testing, two sources will be used: A high power extended interaction oscillator (EIO) and a broad bandwidth solid-state active multiplier chain (AMC).

5.4.1 94 GHz EIO

For the high power source, an EIO manufactured by CPI Canada was used. It is shown in Figure 5-12. The output of the EIO is in W-band waveguide, WR-10. In the picture it is shown connected to an isolator, two variable attenuators, and a detector diode, since power measurements of the EIO were being performed at the

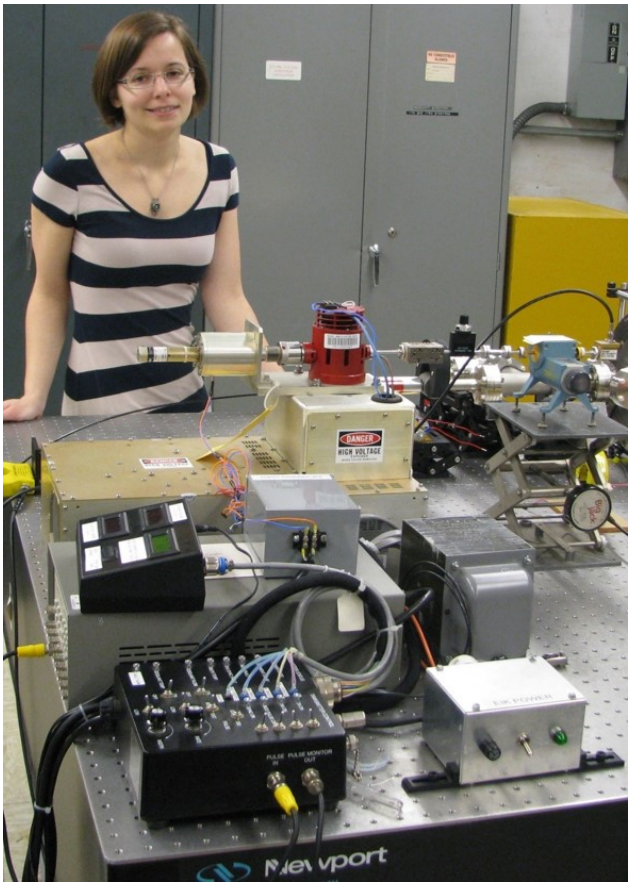

Figure 5-12: A picture of the 94 GHz EIO in the laboratory with an isolator and attenuation on the output.

time. The EIO is capable of producing more than 300 W of power between 93.5 and 95.7 GHz. The frequency is manually tunable via a motor controller. It is able to provide 1–5 microsecond pulses at a rate of 1 Hz, which matches well with our experimental requirements.

The EIO offers the advantage of an extremely high input power. This will allow the circuit to reach saturation while under testing. It is also useful in finding operation points when under initial testing of the TWT, since more power can be used in detection of small amplification parameters. Unfortunately, the EIO has a small bandwidth, and it not easily or consistently tunable to a certain frequency; leaving it difficult to measure gain-bandwidth characteristics.

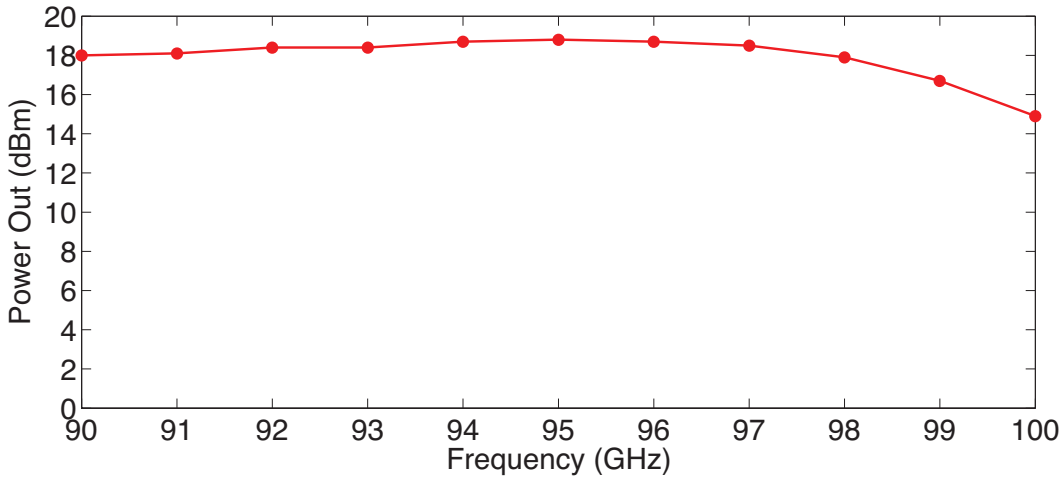

Figure 5-13: Frequency vs. power for the Millitech AMC.

5.4.2 W-band Solid-State AMC

The broad bandwidth, solid-state Active Multiplier Chain (AMC) used for this experiment was purchased from Millitech. The AMC-10-RNHBO is a 6-times multiplier used in tandem with a 3 dBm, 15-17 GHz CW frequency generator. The AMC can provide at least 15 dBm of power (32 mW) between 90-100 GHz, as shown in Figure 5-13.

The AMC is useful in providing a source that is highly tunable in frequency over a broad bandwidth. Unfortunately, it provides a relatively small amount of power to the amplifier circuit when compared to the EIO. The AMC is not powerful enough to drive the circuit into saturation under the expected operating conditions.

For these reasons, a combination of the two sources was used in the amplifier experiment. The low power AMC was used to find low power linear gain and gain-bandwidth characteristics of the TWT. The high power EIO was used to initially optimize the circuit (via tuning of positions and operation parameters of the TWT) and to find high power gain and saturation characteristics of the TWT amplifier circuit.

5.5 RF Vacuum Windows

RF windows are necessary for input and output coupling into the TWT circuit, under vacuum. There are two possible ways to go about the window design. The simplest, though most expensive route, would be to use WR-10 waveguide RF windows that have been specifically designed for 94 GHz. This is the standard approach used in TWT industry, and improvements on W-band windows are still under development [32] [72]. Unfortunately, engineering to industry standards while maintaining a TWT tube that has an interchangeable circuit is prohibitive. In addition, transmission of the fundamental mode in the circuit at 62 GHz must also be considered; though the mode should not be present, this TWT is being built to verify that prediction, so a very narrow-bandwidth window could be prohibitive to our testing. Therefore, windows fitted in WR-10 waveguide and tuned to 94 GHz were not used. The alternative option for windows is to use over-sized windows that are fit to a standard conflat flange; these windows work well with the interchangeable circuit and modular TWT design and can be manufactured to a specified width such that they will not have high reflection at the 62 GHz fundamental mode while maintaining good transmission at 94 GHz.

The windows used in this experiment are standard windows from MPF Products, a company that specializes in ceramic-metal brazing and vacuum components. The windows are fused silica (SiO_2) that has been brazed onto a conflat flange. The width of the silica has been chosen to have a transmission resonance at 94 GHz. This is calculated via the simple 2-boundary dielectric problem, where a dielectric slab is considered, the transmission, T can be calculated as

$$T = \frac{(1-R)^2}{(1-R)^2 + 4R\sin(\delta/2)^2} \tag{5.2}$$

with

$$\delta = \frac{2\omega n}{c}\cos\theta w \tag{5.3}$$

[40] [26] where θ is the incident angle (in this case, we assume normal incidence,

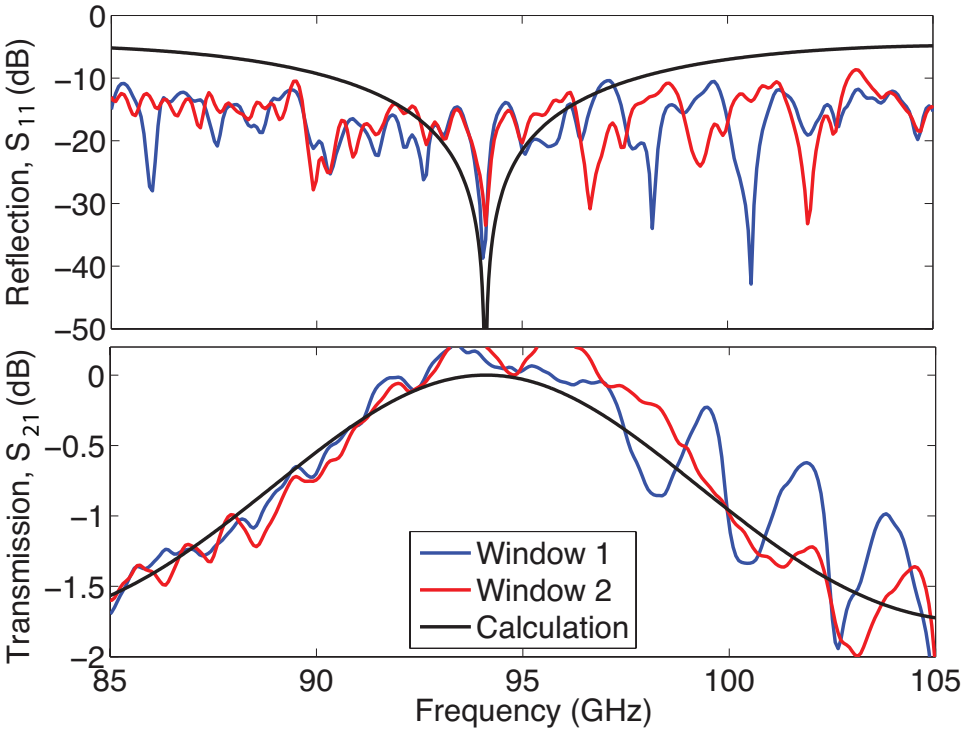

Figure 5-14: Measured and calculated transmission through the fused silica RF windows.

$\theta = 0$), R is the reflection of the material on a single interface, and the relative index of refraction for silica is $n_r = n/n_0 = 1.955$ in the W-band [13]. The width of the window, w is calculated such that the $T = 1$ at 94 GHz ($\omega = 2\pi 94 \times 10^9$ rad/s). There are multiple solutions to the equation. A window width of $w = 3.26$ mm (precisely measured as 0.1284±0.0005 inches) was chosen because a standard part at that width was available from MPF Products and fit our purposes. The calculated and measured S-parameters are shown in Figure 5-14, and show good agreement, assuming $R = 0.1$. The windows have a resonance at the design frequency of 94 GHz, and show good transmission at that point. A reflection is evident in the measurement due to the resonances in the coupling waveguides. There is more than -0.01 dB transmission from 92–97 GHz.

For the internal waveguide that couples into the TWT circuit, the WR-10 waveguide was tapered to WR-28 waveguide prior to transmission through the window, as can be seen in Figure 5-15. This allows for cleaner transmission through the fused

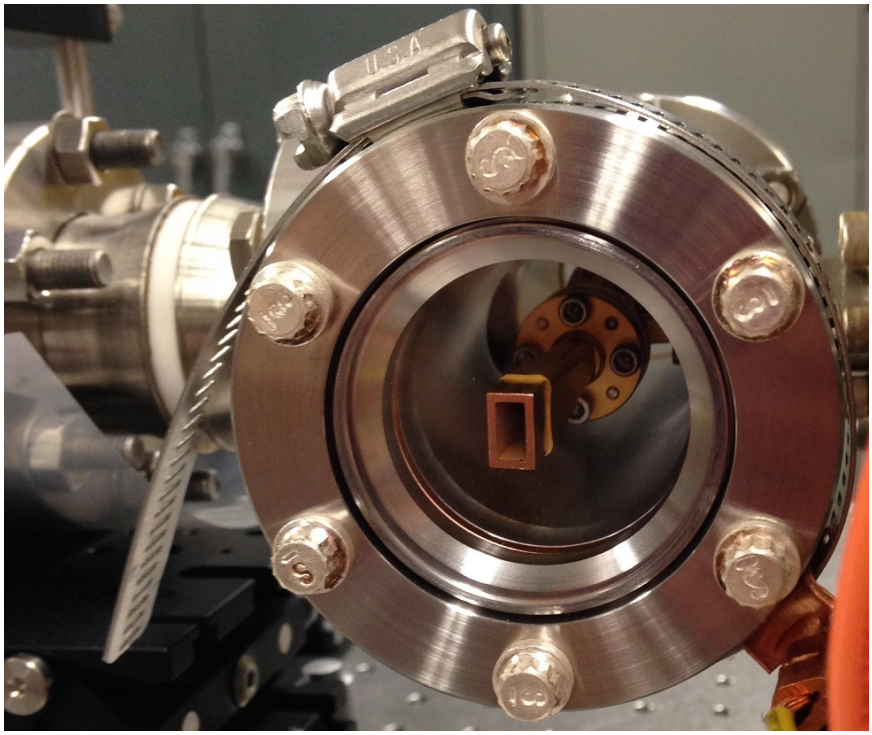

Figure 5-15: One of the fused silica RF windows in a 2-3/4 con flat flange, installed on the TWT. The input WR-28 waveguide can be seen

silica window due to easier alignment of the waveguides, and less overall power loss in the device. Outside of the window, a matched WR-28 to WR-10 waveguide taper is used to couple in power from a driving source at the input. At the output, the transition couples power to a diode to measure the output power from the TWT. These tapers have the potential to set up a resonance in the device, leading to 1–2 dB of trapped power losses. However, the transmission improvements seen when using this tapered section were greater than the detriments of trapped power losses.

5.6 High Power Pulse Modulator

The high power modulator and pulse forming network (PFN) was built in-house. It is powered via a thyratron and can provide 2.8 microsecond pulses at a rate up to 2 Hz. The peak voltage of the pulse can be set anywhere between 3 kV to 100 kV.

A block-diagram showing the high power PFN set-up is shown in Figure 5-16. The modulator is able to provide a high voltage pulse to one of the two experiments

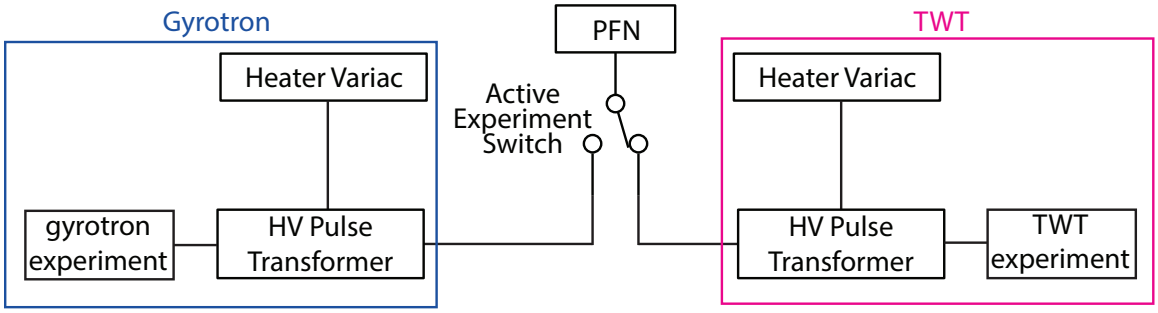

Figure 5-16: A block-diagram of the PFN and high voltage pulse transformer set-up with dual-experiment access.

that share the same laboratory space: either the TWT discussed in this thesis or a megawatt-class 110 GHz gyrotron [67]. The active experiment switch, thyratron, and capacitor bank are located in the control rack (see next section), and are shown in Figure 5-17. The thyratron triggers a 2.8 microsecond pulse from the capacitor bank at a rate set by the experiment controls. These components are all shared between the two experiments, but switch-over of operation between experiments can be done extremely quickly.

Each experiment has a separate pulse transformer network which is located in an oil tank near the respective experiment's electron gun. This set-up isolates the high voltage areas of the laboratory. An electrical drawing of the pulse transformer and connections to the experiment is shown in Figure 5-18, which highlights the high voltage isolation transformer and the load resistor to the experiment. The low-resistance load ensures matched operation of the PFN and a square pulse for the operation parameters of each respective experiment. An isolated 10,000:1 voltage divider (not shown) measures the operation voltage safely, so that the high voltage pulse can be monitored on an oscilloscope. The heater power is also supplied through this network via another isolation transformer which carries the AC heater signal on top of the high voltage pulse. A variable AC transformer (Variac) controls the power level of the AC heater signal, which is limited to 12 W for safety. The cathode heater power should not exceed 8.5 W under normal operation.

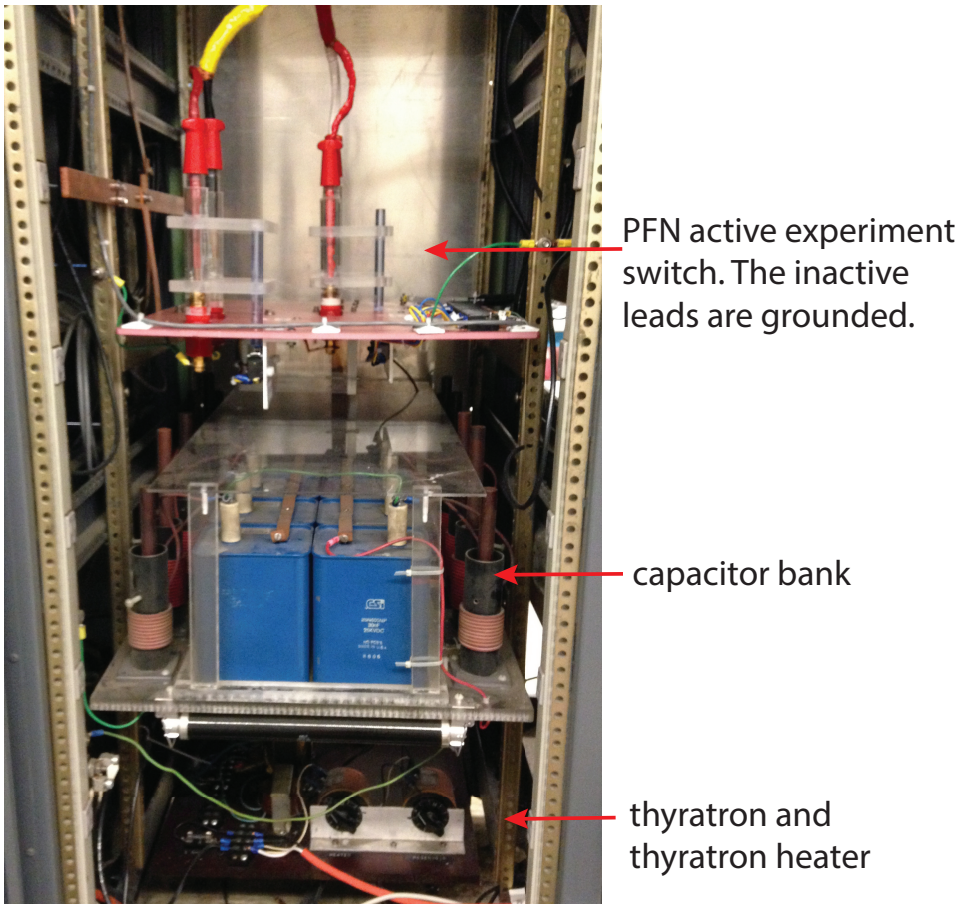

Figure 5-17: The modulator set-up, showing the high-voltage active experiment switch between the megawatt-class gyrotron and TWT experiments, the PFN capacitor bank, and the thyratron.

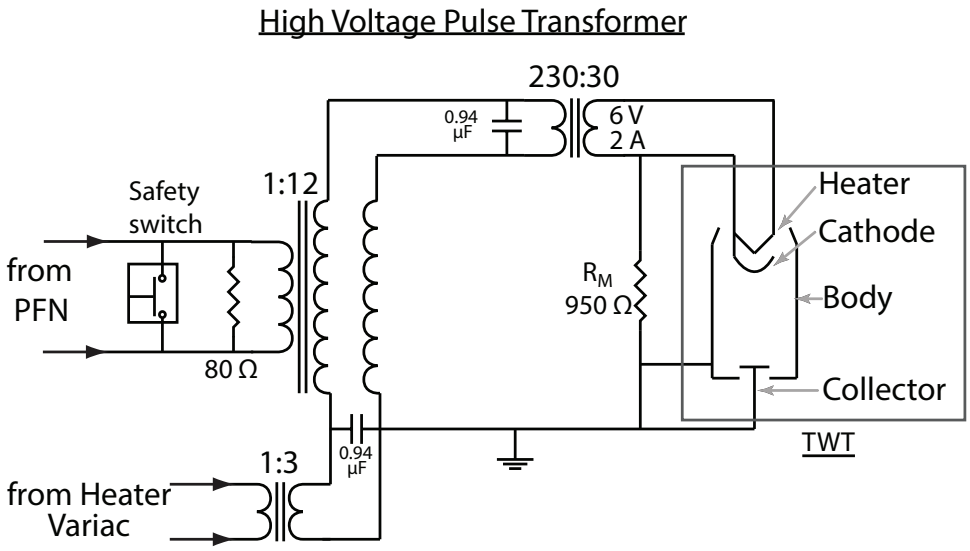

Figure 5-18: An electronic schematic of the high voltage pulse transformer and connections to the TWT experiment. The safety switch, a high voltage crowbar switch, is only energized and open when all safety interlocks are satisfied.

5.7 Safety Interlock System and Controls

The controls for the experiment along with the Safety Interlock System are shown in Figure 5-19. In the left rack is the cathode heater, along with a calibrated output of the heater voltage and current. Also included are interlocks to trip the heater in case of power loss or high vacuum in the tube. Below the cathode heater control are the trigger control, high voltage supply, vacuum pump control and power supplies for the solenoid magnet coils and gun coil. The middle rack holds the PFN for high voltage modulation, highlighted in Figure 5-17. The right rack holds the safety interlock system and active experiment switch-over control board for either the TWT experiment or the alternative experiment in the lab which uses the same PFN. The safety interlock system contains sensors for vacuum pressure, magnetic field, water flow, and PFN settings. In addition, there is a light curtain to prevent personnel from accessing the high voltage area while the experiment is operating. If access is required, the light curtain interlock has a 10 minute override switch.

All interlocks must be satisfied to turn on the high voltage power supply and operate the experiment. If any interlock is switched off while operating, the high

Figure 5-19: The control system for the experiment and safety interlock system.

voltage will automatically turn off and the safety grounding crowbar switch will be unarmed in the high voltage pulse transformer. Other experiment elements will turn off, as needed. For example, if the cooling water to the magnet is interrupted, the high voltage power will turn off along with the magnet power supplies in order to prevent the magnets from over-heating. The selective experiment control allows for safe operation of the sensitive components of the system.

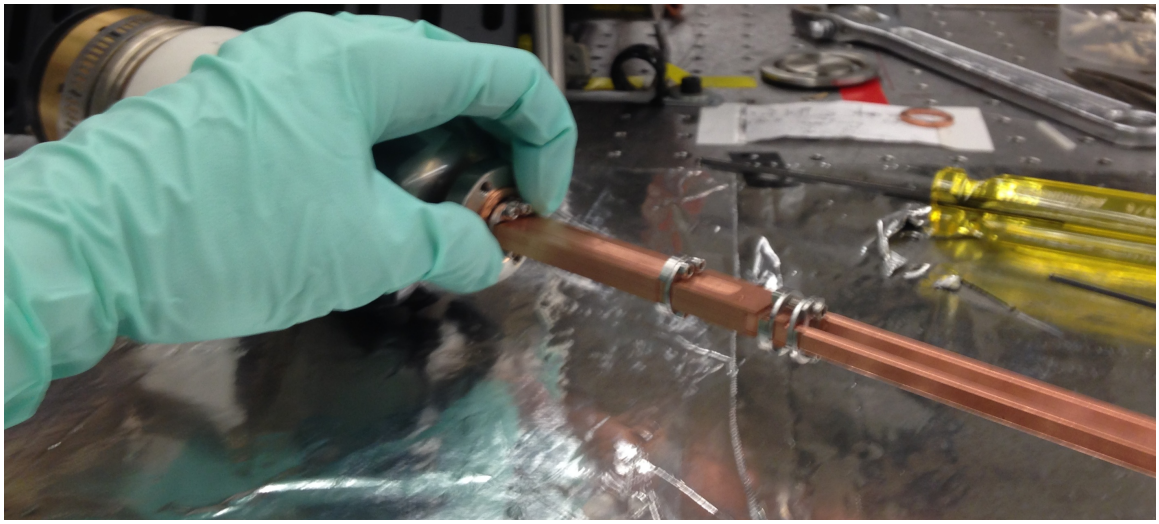

Figure 5-20: Installation and alignment of the TWT structure onto the anode. The alignment surface is held in place with 4 screws on the back-side of the copper anode piece.

5.8 Installation

The installation of the TWT experiment is shown in Figures 5-20 to 5-23. The tube must be assembled and installed in the solenoid magnet simultaneously. Since the tube cannot be easily accessed after installation, components underwent bake-out at 150–200 °C prior to assembly.

To begin installation, the electron gun is aligned to the TWT structure. Figure 5-20 shows the TWT structure being connected to the back of the anode on the electron gun. Four screws secure the alignment surfaces and ensure proper mating between the parts.

After the structure and outer vacuum tube are connected, the tube is inserted into the magnet, and the rest of the components on the collector side of the tube are put into place. Figure 5-21 shows the assembly of the WR-10 waveguide bends with the insertion of the support structure which holds the bends in place inside of the tube. This support aligns the waveguide bends to the straight waveguide sections from the input and output of the TWT structure. Figure 5-22 shows the completion of installation with the connection of the RF windows on 2-3/4 inch conflat flanges, collector, and ion pump for the collector side of the vacuum tube. Also visible in this

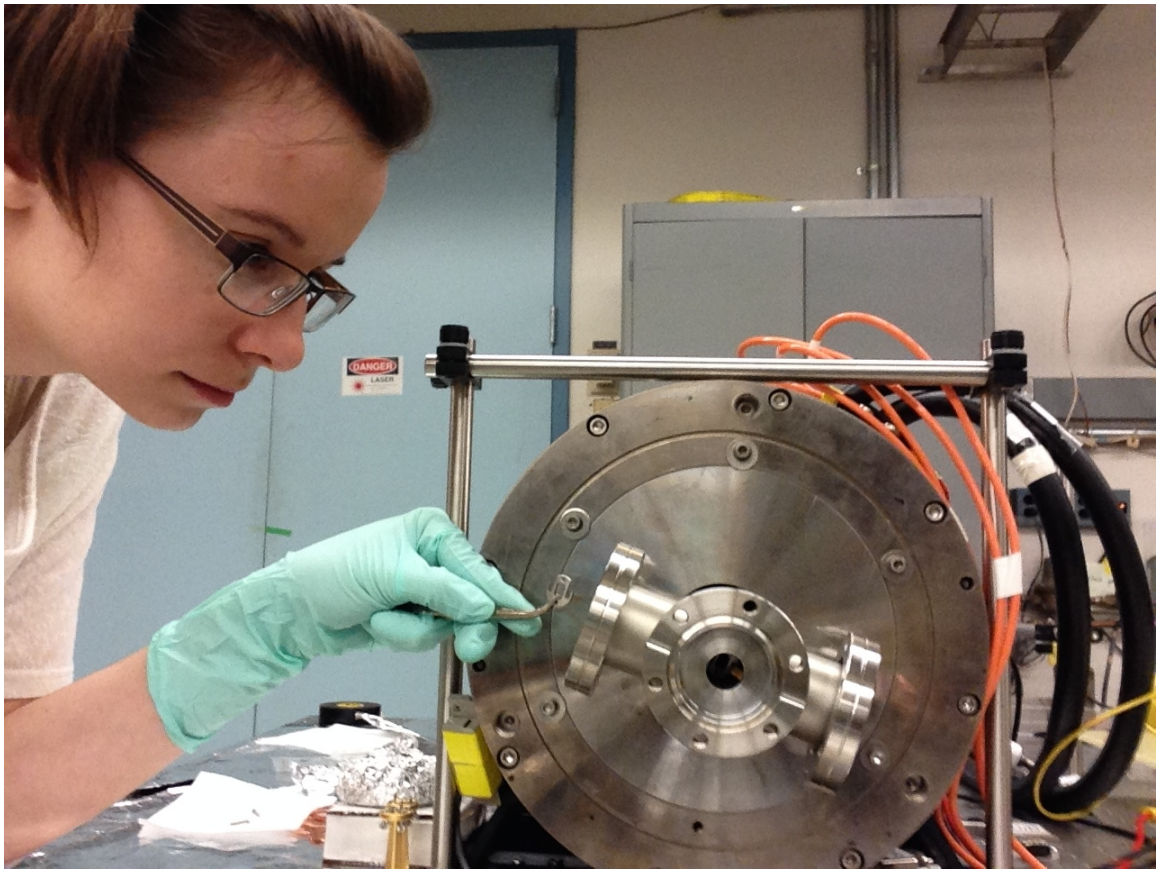

Figure 5-21: Installation of the WR-10 90 degree waveguide bends and support structures into the tube.

figure is the gun coil and electron gun on the right side of the magnet.

Figure 5-23 shows the final laboratory set-up, where the EIO is connected to the input port (right) and an attenuator and detector diode are connected to the output port (left). An acrylic box isolates the high voltage electron gun for safety.

The ion pump controls and grounding wires are routed through Rogowski coils which monitor the pulsed currents deposited on the collector and body of the tube from the electron beam. An oscilloscope near the control panel reads in these two current signals and the voltage pulse. As needed, the RF output power, input power, or power reflected at the input of the TWT can also be monitored via WR-10 detector diodes. Experiment measurements and results will be discussed in the next chapter.

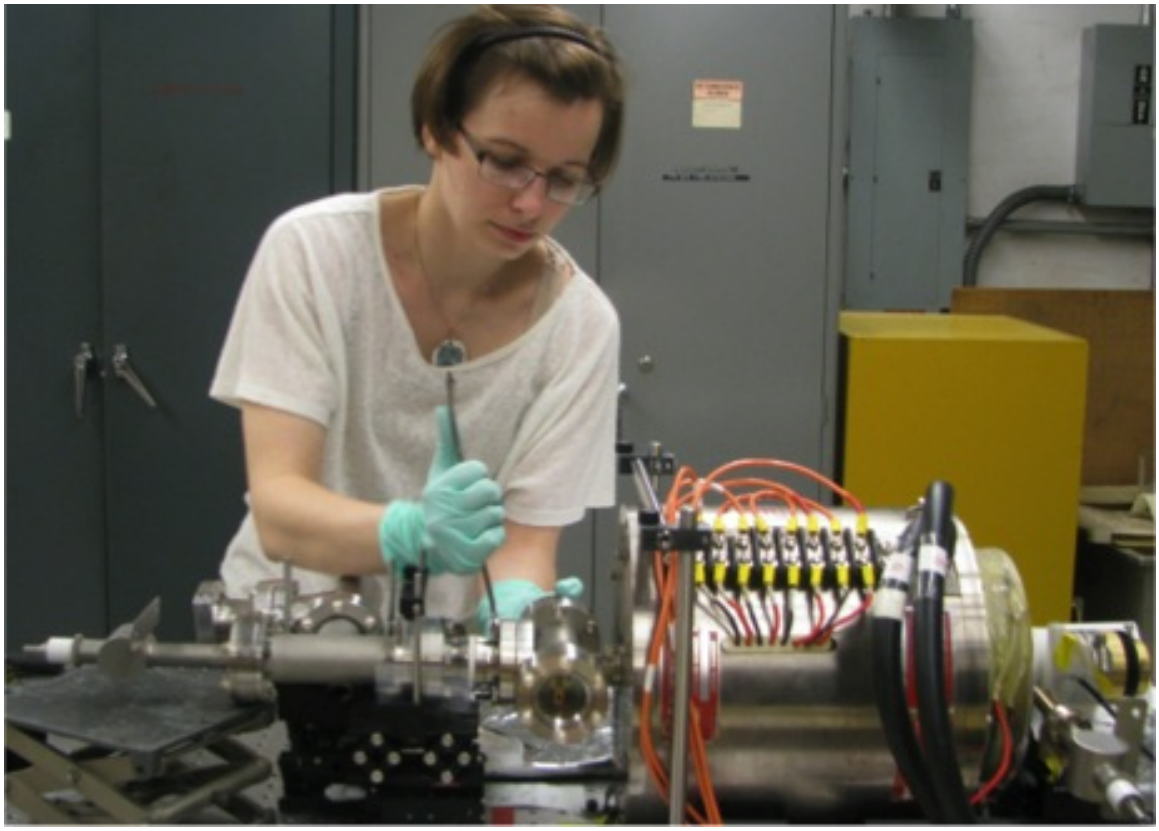

Figure 5-22: Completion of installation for the TWT experiment. Standard 1-1/3 inch and 2-3/4 inch conflat flanges were used in design.

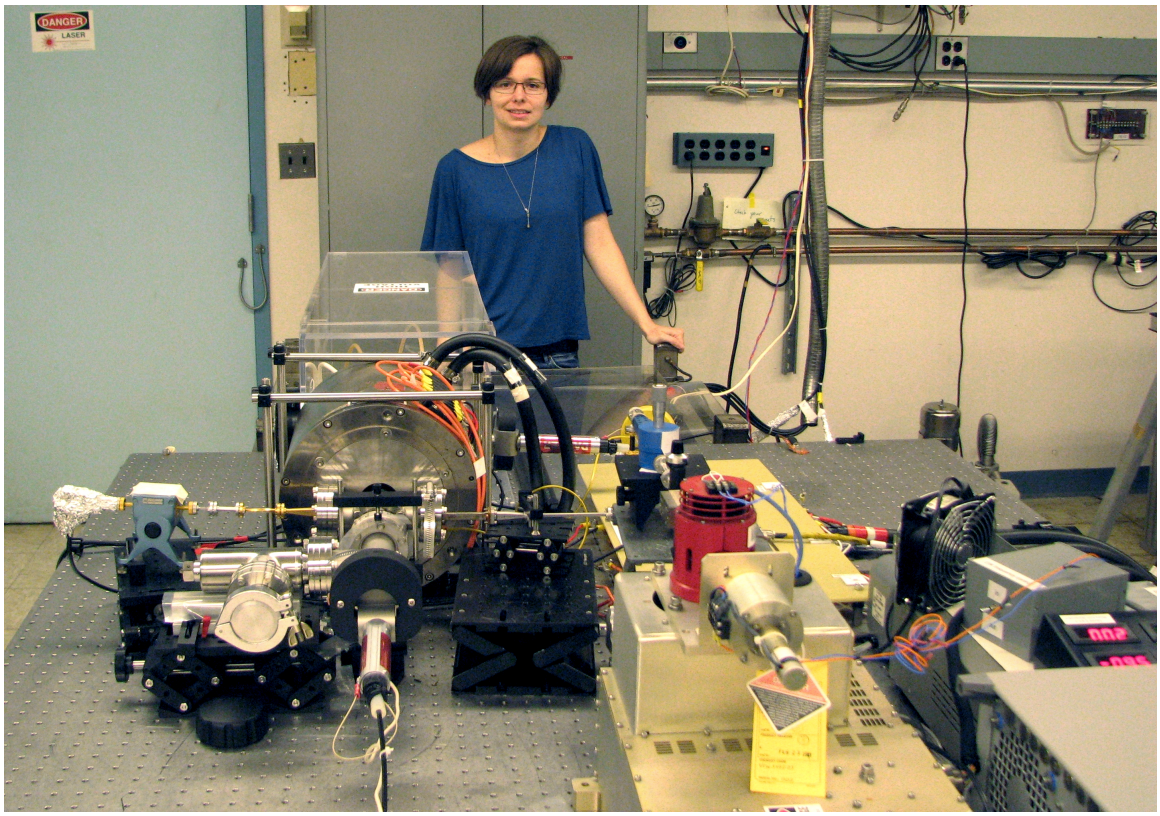

Figure 5-23: The fully assembled TWT experiment, showing the EIO input and diode detector at the output of the circuit.

Chapter 6

Experiment Results

The TWT experiment underwent four distinct builds in the process of testing. First, a beam test was done without a TWT structure in place in order to verify the operation of the test stand and electron gun. Second, the first 87-cavity TWT was installed, Structure A, with full dielectric loading in place. Third, Structure A was re-installed with half of the dielectric loading in place. Finally, the second 87-cavity structure, Structure B, which was extensively cleaned, was installed and tested. In the test of Structure B, the pole pieces on the magnet were adjusted to compensate for the axis offset which was found to be present between the magnetic field and bore center.

The results of these experiments will be discussed in this chapter.

6.1 Electron Gun Beam Test

A test of the electron gun was performed in order to verify operation of the TWT experiment test stand and confirm operation of the electron gun to specifications. The goal of the beam test was to verify the I-V relationship (Child-Langmuir limit) of the gun and measure the transmission of current to the collector. In addition, this test verified that all equipment and measurements were functioning properly.

A cross-sectional rendering of the beam test experiment is shown in Figure 6-1. The electron beam travels from the cathode and through the anode, which has a 0.8 mm diameter (the diameter of the beam tunnel for the TWT design). For the

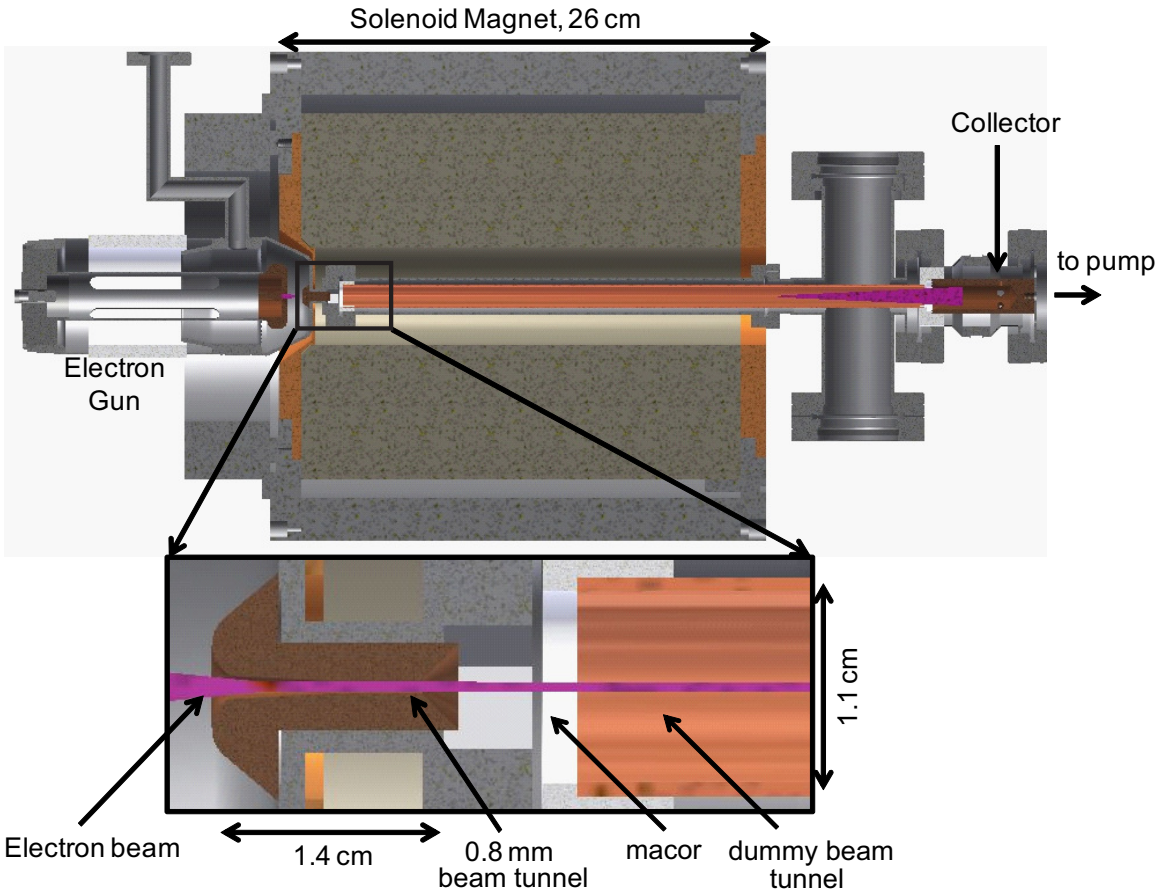

Figure 6-1: A cross-sectional rendering of the beam test experiment. This experiment uses the same components as the TWT experiment, except the TWT structure has been replaced by a dummy beam tunnel. The cut-away shows the beam tunnel which is electrically isolated from the anode with macor.

beam test, a copper pipe with a diameter of 2.5 cm was used as the dummy beam tunnel between the anode and the collector. Instead of using the alignment surface on the anode (which the TWT structure will use), the beam tester was chosen with a large diameter that did not require precise alignment. Due to this design, the dummy beam tunnel could be electrically isolated from the body of the tube. Therefore, the current emitted from the cathode was separated into three measurable components: body current, beam tunnel current and collector current. Due to the nature of the beam test, the body current primarily consists of current that is deposited onto the anode.

The current output of the electron gun was tested over a range of voltages. Align-

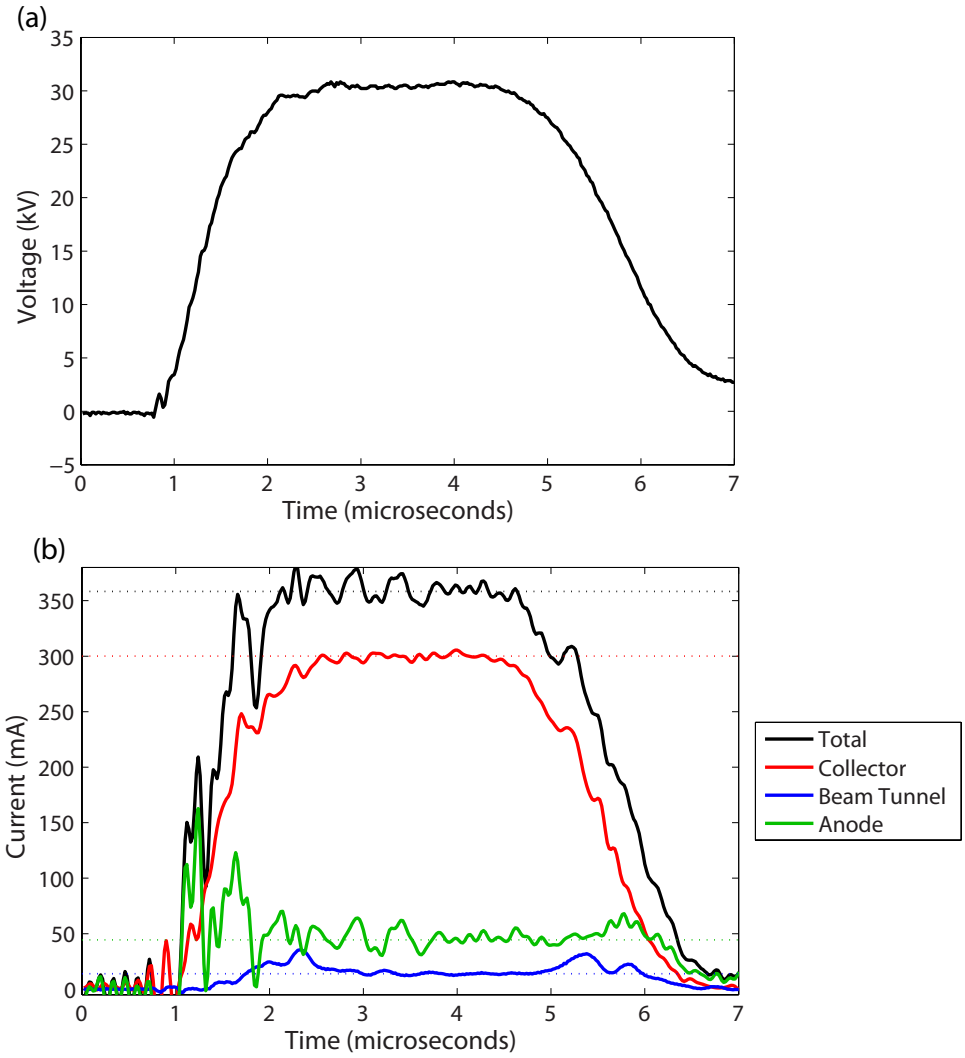

Figure 6-2: Sample traces from the beam test experiment, showing measurements for (a) (negative) Voltage pulse applied to the cathode and (b) the currents measured on the collector, beam tunnel, and anode (body) during the 3 μs pulse. These data were taken with a voltage pulse of 31 kV, and the collector current was measured as 301 mA, with cumulatively 358 mA total current measured.

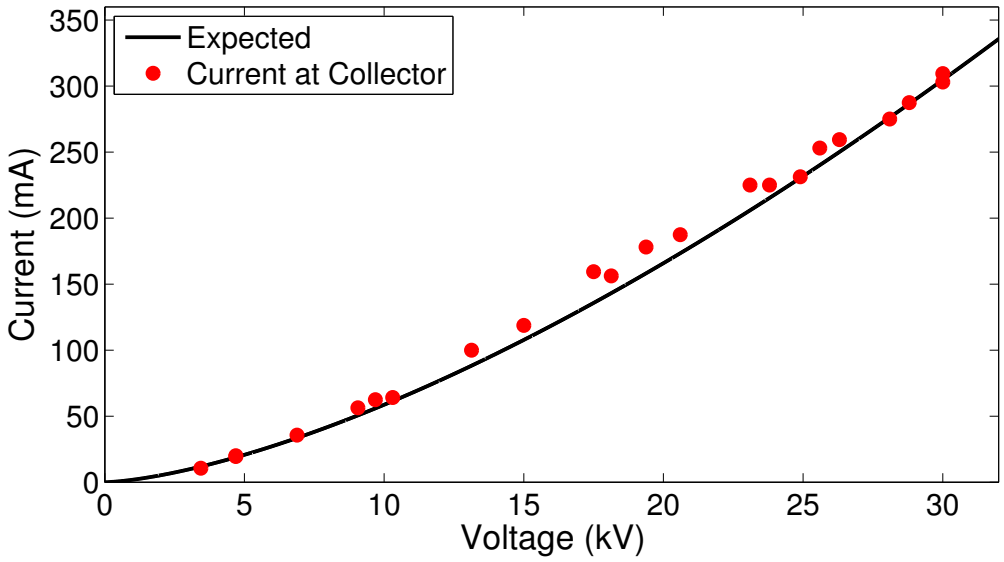

Figure 6-3: The Child-Langmuir curve for the electron gun, comparing the theoretical I-V relationship of the designed electron gun to the measured current at the collector. The gun ideally operates at 31 kV with 310 mA of current.

ment between the tube and magnetic field was performed at low voltages and minimal heater settings (about 1 kV with 10 mA) in order to prevent damage to the anode surface. Operation was found to be best in a wide range of magnetic coil current settings which resulted in a peak on-axis field of about 1.5–2.5 kG (as expected when compared to theory). A sample trace showing the voltage operation at 31 kV, and collector current measurements is shown in Figure 6-2. These curves indicate that the flat-top of the pulse is 2.8 μs, with ± 2 % variation in amplitude. In addition, the current emission directly follows the rise and fall of the voltage pulse. The currents on the solenoid magnets were finely tuned to achieve maximum transmission of current to the collector. Several optimum operation currents which corresponded to peak magnetic field values ranging between 1.5–2.5 kG were observed.

The electron gun performed well and meets specifications. Measured data is shown in Figure 6-3, which shows the calculated Child-Langmuir I-V relationship for the electron gun as compared to the measured current at the collector of the gun. The gun was designed to operate at 31 kV, 310 mA. It should be noted that at this operation voltage, the collector current was 306 ± 6 mA, the body current was approximately

20 mA, and the beam tunnel current was 23 mA. Therefore, there is nearly 88 % transmission of the beam to the collector at the operation point.

It is of note that the electron gun emits more current than anticipated in design. The current deposited on the collector is within range of what was expected for the total current of the design. Therefore, the electron gun is operating within specifications for our experiment. Since the experiment is pulsed, the expected beam interception will not be a problem for TWT operation.

6.2 94 GHz TWT - Structure A

After verifying operation of the electron gun and TWT experimental set-up, the first TWT structure was installed. First, Structure A was tested with full dielectric loading to prevent oscillations. Since Structure A showed high losses compared to theoretical values, a second test of Structure A was performed with half of the dielectric removed.

6.2.1 Full Dielectric

Structure A was installed in the experimental set-up as described in Chapter 5. Aluminum nitride (AlN) composite dielectric was placed on top of the cavity structure. The area on top of the last two cavities was left as a void; this omission will allow for a larger gain to occur in the circuit without introducing oscillations in the device.

After installation, the cathode was re-activated and the tube was aligned in the magnetic field at low voltages. At 31 kV, up to 280 mA was observed on the collector. This value is less than the beam test due to the 7 cm long, 0.8 mm diameter beam tunnel of the structure being introduced. The magnetic field of the solenoid and gun coil were adjusted to fine-tune the current transmission and gain in the circuit.

Overall, zero-drive stable operation was observed in the TWT. There was no evidence of oscillations at any frequency in the forward or backward direction. Figure 6-4(a) shows the observed linear and saturated gain at 95.5 GHz with 27 kV operation. The highest gain observed in the device was 8 dB at 95.56 GHz (not graphed). Figure 6-4(b) plots the same data as output power vs. input power. This figure highlights

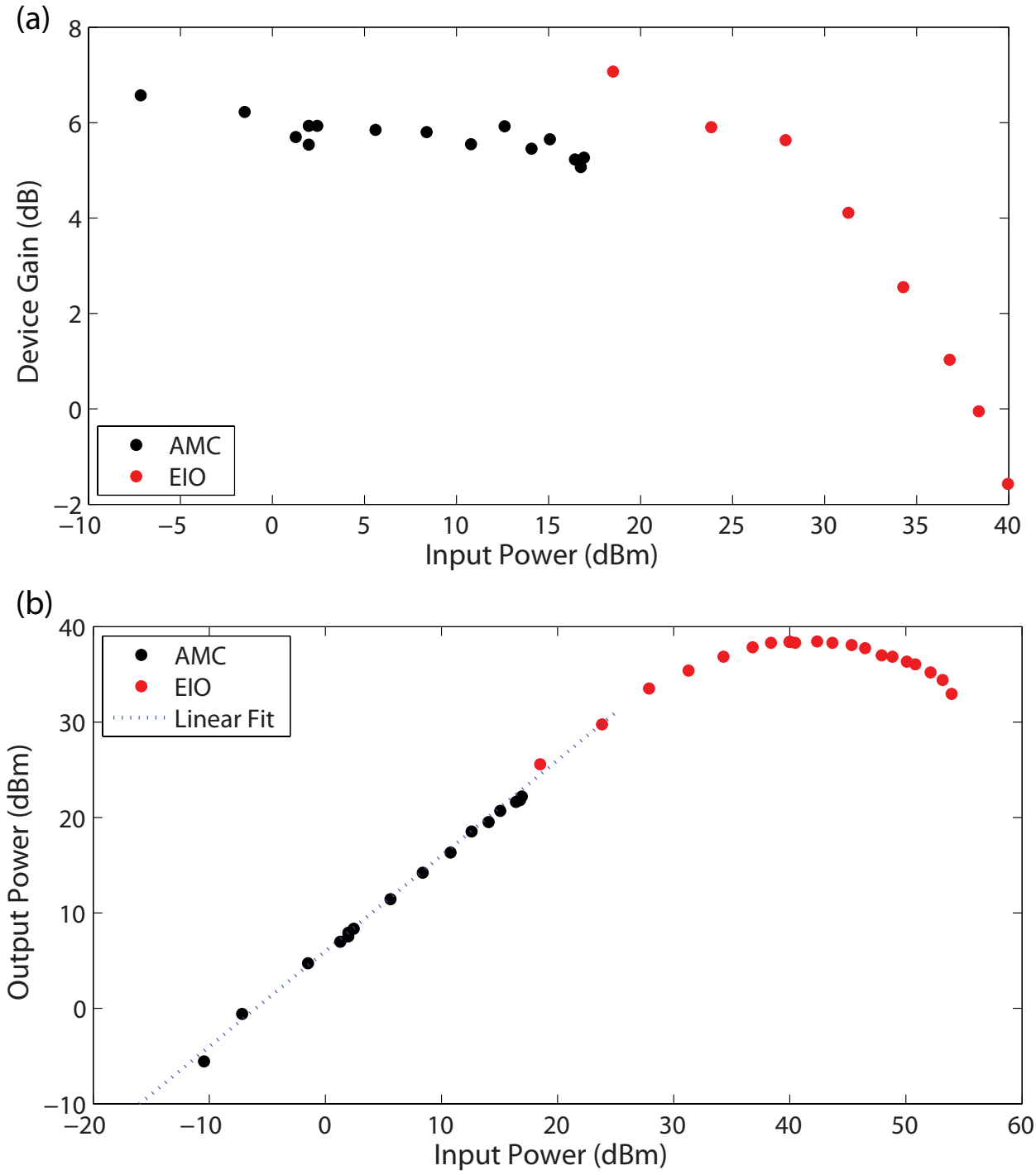

Figure 6-4: (a) Device gain and (b) output power vs. input power observed at 95.5 GHz with V_0 =27 kV. A linear gain of 6 dB (device gain) is shown with 7.5 W saturated output power measured.

the linear gain regime which was measured with the solid state AMC input and the saturation of the circuit which was measured with the EIO input. The highest saturated power observed was 8 W at 95.5 GHz.

It is pertinent to note the difference between device gain and circuit gain. All parameters discussed have been for measurements of device gain. That is, device gain, G_d, is equal to the power measured at output, P_{out}, divided by power at the input window, P_{in}. On the other hand, circuit gain, G_c is the gain which occurs only in the TWT circuit. Circuit gain takes into account the losses due to the rest of the TWT device, L_d, primarily losses at the windows and waveguide outside of the inner TWT circuit. In other words,

$$G_c = G_d - L_d \tag{6.1}$$

In this set up of the 94 GHz TWT, there are significant losses due to the coupling through the windows. Misalignment between the WR-28 waveguides on either side of the windows contribute a large amount of losses, and are difficult to align correctly. This is a fault in the design. It is estimated that at least a total of 3–6 dB of loss occurred in this experiment due to the window set-up. Therefore, the 8 dB measured device gain can be estimated as 11–14 dB circuit gain observed for the TWT at 95.5 GHz.

It should be noted that gain was observed at other frequencies with higher operation voltages, but not nearly as strong as the 95.5 GHz point. Since the transmission through Structure A has resonances, the frequency is not consistently tunable with voltage adjustments. Therefore, the secondary point of operation was 94.55 GHz with 32 kV operation, where up to 4 dB of device gain was observed.

The magnetic field could be adjusted and fine tuned in the 4-coil solenoid. These adjustments led to different operation regimes in the circuit. Figure 6-5 shows the output power detector diode signal and collector current traces that were observed in the system at the 94.5 GHz operation point with V_0 =32 kV. Similar conditions were observed for the 95.5 GHz operation point. Figure 6-5(a) shows an operation point that was taken with an inconsistent magnetic field. The field was adjusted

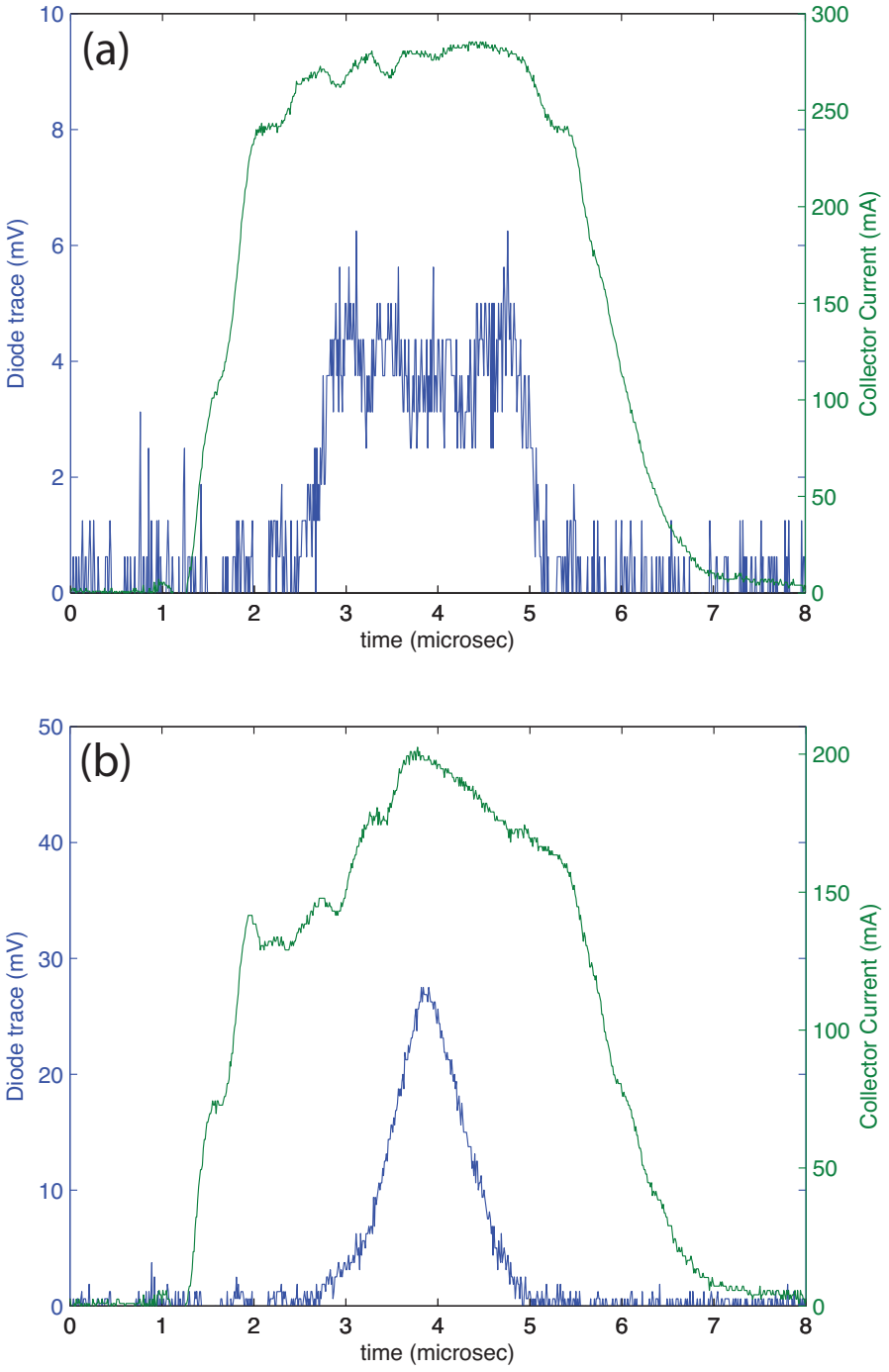

Figure 6-5: Sample traces of the collector current and output power measurements for Structure A under test in the TWT experiment. (a) was observed during low gain operation, where the system was aligned for high current transmission and consistent signal, while (b) was observed during high gain operation.

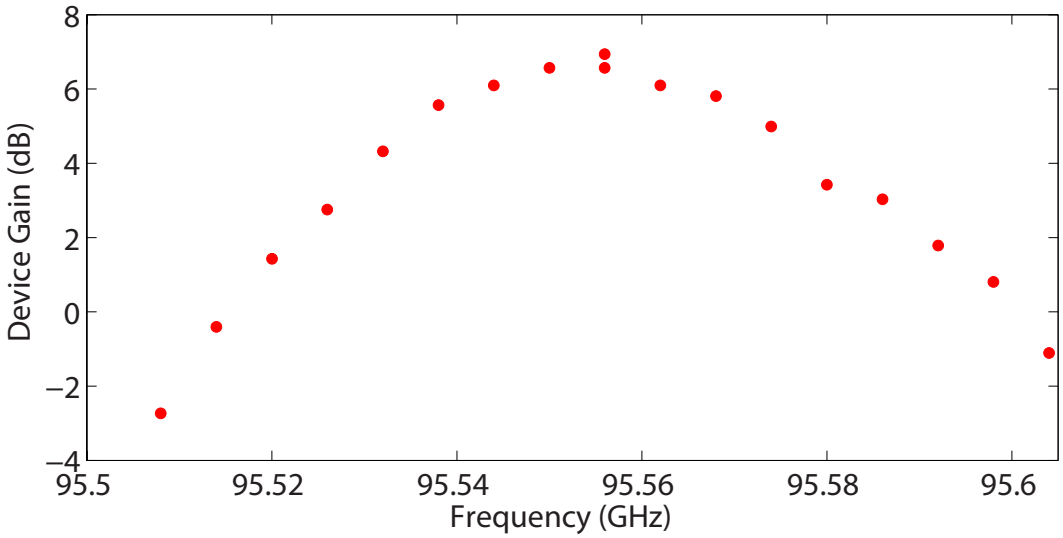

Figure 6-6: Device gain vs. bandwidth for operation at V_0=27 kV (340 mA total measured current).

to allow for high current transmission, 280 mA, to the collector. This resulted in a field that was about 2.5 kG at the outer edges of the magnet and less than the Brillouin field in the center of the magnet. A consistent RF input was used, and the output power detector diode signal is flat and appears smooth in the middle of the pulse (ignoring signal noise). However, only 1 dB of gain was observed under this operation condition. Conversely, Figure 6-5(b) shows the high gain operation point. This point was taken with a very low, but consistently flat, magnetic field, of about 0.9 kG, which is at the edge of acceptable operation for the magnetic field. This operation condition for the magnetic fields led to less than 200 mA of current at the collector and a very inconsistent current trace throughout the time of the pulse. In addition, the RF pulse, which showed 8 dB of gain, was only amplified during the peak in the collector current. Though less current was transmitted to the collector at this operation condition, more interaction occurred between the electron beam and RF signal.

Many factors could have led to the odd operation conditions needed for high gain in the circuit. One possibility is that these operation conditions were due to the magnetic field axis being shifted from the center of the magnetic bore and pole piece center. By operating at a low current, a consistent interaction occurred between the

electron beam and RF wave, but the current was unable to be transmitted to the collector. The shift of the magnetic field axis will be adjusted in Structure B testing.

For the 95.5 GHz high gain operation point, the frequency dependence on gain is shown in Figure 6-6. These data points were taken by measuring the linear gain due to the low power AMC input at various frequency inputs with V_0 =27 kV. This voltage optimized the output for 95.56 GHz operation (the highest gain point observed). A 3-dB bandwidth of 60 MHz was observed for these operation points.

The limited bandwidth and small gain can be traced back to the cold test transmission measurements, where a significant frequency dependence was observed. The best transmission point occurs around 95 GHz (and it follows logically that this frequency may have shifted to a slightly higher frequency under the final installation and vacuum operation). Therefore, the discrepancies measured between the cold test circuit performance and simulation accurately reflect the frequency characteristics observed in experiment.

6.2.2 Half Dielectric

Due to the high loss in the structure when full dielectric was in place, which was 20 dB greater than the anticipated loss (as shown in Chapter 5), it was determined that less dielectric could enhance the gain results seen in the structure. CST simulations indicate that less dielectric would result in TM_{31} round-trip oscillations. That is, the loss associated with the TM_{31} mode would be less than the gain in the circuit and would create an unstable condition in the TWT. However, these simulations predicted much less loss in the circuit than was measured and may not be valid for Structure A with more loss present.

Structure A was installed with dielectric in place for the first 42 cavities. For the remaining cavities, a void was left where the dielectric slots were machined. During operation, consistent TM_{31} mode oscillations were present in the device at 95.75 GHz for a 27 kV voltage pulse. No fundamental mode, TM_{11}, or backward wave oscillations were seen in the device. At 94.5 GHz operation with V_0 =30.6 kV, less than 1 dB of gain was observed during zero-drive stable operation. The electron beam was likely

modulated by oscillations during the voltage rise, preventing the previously observed operation. The oscillations in the circuit prevented the high gain point in the previous test from being reached.

6.3 94 GHz TWT - Structure B

Structure A showed substantial results, but it was possible to improve the gain of the TWT. Two sources of non-ideal behavior were discovered in the system: misalignment of the magnetic field and burrs in the structure. These errors could be adjusted with a second build of the TWT.

The misalignment of the magnetic field was already discussed in Chapter 5. To fix this in experiment, the front iron pole piece was modified to have a center hole that was positioned off of the magnetic bore axis by 2.5 mm, and positioned in the correct orientation during installation of the tube. The back iron pole piece was also adjusted to be aligned with the magnetic center.

Upon inspection of both Structures A and B, it was evident that many burrs were present in the structure after machining and standard cleaning for vacuum. Structure A was installed without further cleaning, but Structure B underwent a much more extensive cleaning with 0.2 mm acupuncture needles, and the machining burrs were successfully removed from the structure. Upon cold test measurements, shown in Chapter 4, it is evident that the extensive cleaning enhanced the transmission in Stricture B, decreasing ohmic losses and reflections.

6.3.1 Results

After cleaning, Structure B was installed in the TWT with full AlN composite dielectric loading. As was the case with the full dielectric test for Structure A, the area on top of the last two cavities was not filled with dielectric and was left as a void. Since the tube could not be aligned to the center of the magnet bore, alignment of the device was more complicated, but successfully achieved at low voltages.

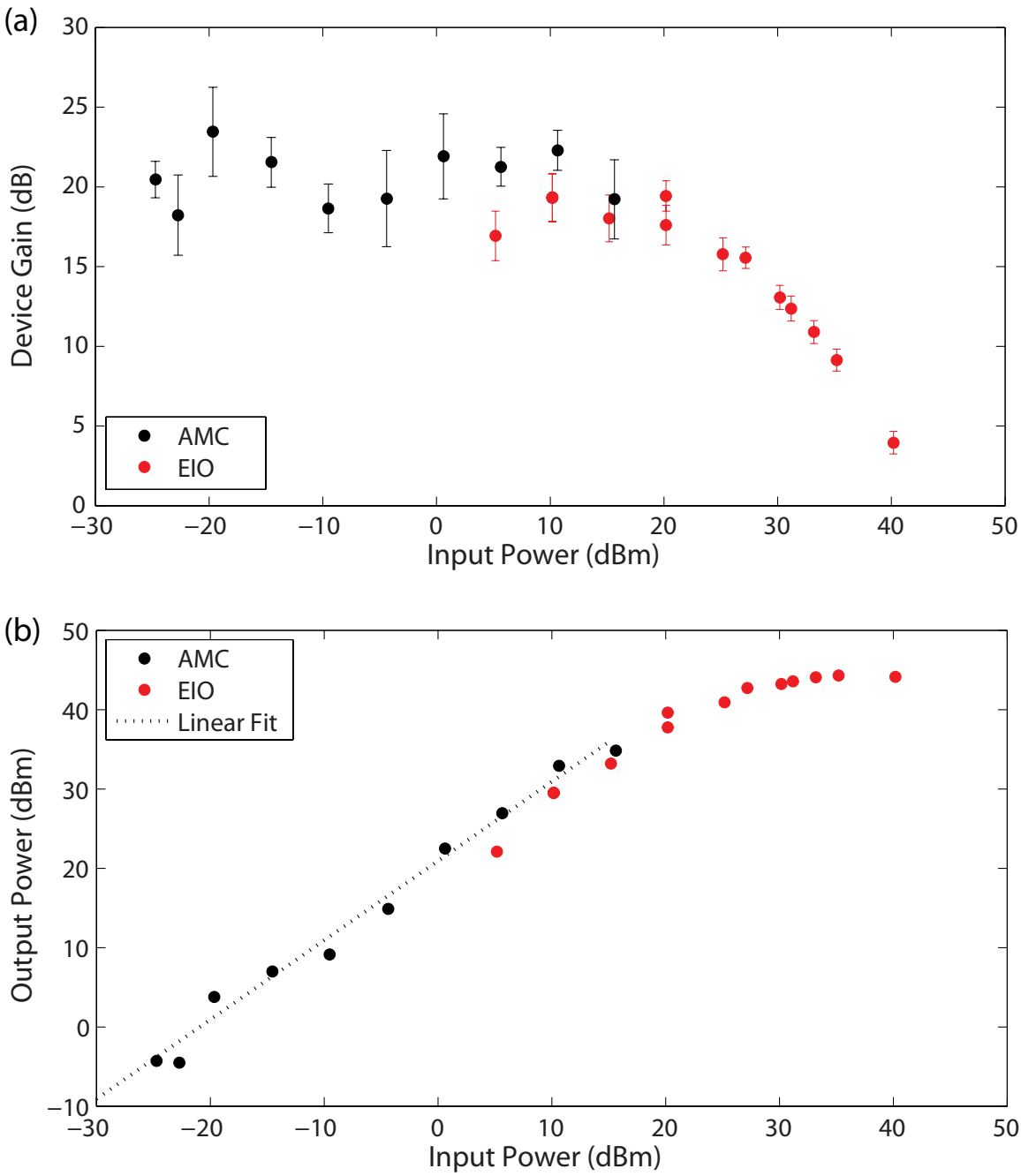

Figure 6-7: (a) Device gain vs. input power and (b) output power vs. input power measured at 94.27 GHz. The input power was provided by a low power solid-state AMC or high power EIO, as indicated. The TWT has 20.9 dB of linear gain and 27 W peak power.

Zero-drive stable operation was achieved, and gain was observed at several frequencies. The largest low power linear gain measured was 20.9±1.7 dB, which occurred at 94.27 GHz with a voltage of 30.6 kV. The results for the gain measured in these conditions is seen in Figure 6-7. Two data sets are shown; the low power set used the solid-state amplifier multiplier chain (AMC) for the input signal, and the high power set used the W-band EIO. The magnetic fields were kept with a consistent flat-top at about 1.6 kG, which allowed 250 mA of current on the collector. The linear fit in Figure 6-7(b) for the AMC data corresponds to 20.9 dB of device gain.

As was the case with Structure A, the circuit gain can be calculated by eliminating other system losses from the device gain measurement. Primarily, these losses are due to the input and output coupling through WR-28 waveguide and the fused silica windows. This gain is split between ohmic and reflective losses that occur in the WR-28 waveguide and tapers.

The coupling set-up was tested with a PNA. The transmitting millimeter wave head had WR-10 waveguide which was connected to a WR-10 to -28 taper which was placed against a fused silica window, and the receiving head had the same set up on the other side of the fused silica window. These cold tests showed that about 1–2 dB of power would be lost due to trapped power in the WR-28 waveguide (with a large frequency dependence), and about 1–4 dB of power would be lost due to reflections between the WR-10 to -28 waveguide tapers and misalignment between the two WR-28 cut-off waveguides on either end of the window. Therefore, a total of 2–6 dB is expected as the coupling loss at the input or output of the TWT circuit.

In the TWT experiment, the EIK was used to measure the losses through the entire TWT device. The losses in the TWT device, including the input and output coupling through two fused silica windows and the TWT circuit, were measured to be −36.3±0.6 dB at 94.3 GHz. At this frequency, the measured transmission through the TWT circuit, Structure B, in cold test (as shown in Figure 4-12) was −30.1±0.5 dB. Therefore, the losses due to coupling at the input and output of the circuit can be extracted from these measurements. The input and output coupling losses, combined, were measured in the device to be 6.2±0.6 dB at 94.26 GHz. For simplicity in analysis,

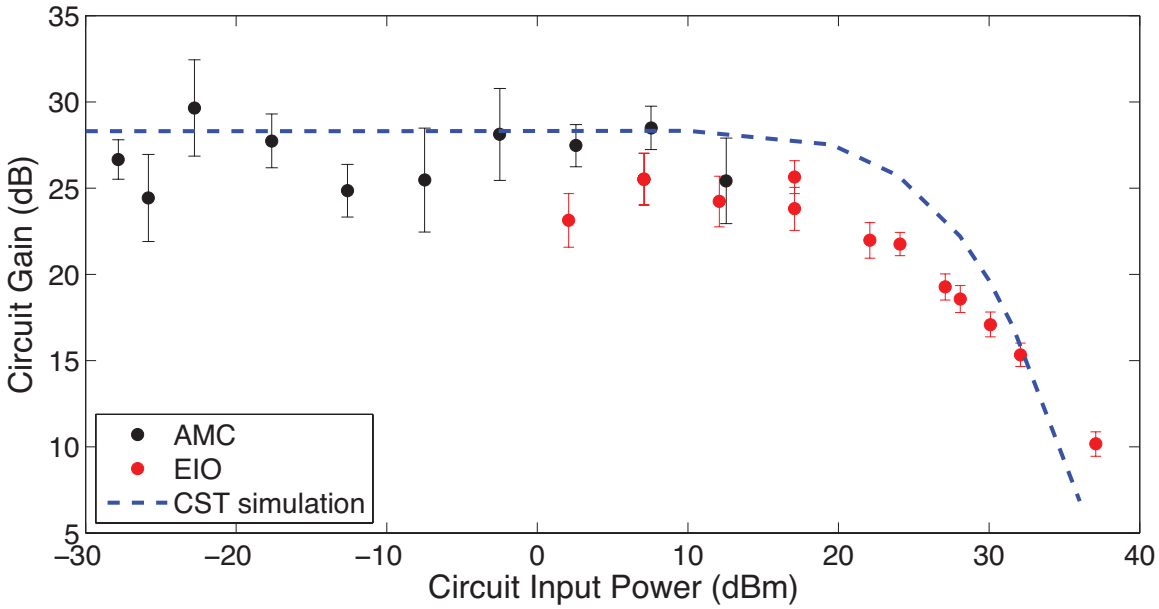

Figure 6-8: Circuit gain in the TWT as compared to simulated gain with CST for 250 mA beam current. The input power has been adjusted to indicate the power input into the TWT circuit.

it's assumed that half of these losses, 3.1 dB, occur at the input and half occur at the output. This measurement is in good agreement with the independently measured coupling losses expected in cold test, 2–6 dB. With this measured coupling loss taken into account, the circuit gain of the TWT is 27.1±1.8 dB. This is rounded to be a reported circuit gain of 27±2 dB.

The solid-state W-band AMC was used for low power operation, but in order to achieve saturation, the EIO was used. The input device for each measured point is indicated in Figure 6-7. The input power was regulated with a variable attenuator at the input. The frequency of the EIO is tuned manually in the device, and, therefore, cannot be set as accurately as the AMC. The maximum output power observed was 27±5 W at 94.26 GHz. This point can be seen in Figure 6-7(b) where the measured output power levels off at 27 W. Assuming that the measured coupling loss is split evenly between the input and output circuits, the saturated output power at the end of the TWT circuit would be 55 W.

A comparison of the measured circuit gain and the theoretical calculation of the gain in the TWT is shown in Figure 6-8. In the theory, the current through the TWT

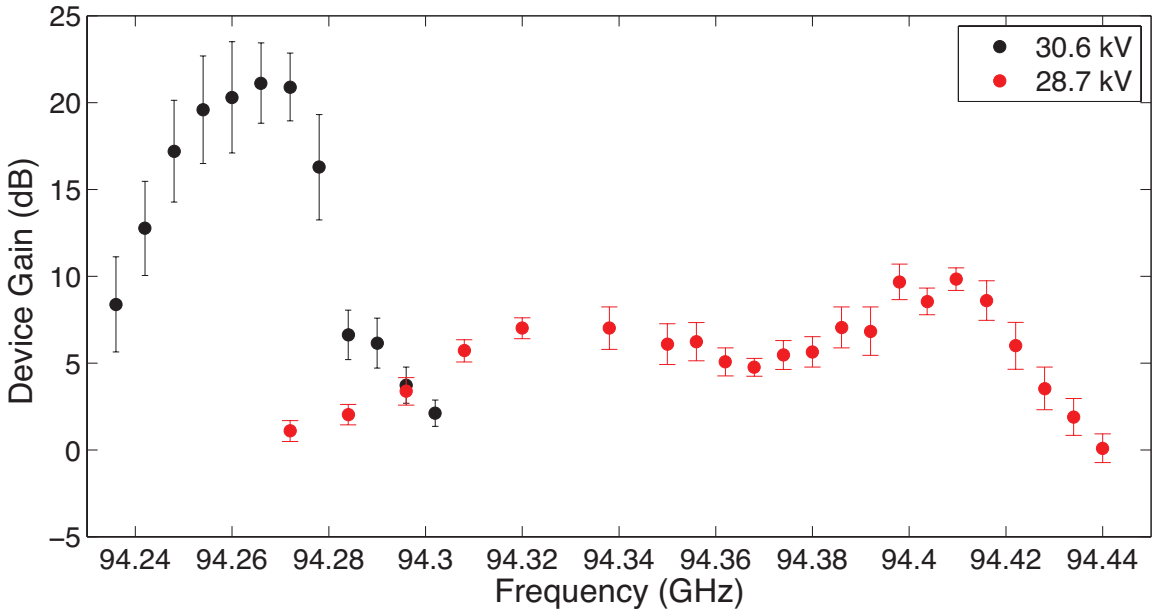

Figure 6-9: Device gain vs. frequency in the TWT for two different operation points; 30.6 kV operation shows the high gain point, and 28.7 kV operation shows a wider bandwidth operation point.

has been adjusted to be 250 mA to match the experimental current and all other parameters are kept as stated in Chapter 3. With this adjustment, the theoretical circuit gain for the TWT is 28.3 dB and the measured circuit gain is in good agreement with theory. In addition, the theoretical saturated output power is 113 W. The measured saturated power is likely lower due to increased beam interception during high power operation.

The bandwidth of the TWT for two different operation points is shown in Figure 6-9. The high gain operation point, as discussed above, is shown as 30.6 kV operation. The bandwidth of this operation is 30 MHz, centered at 94.26 GHz. Another operation point with a larger bandwidth is shown for 28.7 kV operation. The 3-dB bandwidth for this point is 40 MHz, centered at 94.45 GHz, but the 6-dB bandwidth is 120 MHz, quite larger. Theoretically, there should be 200 MHz of bandwidth at the high gain 30.6 kV operation point. The limited measured bandwidth could be due to several factors that will be discussed in detail in the next section: limited current, transverse magnetic field, and inconsistent flat-top voltage.

6.3.2 Analysis

Samples of the diagnostic measurements for a typical high gain pulse are shown in Figure 6-10. In this pulse, a low power signal at 94.26 GHz is provided by the AMC at the input. A 30.6 kV input pulse of 2.8 μs is shown in Figure 6-10(a) along with the diode trace. The detector diode is placed at the output of the circuit, after a variable attenuator, and has been calibrated so that it directly measures the output power of the circuit. It should be noted that the measured output power presented in this chapter was the average power detected during the last microsecond of flat-top of the pulse, from 3.6–4.6 μs. Figure 6-10(b) shows the current measured at the collector and body of the TWT. For comparison, the current traces where no RF power is present in the TWT for the same operating conditions are also shown. The presence of low power linear amplification has little effect on the current in the system.

From these diagnostics, there are two curious measurements that must be addressed: there is a very high percentage of body current and the diode measurement is not consistent for the duration of the pulse.

In a standard TWT, the body current should be less than 5 % of the total current, even less for a commercial, CW TWT. Since this is an experimental pulsed device, the TWT can operate with high body current, though it can introduce some problems and should be addressed. The large quantity of body current in the system is likely due to the magnetic fields in the TWT. Any inconsistencies in the magnetic field will result in beam interception throughout the TWT. The magnetic field has been changed from Structure A to fix some misalignment, but it is still not ideal. Comparison between the body current measurements for the two experiments during high gain operation shows better current transmission in the testing for Structure B. However, there is still between 40–50 % beam interception through the duration of the voltage pulse. In addition, the current transmission shows a dependence on time during the flat-top of the voltage pulse. During ideal operation, this time-dependent behavior would not be present. Several factors could contribute to time-dependency, like a rising pressure during the pulse due to beam interception or beam rotation due to transverse

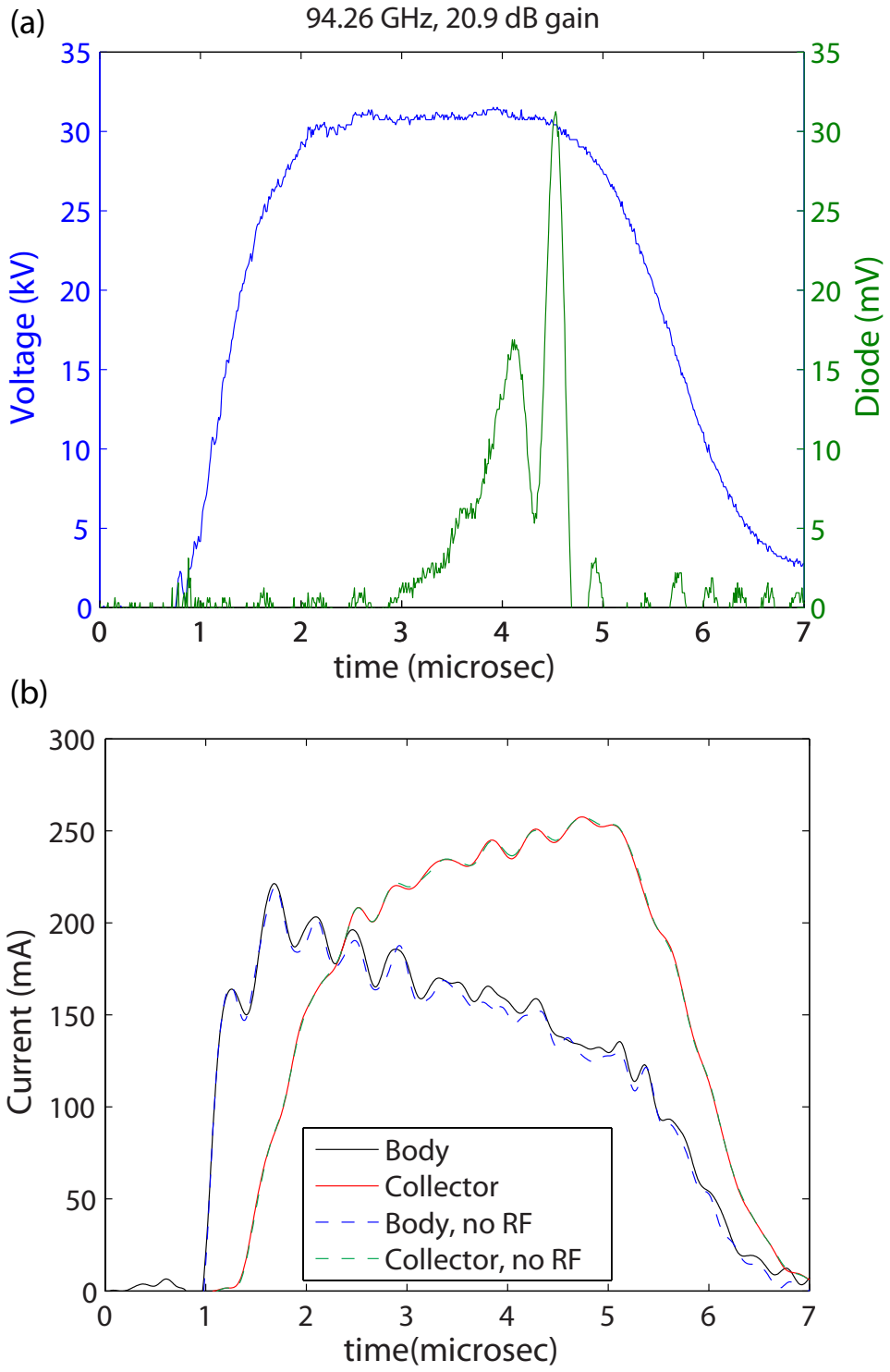

Figure 6-10: The diagnostic measurements for a high-gain operation point at 94.27 GHz with a low power AMC input, showing (a) voltage and output detector diode signals vs. time and (b) current signals vs. time for the duration of the 3 μs pulse.

magnetic fields. It should be noted that up to 280 mA of collector current was possible (approximately 70 % current transmission), but these operation conditions did not correspond to a high gain point.

There are several reasons as to why the diode measurement is not consistent across the pulse. The most notable reason is that the output power is related to the beam current in the TWT. Since the current on the collector rises during the duration of the pulse, it follows that the interaction current in the TWT also rises during the pulse, leading to more gain in the TWT at the end of the pulse than at the beginning. However, the effect in the output pulse is too large to be accounted for by this change in interaction current, since the gain is only proportional to $I_0^{1/3}$. Another reason for this behavior could be the beam shape and quality due to the magnetic field. If the beam is rotating early in the pulse, it would not have a strong interaction with the RF field.

Another factor to consider for both the inconsistent collector current and amplification is the flatness of the voltage pulse. Typical operation of the TWT would allow for small variations in the voltage pulse, less than 1 %. The voltage pulse for the TWT, as measured, has ± 2 % variation, with a stronger variation evident during the first microsecond of the flat-top. Gain at a certain frequency is dependent strongly on voltage, and large voltage variations will result in atypical bunching of the electron beam. Since the bandwidth is small in the device, the TWT is less tolerable to voltage variation, intensifying the effect of the flat-top variation on the performance of the TWT. The variation is larger at the beginning of the pulse, leading to a time-dependent variation in the field.

During saturation, the diagnostics look very similar to high gain operation, with some other distinct characteristics. A sample pulse for operation during the 27 W saturation point is shown in Figure 6-11. The EIO provided a 10 W input signal from 2-6 μs to overlap with the flat-top of the voltage pulse. The same conditions of operation for the linear gain points were kept. The current traces are shown alongside current traces where no RF signal was present in the TWT.

As was seen in the high gain case, amplification is only present during the later

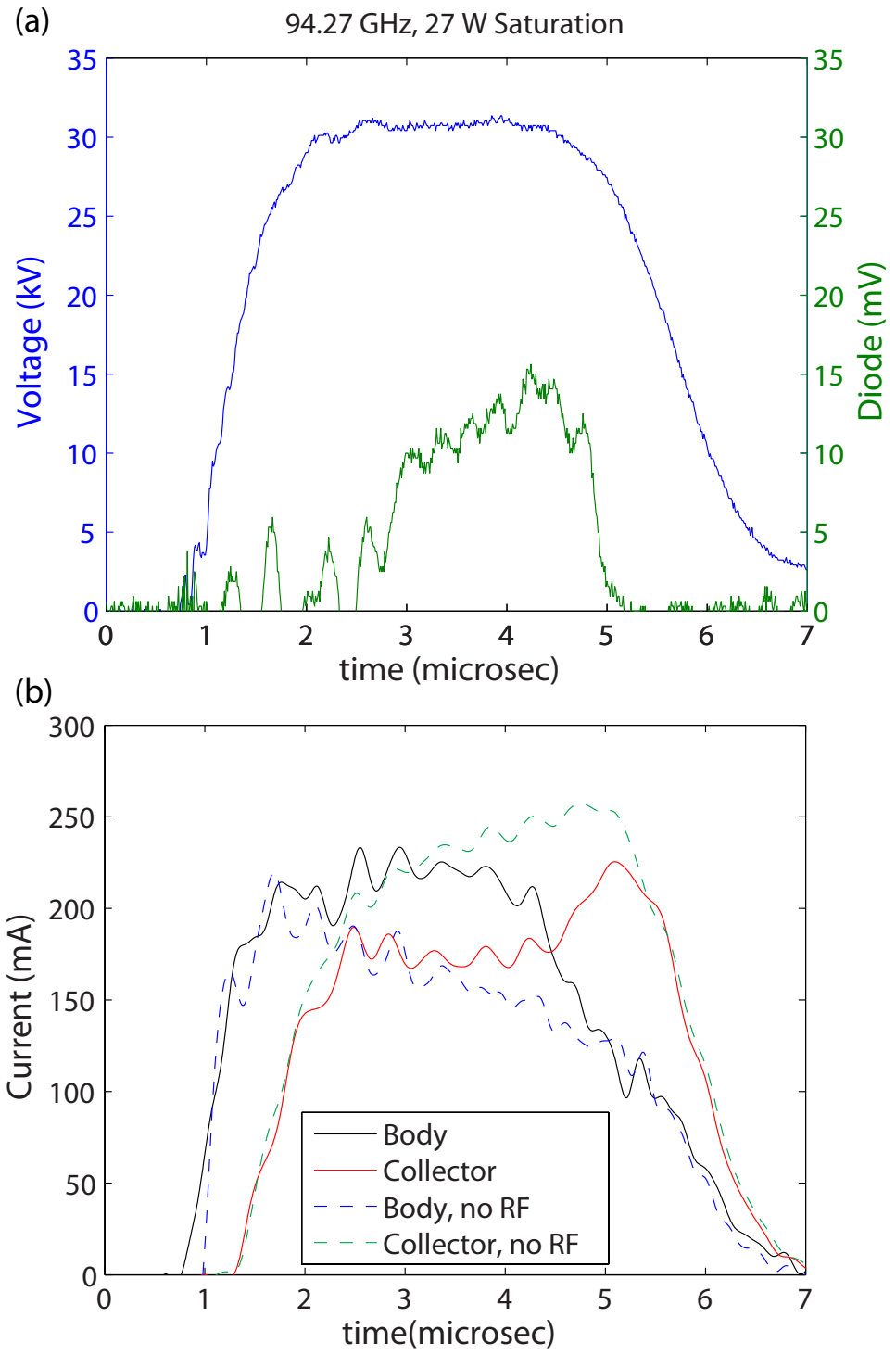

Figure 6-11: The diagnostic measurements for the saturated power operation point at 94.26 GHz with a high power EIO input, showing (a) voltage and output detector diode signals vs. time and (b) current signals vs. time for the duration of the 3 μs pulse.

part of the pulse, seen in the output diode detector output from 3–5 μs. The diode pulse appears wider since the high gain points later in the pulse (4–5 μs) are severely saturated, while the lower gain points (from 3–4 μs) have only just reached saturation; this effect causes the pulse to appear more level. Of note is that the rf pulse is not amplified at the start of the flat-top (from 2–3 μs). This behavior in the saturated power indicates that poor interaction is happening at the start of the pulse, possibly due to the voltage variation during this time frame.

Also seen during saturation is an increase in the beam interception. This effect can be seen by a comparison between the collector current with and without RF in the TWT. During saturated output power, the collector current dips (conversely, the body current rises) by over 50 mA. This is due to the fact that the beam is de-bunching at the end of the TWT, after energy has been transferred from the beam into the wave. At that point, the electron beam parameters are no longer matched to the magnetic field of the system; the beam spreads radially, leading to current interception in the beam tunnel. In order to increase gain in the device, the magnetic field was adjusted to 1.6 kG, instead of the 2.5 kG simulated. This magnetic field adjustment could prohibit the de-bunching electrons from reaching the collector.

Due to beam interception during saturation, there is less current at the end of the TWT at high powers than at low powers. Even though there is a small amount of power output compared to the beam power, the collector current is seen to decrease during saturation. By losing current in the TWT, the effects of saturation are seen at lower input power levels than observed in simulation, leading to the difference seen between simulation and experiment in the curve of the data at high power levels. In addition, the maximum output power will be less than simulated due to there being less overall current in the TWT at the saturation point, leading to only 55 W maximum output power instead of the predicted 114 W. Despite these circumstances, theory and experiment match well.

The data discussed so far was all collected during zero-drive stable, pulsed operation. However, the TWT did see some oscillations evident in the device under very specific and controllable circumstances. A sample oscillation along with the diagnos-

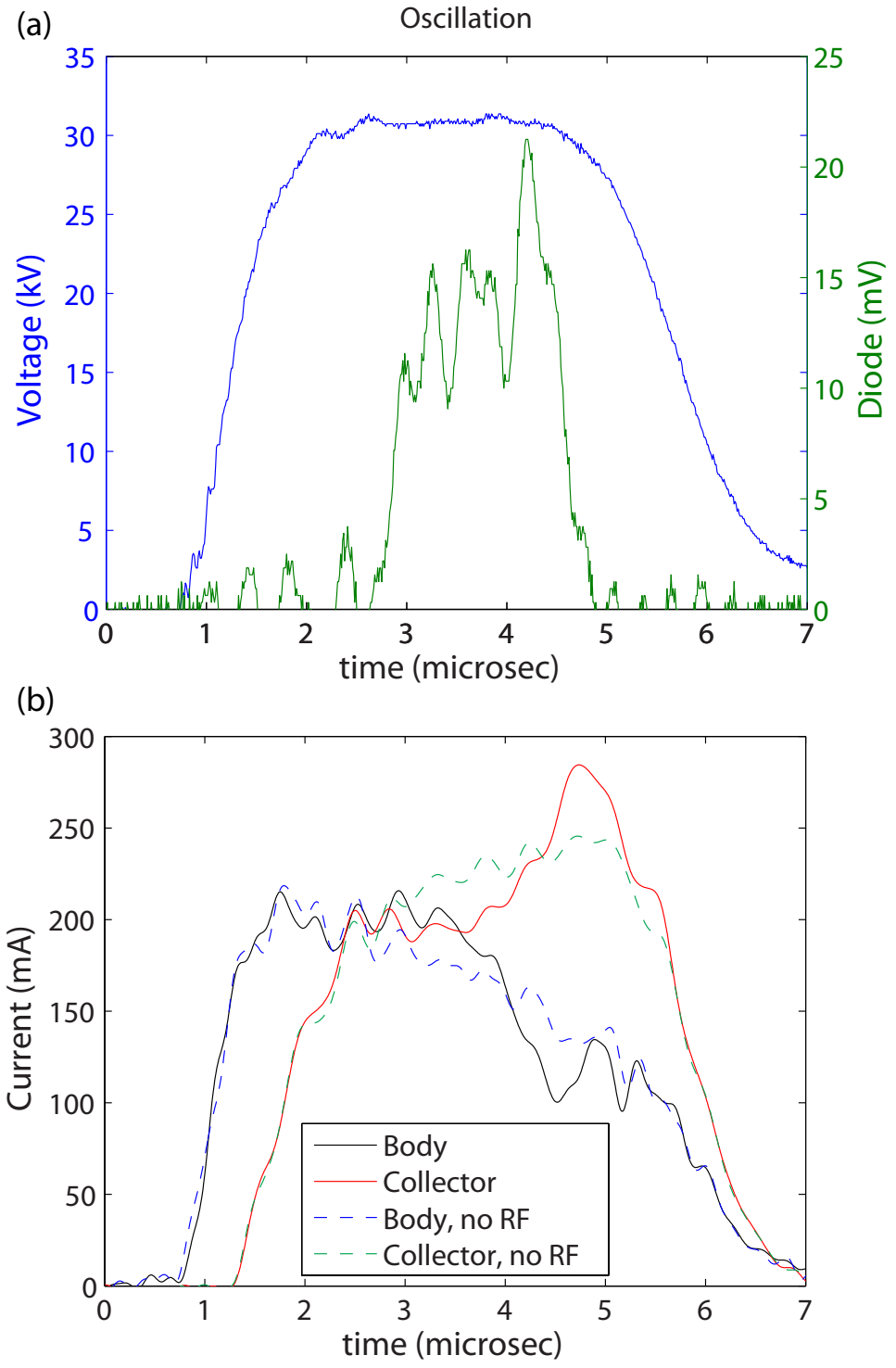

Figure 6-12: The diagnostic measurements for an oscillation observed during the start of operation, showing (a) voltage and output detector diode signals vs. time and (b) current signals vs. time for the duration of the 3 μs pulse.

tics for the pulse is shown in Figure 6-12. This oscillation occurred during the start of operation, when the pressure in the TWT was quite low. After initial pulsing, the oscillation was not present in the device while operating at 1 Hz. Figure 6-12(a) shows the 30.6 kV voltage input pulse and the output diode detector signal, which was calculated to be 20–30 W in power. The current traces along with the standard operation current traces are shown in Figure 6-12(b)

The frequency of the oscillation could not be measured due to the limited time of operation in conditions that could induce the oscillation. However, the signal was detected through WR-08 waveguide, indicating that it is has a frequency above 74 GHz (the cut-off frequency of WR-08 waveguide) and likely oscillates in the TM_{31} mode of the TWT cavity.

During this initial operation condition with very low pressure, the collector current was significantly higher than during normal 1 Hz pulsed operation. Assuming that the collector current functions the same way during oscillation as during saturation, we can speculate that the current in the circuit without an induced oscillation would be nearly 300 mA. This estimation is judged due to the 290 mA peak of collector current at the end of the pulse. The oscillation causes the TWT to reach a saturation condition and for the de-bunching electrons to intercept the beam tunnel, in the same way that the saturated RF pulse, shown in Figure 6-11, caused the collector current to be decreased. Since there is nearly 400 mA of total current in the system but the TWT was only designed for 310 mA of current, it is likely that there is enough current at the start of the TWT to induce an oscillation. However, during typical operation, the current in the TWT is reduced and oscillations do not occur.

Overall, the current in the system is higher than anticipated, as was shown during the beam test prior to TWT installation. The electron gun must be run at a high heater value in order to operate in the space-charge limited regime of the electron gun. The electron gun heater power can be reduced slightly (from 8.2 W to 8.0 W in experiment), which still allows operation in the space-charge limited regime while emitting 20 mA less total current. In this condition, the start-up oscillations are avoided when pulsed operation is begun. However, this reduces the current in the

system during stable operation, too, and the overall gain seen is lower.

If the operation conditions of the TWT were to be adjusted in some way to allow for less beam interception, the oscillations could be avoided in the device all together by allowing the electron gun to operate at a lower temperature while maintaining an ideal beam current for amplification. Regardless, these adjustments would only be to fine-tune the operation of the TWT and possibly match conditions closer to ideal with a higher interaction current in the TWT.

Chapter 7

Conclusions

7.1 Summary of Results

This thesis has covered the design and testing of an overmoded coupled-cavity TWT which has been implemented at MIT. The TWT involves an overmoded, or oversized, coupled-cavity structure which was designed to operate at 94 GHz. The experiment has shown successful operation of the TWT.

The overmoded TWT operates in the TM_{31} rectangular cavity mode. In doing so, the size of the cavity is larger than a comparable fundamental-mode cavity, allowing for many size related benefits. Most notably, the cavity size allows for a large beam tunnel; the 0.8 mm diameter beam tunnel is the largest of any W-band TWT. The large beam tunnel allows for a large current in the system with a small magnetic field, and, subsequently, more gain in the device. In addition, the oversized cavity allows for easier manufacturing of the structure and the ability for the TWT to be scaled to even higher frequencies.

The lower order modes in the TWT are suppressed using dielectric loading. The dielectric is selectively placed along the edges of the cavities to interact with the TM_{11} and TM_{21} modes, causing high losses; at the same location, the dielectric does not effect the TM_{31} mode. A lossy aluminum nitride composite dielectric was used in implementation which offered the desired high loss tangent characteristics while being compatible with vacuum conditions. The effect of the dielectric loading was

tested extensively in cold tests of the cavity structures.

In addition to analytical calculations, simulations of the TWT were performed in both 1-D Latte and 3-D CST particle studio. The TWT was designed to operate with a 2.5 kG solenoid magnet which was available for the experiment, which was the main engineering constraint on the experiment. Taking into account machining considerations of the TWT, the electron gun was determined to operate with a 31 kV, 310 mA beam. With these parameters, the coupling impedance of the TM_{31} mode in the final cavity was calculated in HFSS to be 3.2 Ω for 94 GHz, with a loss of about 0.3 dB/cm. Simulations from both Latte and CST agreed and predicted 32 dB of gain and 300 W peak output power.

The overmoded cavities were built and tested in several different cold tests in order to verify manufacturing methods and HFSS simulation results. The cavities were directly machined with a standard CNC mill, and the designs were built in 9- and 19-cavity cold tests out of both OFHC copper and glidcop. The tests showed good agreement with theory and frequency-matching to simulation. In addition, the aluminum nitride composite dielectric loading worked as simulated, demonstrating the suppression of unwanted modes and minimal additional losses to the TM_{31} mode. The glidcop structures performed with significantly less loses than the copper structures, agreeing much better to theoretical results and having less machining errors and anomalies. Due to these tests, it was determined to machine the final 87-cavity structures out of glidcop and with the same machining method and tolerances. Though the ohmic losses measured in the 87-cavity structures were large, they agreed with theory and were large enough to reduce round-trip oscillations in the TWT device. Therefore, no sever was needed in the TWT.

The entire TWT experiment was built and tested at MIT. The electron gun was designed in Michelle for the parameters necessary. A beam test prior to implementation showed 85 % beam transmission to the collector through an oversized beam tunnel, with 306$\pm$6 mA of current on the collector. Though the electron gun provided more total current than anticipated, the Child-Langmuir limit of the in-house built electron gun agreed well with theory.

The experiment was designed to have an interchangeable TWT structure and the TWT was tested in three stages: Structure A with full dielectric, Structure A with half dielectric, and Structure B with full dielectric. The experiment was operated with 2.8 microsecond high voltage pulses.

Initial testing of Structure A with the full dielectric loading in place showed 8 dB of gain with 10 W peak power at 95.5 GHz. Structure A was also tested with half dielectric loading, where oscillations were observed.

In the second stage of testing the TWT, the magnetic field was adjusted and Structure B was precision cleaned during finishing. The precision cleaning led to a higher transmission through the 87-cavity TWT. The TWT with Structure B achieved 21±2 dB device gain and 27 W output power. Adjusting for device losses, the TWT achieved 27±2 dB circuit gain with 55 W peak circuit output power. In testing, only 250 mA beam current was achieved, limiting the theoretical gain to 28.3 dB and peak power to 114 W, in good agreement with measurements.

7.2 Discussion of Relevance

Currently, there are many experiments focusing on W-band TWTs. It is an area of research with many immediate applications. In addition, the research allows for TWTs to be expanded for use in higher frequencies. The TWT built in this thesis is comparable to existing W-band TWTs. Commercially, W-band TWTs with 50 W output power are available from CPI. A W-band TWT with up to 30 dB of gain has been built [68], but many W-band TWTs have only 20 dB of gain. However, these designs are limited in their ability to be scaled to higher frequencies. The overmoded TWT has a limited bandwidth, but that was not a goal of this design. In addition, the overmoded TWT was operated at a significantly lower magnetic field than other state-of-the-art W-band TWTs, allowing for less current in the overmoded system.

This experiment sought to build a TWT with a new design that had not previously been implemented. Though there are several designs for overmoded TWTs, none had previously been realized in experiment. This thesis has documented the first successful

operation of an overmoded TWT.

In building this overmoded design, as with any first-time device, the success of the experiment was not guaranteed. The experiment demonstrated an overmoded TWT of comparable gain and power to present-day W-band TWTs. In addition, the operation of this design has shown that an overmoded design is capable of handling high gain and nominal output powers at high frequency. The selective dielectric loading successfully suppressed oscillations from unwanted modes, and the lossy design prevented round-trip oscillations from the operating mode. The overmoded TWT does not have the same frequency limitations as the traditional fundamental mode TWT, and the design has the ability to be extended to higher frequencies. The fabrication of the overmoded TWT in the W-band was performed using direct machining, another advantage of this design over fundamental-mode TWTs. The implementation and research for this overmoded TWT can be used to design and build other overmoded TWTs at higher frequencies.

7.3 Future Work

There is much area for improvement with the design of this TWT. The experiment itself has room for improvement, particularly by fine-tuning the magnetic field focusing and eliminating the voltage pulse flat-top variation. In addition, the experiment design would be greatly enhanced with the addition of better coupling with WR-10 waveguide windows.

However, the most interesting TWT engineering advances will happen by expanding research to higher frequencies and investigating other types of overmoded devices. TWTs with large beam tunnels and oversized cavities are capable of producing high powers without the need for high magnetic fields or complex nano-fabrication techniques. This research has laid the groundwork for studying unconventional designs and oversized TWT structures.

Bibliography

[1] U. S. Army. *Army Science and Technology Master Plan*. 21 March 1997.

[2] G. Arnau-Izquierdo, S. Calatroni, S. Heikkinen, T. Ramsvik, S. Sgobba, M. Taborelli, and W. Wuensch. Material selection and characterization for high gradient RF applications. In *IEEE Particle Accelerator Conf. (PAC)*, pages 2197–2199, June 2007.

[3] Anisullah Baig, Diana Gamzina, Robert Barchfeld, Calvin Domier, Larry R Barnett, and Neville C Luhmann Jr. 0.22 THz wideband sheet electron beam traveling wave tube amplifier: cold test measurements and beam wave interaction analysis. *Physics of Plasmas*, 19(9):93–110, 2012.

[4] James H. Billen and Lloyd M. Young. Poisson/superfish on pc compatibles. In *Proceedings of the Particle Accelerator Conference (PAC)*, pages 790–792. IEEE, 1993.

[5] J. H. Booske. Plasma physics and related challenges of millimeter-wave-to-terahertz and high power microwave generation. *Physics of Plasmas*, 15(5):1–16, May 2008.

[6] Bruce Carlsten and Steve Russell. Microwave sources course notes. United States Particle Accelerator School (USPAS), June 2012.

[7] E. M. Choi, C. Marchewka, I. Mastovsky, M. A. Shapiro, J. R. Sirigiri, and R. J. Temkin. Megawatt power level 120 GHz gyrotrons for ITER start-up. In *Journal of Physics: Conference Series*, volume 25, page 1. IOP Publishing, 2005.

[8] T. S. Chu, F. V. Hartemann, B. G. Danly, and R. J. Temkin. Single-mode operation of a Bragg free-electron maser oscillator. *Phys. Rev. Lett.*, 72:2391–2394, Apr 1994.

[9] E. N. Comfoltey, M. A. Shapiro, J. R. Sirigiri, and R. J. Temkin. Design of an overmoded W-band TWT. In *10th IEEE Intl. Vacuum Electronics Conf.*, pages 127–128, Apr 2009.

[10] Edward N. Comfoltey. Design of an overmoded W-Band coupled cavity TWT. Master's thesis, Massachusetts Institute of Technology, Department of Electrical Engineering and Computer Science, Cambridge, MA, 2009.

[11] MIT Lincoln Laboratory Communications and Community Outreach Office. *Annual Report*. MIT Lincoln Laboratory, 2011.

[12] David H. Staelin and Ann W. Morgenthaler and Jin Au Kong. *Electromagnetic Waves*. Prentice-Hall, Inc., 1994.

[13] Antonio C. Torrezan de Sousa. *Frequency-tunable second-harmonic submillimeter-wave gyrotron oscillators*. PhD thesis, Massachusetts Institute of Technology, Department of Electrical Engineering and Computer Science, Cambridge, MA, September 2010.

[14] David E. Dean, Thomas D. Schaefer, Gregory A. Steinlage, and Liqin Wang. Bearing temperature and focal spot position controlled anode for a CT system, March 13 2007. US Patent 7,190,765.

[15] Duniway Stockroom Corp. *Data Sheet: Calculation of Conductance*, 2014.

[16] I. Ederra, I. Khromova, R. Gonzalo, N. Delhote, D. Baillargeat, A. Murk, B. E. J. Alderman, and P. M. de Maagt. Electromagnetic-bandgap waveguide for the millimeter range. *IEEE Trans. on Microwave Theory and Techniques*, 58(7):1734–1741, July 2010.

[17] J. Feicht, K. N. Loi, W. L. Menninger, J. G. Nicolello, and X. Zhai. Space qualified 140 watt linearized L-band helix TWTA. In *IEEE Intl. Vacuum Electronics Conf. (IVEC)*, pages 355–356. IEEE, 2012.

[18] M. Field, Z. Griffith, A Young, C. Hillman, B. Brar, D. Gamzina, R. Barchfield, Jinfeng Zhao, A Spear, A Baig, C. Domier, L. Barnett, N. Luhmann, T. Kimura, J. Atkinson, T. Grant, Y. Goren, T. Reed, and M. Rodwell. Development of a 220 GHz 50 W sheet beam traveling wave tube amplifier. In *IEEE Intl. Vacuum Electronics Conf. (IVEC)*, pages 225–226, April 2014.

[19] D. Gamzina, Robert Barchfeld, L.R. Barnett, N.C. Luhmann, and Young-Min Shin. Nano CNC milling technology for terahertz vacuum electronic devices. In *IEEE Intl. Vacuum Electronics Conf. (IVEC)*, pages 345–346, Feb 2011.

[20] J. W. Gewartowski and H. A. Watson. *Principles of Electron Tubes*. D Van Nostrand Company, Inc., 1965.

[21] J. F. Gittens. *Power Travelling Wave Tubes*. American Elsevier, 1965.

[22] Yubin Gong, Hairong Yin, Lingna Yue, Zhigang Lu, Yanyu Wei, Jinjun Feng, Zhaoyun Duan, and Xiong Xu. A 140-GHz Two-Beam Overmoded Folded-Waveguide Traveling-Wave Tube. *IEEE Trans. on Plasma Science*, 39(3):847–851, Mar 2011.

[23] V. L. Granatstein, R. K. Parker, and C. M. Armstrong. Vacuum electronics at the dawn of the twenty-first century. *Proceedings of the IEEE*, 87(5):702–7161, May 1999.

[24] Chen-Yu Gung, N. N. Martovetsky, D. R. Hatfield, J. R. Miller, J.-H. Kim, and J. H. Schultz. Fabrication of the first US ITER TF conductor sample for qualification in SULTAN facility. *IEEE Transactions on Applied Superconductivity*, 19(3):1474–1477, June 2009.

[25] A. E. Harrison. *Klystron Tubes*. McGraw-Hill Book Company, 1947.

[26] Hermann A. Haus. *Waves and Fields in Optoelectronics*. CBLS, 2004.

[27] J. He, Y. Wei, Y. Gong, and W. Wang. Linear analysis of a W band groove-loaded folded waveguide traveling wave tube. *Physics of Plasmas*, 17(11), November 2010.

[28] Jun He, Yanyu Wei, Yubin Gong, Wenxiang Wang, and Gun-Sik Park. Investigation on a W band ridge-loaded folded waveguide TWT. *IEEE Transactions on Plasma Science*, 39(8):1660–1664, Aug 2011.

[29] Heatwave Labs, Inc. *Dispenser Cathodes*, July 2002.

[30] J-P Hogge, TP Goodman, Stefano Alberti, Ferrando Albajar, KA Avramides, P Benin, S Bethuys, W Bin, T Bonicelli, A Bruschi, et al. First experimental results from the european union 2-MW coaxial cavity ITER gyrotron prototype. *Fusion Science and Technology*, 55(2):204–212, 2009.

[31] Peter Horoyski, Dave Berry, and Brian Steer. A 2 GHz bandwidth, high power W-band extended interaction klystron. In *IEEE Intl. Vacuum Electronics Conf. (IVEC)*. IEEE, 2007.

[32] Yinfu Hu, Jinjun Feng, Jun Cai, Xianping Wu, Shaoyun Ma, Bo Qu, Juxian Zhang, and Tongjiang Chen. A broadband microwave window for W-band TWT. In *IEEE Intl. Vacuum Electronics Conf. (IVEC)*, pages 376–377, April 2008.

[33] B. G. James. Coupled-Cavity TWT designed for future Mm-wave systems. In *Microwave systems news and communications technology*, volume 16, 1986.

[34] B. G. James and P. Kolda. A ladder circuit coupled-cavity TWT at 80-100 GHz. In *1986 Intl. Electron Devices Meeting*, volume 32, pages 494–497, 1986.

[35] C. D. Joye, A. M. Cook, J. P. Calame, D. K. Abe, K. T. Nguyen, E. L. Wright, A. N. Vlasov, I. A. Chernyavskiy, T. Kimura, and B. Levush. Demonstration of a high power, wideband 220 GHz serpentine waveguide amplifier fabricated by UV-LIGA. In *IEEE Intl. Vacuum Electronics Conf. (IVEC)*, pages 1–2, May 2013.

[36] Colin D. Joye, Alan M. Cook, Jeffrey P. Calame, David K. Abe, Alexander N. Vlasov, Igor A. Chernyavskiy, Khanh T. Nguyen, and Edward L. Wright. Microfabrication and cold testing of copper circuits for a 50-watt 220-GHz traveling wave tube. In *Proc. SPIE*, volume 8624, 2013.

[37] A. S. Gilmour Jr. *Principles of Traveling Wave Tubes*. Artech House, 1994.

[38] A. Kasugai, R. Minami, K. Takahashi, N. Kobayashi, and K. Sakamoto. Long pulse operation of 170 GHz ITER gyrotron by beam current control. *Fusion engineering and design*, 81(23):2791–2796, 2006.

[39] Rudolf Kompfner. *The Invention of the Traveling-Wave Tube*. San Francisco Press, 1964.

[40] Jin Au Kong. *Electromagnetic Wave Theory*. EMW Publishing, 2008.

[41] C. Kory, L. Ives, M. Read, J. Booske, H. Jiang, D. van der Weide, and P. Phillips. Microfabricated W-band traveling wave tubes. In *13th Intl. Conf. on IR mm Waves and THz Tech.*, volume 1, pages 85–86, Sept 2005.

[42] C. L. Kory, M. E. Read, R. L. Ives, J. H. Booske, and P. Borchard. Design of Overmoded Interaction Circuit for 1-kW 95-GHz TWT. *IEEE Trans. on Electron Devices*, 56(5):713–720, May 2009.

[43] R. Kowalczyk, A. Zubyk, C. Meadows, M. Martin, M. Kirshner, R. True, A. Theiss, J. Rominger, and C. Armstrong. A 100 watt W-band MPM TWT. In *IEEE Intl. Vacuum Electronics Conf.*, May 2013.

[44] B. Levush, D. Abe, J. Pasour, S. Cooke, F. Wood, P. Larsen, K. Nguyen, E. Wright, D. Pershing, and A Balkcum. Sheet electron beam millimeter-wave amplifiers at the naval research laboratory. In *IEEE Intl. Conf. on Microwaves, Communications, Antennas and Electronics Systems (COMCAS)*, Oct 2013.

[45] S. M. Lewis, E. A Nanni, and R. J. Temkin. Direct machining of low-loss THz waveguide components with an RF choke. *IEEE Microwave and Wireless Components Letters*, PP(99), 2014.

[46] Alexander G. Litvak, Gregory G. Denisov, Vadim E. Myasnikov, Evgeny M. Tai, Englen A. Azizov, and Vladimir I. Ilin. Development in russia of megawatt power gyrotrons for fusion. *Journal of Infrared, Millimeter, and Terahertz Waves*, 32(3):337–342, 2011.

[47] K. P. McCarthy, F. J. Stocklin, B. J. Geldzahler, D. E. Friedman, and P. B. Celeste. NASAs Evolution to Ka-Band Space Communications for Near-Earth Spacecraft. *Proceedings of the SpaceOps 2010 Conf.*, April 2010.

[48] Millitech, Smiths Microwave. *Active Multiplier Chain Data Sheet*, 2014. http://www.millitech.com/.

[49] Matthew Morgan, Sander Weinreb, Niklas Wadefalk, and Lorene Samoska. A MMIC-based 75-110 GHz signal source. In *IEEE MTT-S Intl. Microwave Symposium Digest*, volume 3, pages 1859–1862. IEEE, 2002.

[50] Emilio A. Nanni. *A 250 GHz photonic band gap gyrotron amplifier* . PhD thesis, Massachusetts Institute of Technology, Department of Electrical Engineering and Computer Science, Cambridge, MA, June 2013.

[51] K. Nguyen, L. Ludeking, A. Cook, S. Cooke, C. Joye, J. Calame, A. Burke, E. Wright, D. Pershing, J. Pasour, J. Petillo, A. Vlasov, D. Chernin, D. K. Abe, and B. Levush. Design of a wideband high-power W-band serpentine TWT. In *IEEE Intl. Vacuum Electronics Conf. (IVEC)*, May 2013.

[52] Khanh Nguyen, J. Pasour, E. Wright, D. Abe, L. Ludeking, D. Pershing, and B. Levush. Linearity performance of multi-stage TWT amplifiers: Cascade vs. series. In *IEEE Intl. Vacuum Electronics Conf. (IVEC)*, pages 309–310, Feb 2011.

[53] J. Pasour, E. Wright, K. T. Nguyen, A. Balkcum, F. N. Wood, R. E. Myers, and B. Levush. Demonstration of a multikilowatt, solenoidally focused sheet beam amplifier at 94 GHz. *IEEE Transactions on Electron Devices*, 61(6):1630–1636, June 2014.

[54] J. Petillo, P. Blanchard, A. Mondelli, K. Eppley, W. Krueger, T. McClure, D. Panagos, B. Levush, J. Burdette, M. Cattelino, et al. The MICHELLE electron gun and collector modeling tool. In *Proc. of the 2001 Particle Accelerator Conference (PAC)*, volume 4, pages 3054–3056. IEEE, 2001.

[55] Norman H. Pond. *The Tube Guys*. Russ Cochran, 2008.

[56] David M. Pozar. *Microwave Engineering*. John Wiley, second edition, 1998.

[57] Herbert J. Reich, Philip F. Ordnung, Herbert L. Krauss, and John G. Skalnik. *Microwave Theory and Techniques*. D. Van Nostrand Company, Inc., 1953.

[58] Albert Roitman, Peter Horoyski, Mark Hyttinen, Dave Berry, and Brian Steer. Extended interaction klystrons for submillimeter applications. In *IEEE Intl. Vacuum Electronics Conf. (IVEC)*, pages 191–191. IEEE, 2006.

[59] M. J. Rosker and H. B. Wallace. Imaging Through the Atmosphere at Terahertz Frequencies. *IEEE/MTT-S International Microwave Symposium, 2007*, pages 773–776, June 2007.

[60] E. Savrun, V. Nguyen, and D. K. Abe. High thermal conductivity aluminum nitride ceramics for high power microwave tubes. In *IEEE Intl. Vacuum Electronics Conf. (IVEC)*, pages 34–35, 2002.

[61] James Schellenberg, E. Watkins, M. Micovic, Bumjin Kim, and Kyu Han. W-band, 5 W solid-state power amplifier/combiner. In *IEEE MTT-S Intl. Microwave Symposium Digest*, pages 240–243, May 2010.

[62] S. Sengele, Hongrui Jiang, J. H. Booske, C. L. Kory, D. W. van der Weide, and R. L. Ives. Microfabrication and Characterization of a Selectively Metallized W-Band Meander-Line TWT Circuit. *IEEE Trans. on Electron Devices*, 56(5):730–737, May 2009.

[63] P. H. Siegel. Terahertz Technology. *IEEE Trans. on Microwave Theory and Techniques*, 50(3):910–928, March 2002.

[64] E. Simakov, D. Dalmas, L. Earley, W. Haynes, R. Renneke, and D. Shchegolkov. Progress on the Omniguide Traveling-Wave Tube Experiment. *52nd Meeting of APS Division of Plasma Physics*, November 2010.

[65] Spotwelding Consultants, Inc. *Technical Data Sheet: Glidcop AL-25*, 2014.

[66] Spotwelding Consultants, Inc. *Technical Data Sheet: Glidcop AL-60*, 2014.

[67] David S. Tax. *Experimental study of a high efficiency step-tunable MW gyrotron oscillator*. PhD thesis, Massachusetts Institute of Technology, Department of Electrical Engineering and Computer Science, Cambridge, MA, September 2013.

[68] A. J. Theiss, C. J. Meadows, R. Freeman, R. B. True, J. M. Martin, and K. L. Montgomery. High-Average-Power W-band TWT Development. *IEEE Trans. on Plasma Science*, 38(6):1239 –1243, June 2010.

[69] M. Thumm. Progress on gyrotrons for ITER and future thermonuclear fusion reactors. *IEEE Trans. on Plasma Science*, 39(4):971–979, April 2011.

[70] Shulim E. Tsimring. *Electron Beams and Microwave Vacuum Electronics*. Wiley Interscience, 2007.

[71] Robert Valdiviez, D. Schrage, F. Martinez, W. Clark, et al. The use of dispersion-strengthened copper in accelerator designs. *XX International Linac Coference*, 2000.

[72] Shuzhong Wang, Cunjun Ruan, Xiudong Yang, Ding Zhao, and Changqing Zhang. The design considerations of W-band broad band output window. In *IEEE 14th Intl. Vacuum Electronics Conf. (IVEC)*. IEEE, 2013.

[73] R. D. Watson, F. M. Hosking, M. F. Smith, and C. D. Croessmann. Development and testing of the ITER divertor monoblock braze design. *Fusion Technology*, 19:1794–1798, 1991.

[74] J.G. Wohlbier, J.H. Booske, and I. Dobson. On the physics of harmonic injection in a traveling wave tube. *IEEE Trans. on Plasma Science*, 32(3):1073 – 1085, June 2004.